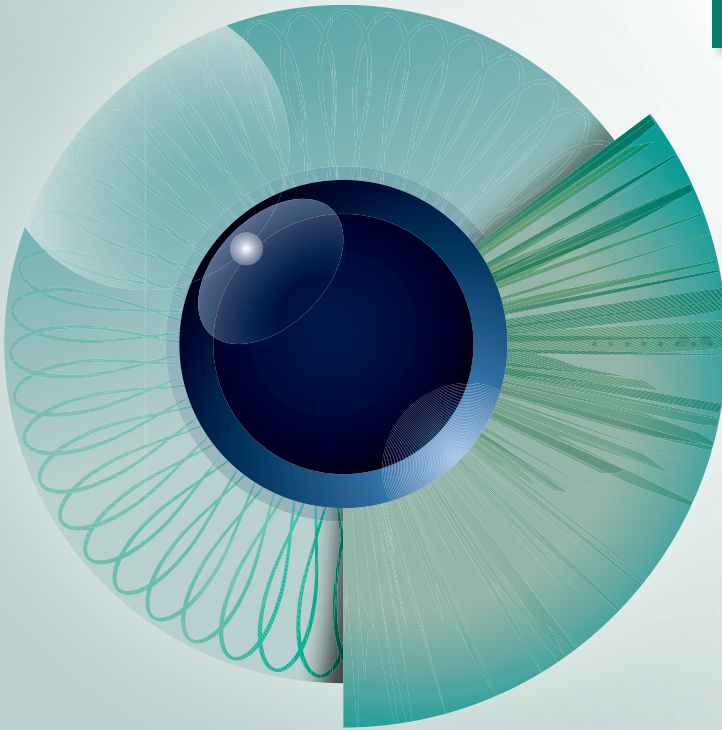
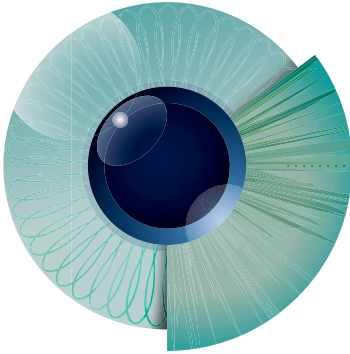


Issue 2-3



Journal for Modeling in Ophthalmology





JMO

Journal for
Modeling in
Ophthalmology

Journal for Modeling in Ophthalmology (JMO) was created in 2014 with the aim of providing a forum for interdisciplinary approaches integrating mathematical and computational modeling techniques to address open problems in ophthalmology.

The Editorial Board members include experts in ophthalmology, physiology, mathematics, and engineering, and strive to ensure the highest scientific level of the contributions selected for publication. JMO aims to be the voice for this rapidly growing interdisciplinary research and we hope you will join us on this exciting journey.

JMO welcomes articles that use modeling techniques to investigate questions related to the anatomy, physiology, and function of the eye in health and disease.

For further information on JMO's focus and scope as well as manuscript submissions:

www.modeling-ophthalmology.com
info@modeling-ophthalmology.com

Copyright

Authors who publish in JMO agree to the following terms:
a. Authors retain copyright and grant the journal JMO right of first publication, with the work twelve (12) months after publication simultaneously licensed under a Creative Commons Attribution License that allows others to share the work with an acknowledgement of the work's authorship and initial publication in JMO.

Chief editors

Alon Harris
Giovanna Guidoboni

Managing editor

Giovanna Guidoboni

Editorial board

Makoto Araie
Fabio Benfenati
Richard J. Braun
Thomas Ciulla
Vital Paulino Costa
Ahmed Elsheikh
Jean-Frederic Gerbeau
Rafael Grytz
Michaël Girard
Gabor Hollo
Ingrida Januleviciene
Jost Jonas
Larry Kagemann
Fabian Lerner
Anat Loewenstein
Toru Nakazawa
Colm O'Brien
Anna Pandolfi
Peter Pinsky
Rodolfo Repetto
Riccardo Sacco
Einar Stefansson
Fotis Topouzis
Emanuele Trucco
Zoran Vatauvuk
Joanna Wierzbowska

Publisher

Kugler Publications
P.O. Box 20538
1001 NM Amsterdam
The Netherlands
info@kuglerpublications.com
www.kuglerpublications.com

ISSN

Online: 2468-3930

Print: 2468-3922

Manuscript submissions

Author guidelines and templates are available via the website, through which all manuscripts should be submitted. For inquiries please contact us via e-mail.

Publication frequency

JMO is published four issues per year (quarterly) electronically. A selection is published in print twice a year and distributed free of charge at congresses through Kugler Publications or partners.

Advertising inquiries

JMO offers online and in print sponsorship and advertising opportunities. Please contact Kugler Publications to for inquiries.

b. After 12 months from the date of publication, authors are able to enter into separate, additional contractual arrangements for the non-exclusive distribution of JMO's published version of the work, with an acknowledgement of its initial publication in JMO.

Open access policy

The first volume of JMO is fully open access (after registration) without requiring any publication fee from the authors. However, we are currently evaluating various models to cover the publications costs while keeping knowledge as accessible as possible, which remains our first priority. Possible models include subscription fees, publication fees, and advertisement venues, or a combination. Please share your thoughts with us on this hot topic via e-mail.

Disclaimers

All articles published, including editorials and letters, represent the opinions of the authors and do not reflect the official policy of JMO, its sponsors, the publisher or the institution with which the author is affiliated, unless this is clearly specified. Although every effort has been made to ensure the technical accuracy of the contents of JMO, no responsibility for errors or omissions is accepted. JMO and the publisher do not endorse or guarantee, directly or indirectly, the quality or efficacy of any product or service described the advertisements or other material that is commercial in nature in any issue. All advertising is expected to conform to ethical and medical standards. No responsibility is assumed by JMO or the publisher for any injury and/or damage to persons or property as a matter of products liability, negligence or otherwise, or from any use or operation of any methods, products, instructions, or ideas contained in the material herein. Because of rapid advances in the medical sciences, independent verification of diagnoses and drug dosages should be made.



Table of contents

Editorial 5
Kara L. Maki, Rodolfo Repetto, Richard J. Braun

Meeting highlights articles

Relationship between intraocular, blood, and cerebrospinal fluid pressures: a theoretical approach 9
Giovanna Guidoboni, Fabrizia Salerni, Rodolfo Repetto, Marcela Szopos, Alon Harris

A simulation study on the effect of ionic currents on transmission from cones to retinal OFF type cone bipolar cells 14
Akito Ishihara

A Model for Tear Film Dynamics During a Realistic Blink 21
Kara L. Maki, William D. Henshaw, Alex McManus, Richard J. Braun, Dylan M. Chapp, Tobin A. Driscoll

Automated classification of dry eye type analyzing interference fringe color images of tear film using machine learning techniques 28
Katsumi Yabusaki, Reiko Arita, Takanori Yamauchi

Influence of benzalkonium chloride on tear film lipid layer stability: a molecular level view by employing *in silico* modeling 36
Kamila Riedlova, Adela Melcrova, Agnieszka Olzynska, Philippe Daull, Jean-Sebastien Garrigue, Lukasz Cwiklik

Original articles

Image processing-based model for tortuosity measurement of retinal blood vessels 43
Sanyukta Chetia, S.R. Nirmala

A socioeconomic evaluation of early-stage and moderate glaucoma patients 68
Miglė Lindžiūtė, Ingrida Janulevičienė

**Predicting infusion pressure during pars plana vitrectomy:
a physically based model 88**

Tommaso Rossi, Giorgio Querzoli, Giampiero Angelini, Alessandro Rossi, Carlo Malvasi, Laura Landi, Serena Telani, Guido Ripandelli

**Peripapillary non-flow area measurement for progressive localized
glaucomatous perfusion damage: a case series104**

Gábor Holló

**Increasing protected data accessibility for age-related cataract research using a
semi-automated honest broker.115**

Samaikya Valluripally, Murugesan Raju, Prasad Calyam, Mauro Lemus, Soumya Purohit, Abu Mosa, Trupti Joshi



Mathematical modeling highlights from ARVO 2018

Kara L. Maki¹, Rodolfo Repetto², Richard J. Braun³

¹*School of Mathematical Sciences, Rochester Institute of Technology, Rochester, NY, USA;* ²*Department of Civil, Chemical and Environmental Engineering, University of Genoa, Genoa, Italy;* ³*Department of Mathematical Sciences, University of Delaware, Newark, DE, USA*

Keywords: anterior chamber, dry eye, modeling, posterior chamber, retina, tear film

At the ARVO annual meeting, there is an increasing number of contributions that involve significant mathematical modeling of ocular physiology and procedures. There has long been significant use of statistical methods for understanding data from a variety of *in vivo* measurements and clinical trials. Beyond these important uses of statistical and mathematical tools, a growing number of researchers are developing mathematical and computational models, often based on fundamental principles from physics, chemistry and mechanics, that provide insights into ocular phenomena. A number of areas had noticeable contributions involving applications of models, such as tear production, tear film dynamics, corneal biomechanics, retinal blood flow, and glaucoma. We list a number of such contributions in this introduction and follow those with five extended abstracts that summarize some of the studies mentioned here.

Guidoboni *et al.*¹ studied fluid flow in the eye and related organs by using a lumped parameter model. Their model accounts for the flows of blood and aqueous humor in the eyes and the flows of blood, cerebrospinal fluid, and interstitial fluid in the brain, as well as their interactions. Eye and brain are connected to a simple model of the whole-body circulation. The model captures the major observed trends in the interactions between cerebrospinal fluid pressure, intraocular pressure (IOP), and choroidal venule pressure.

Ishihara² used a mathematical model to simulate transmission from cones to OFF type cone bipolar cells (OFF-BCs) and the role of ionic currents in this process. In the

Correspondence: Richard J. Braun, Department of Mathematical Sciences, University of Delaware, Newark, DE 19716, USA. E-mail: rjbraun@udel.edu

cone cells, the model focused on the role of glutamate and its receptors, as well as calcium ions, after the cells are stimulated by a photosensitive current model. In the OFF-BCs, the model focused on rectifying currents that may involve potassium ions. The two cells were coupled together in the model, and parameters were determined from mammalian retinas where possible. Frequency characteristics of the system were found, suggesting a band-pass behavior. At lower light levels, the OFF-BC response was suppressed; however, transient signals could still be sent at low light levels.

Maki *et al.*³ studied the influence of the blink on the formation of a stable tear film. They developed a numerical method to approximate a simplified mathematical model characterizing the tear film dynamics during a realistic blink. The model captures the flow of the aqueous tears on the exposed ocular surface, and accounts for influxes and effluxes of aqueous tears at the lid margin during the blink. It was found that sufficient aqueous tears must be supplied along the lid margin near the exposed ocular surface and must be supplied at rates comparable to the speed of ocular exposure to ensure the formation of a stable tear film with “healthy” menisci. These simulations will allow for the continued exploration of the tear dynamics in regions on the ocular surface not accessible to imaging techniques due to interference by lid motion.

Yabusaki *et al.*⁴ are the first group, to our knowledge, to publish on machine learning (ML) techniques applied to tear film imaging and dry eye diagnosis. Using interference fringe patterns and colors from the tear film lipid layer (TFLL) as input, they aimed to diagnose differences between aqueous deficient dry eye (ADDE), evaporative dry eye (EDE), and normals. A linear support vector machine-based ML approach was compared to diagnoses by one of the co-authors (who is experienced at diagnosis). Better agreement was obtained for ADDE than for EDE or normal-type predictions. This approach opens the door to an exciting path of investigation for ocular surface researchers and clinicians.

Cwiklik *et al.*⁵ simulated the dynamics of the TFLL in the presence of the preservative benzalkonium chloride (BAK) with a few different hydrocarbon chain lengths. These short-chain molecules are surface active and similar to cetalkonium chloride (CKC). The latter was previously shown to affect the TFLL, improving its stability. Their detailed simulations showed that the BAK molecules, particularly the shortest one, could orient itself through a wide range of angles relative to the TFLL/aqueous interface. Longer molecules like CKC could not do this. These results help explain the destabilizing effect of short-chain BAK molecules.

Zhong *et al.*⁶ study the tear breakup (TBU) caused by local “globs” of excess lipid. The surface active globs cause rapid divergent (outward) flow that can lead to rapid TBU. They also included evaporation of the aqueous to surrounding air, osmotic supply of aqueous from the epithelium, and transport of solutes such as fluorescein (FL). From computed tear film thickness and FL concentration, they could compute

the emitted FL intensity. They then computed what fluorescent images would look like in experiments and determined desirable initial concentration ranges for imaging evaporative (slow) vs rapid (divergent flow) instances of TBU.

There were also math-focused presentations in the areas of corneal biomechanics, glaucoma, and more. For example, Tavakol *et al.*⁷ simulated the response of the cornea to mechanical stimuli. The long-term goal is to estimate corneal elasticity by measuring the speed of acoustic wave propagation. The authors presented a finite element (FE) model created in COMSOL, where they probed how individual parameters affected corneal wave propagation.

Missel and Sarangapani⁸ presented a computational multi-physics model to study the potential benefit of implanting more than one supraciliary micro-stent in cataract surgery. The micro-stent is implanted to lower IOP in glaucoma patients. Their modeling efforts found a single micro-stent is sufficient in equilibrating the IOP with the suprachoroidal pressure.

Jin *et al.*⁹ used FE analysis to model the origin of the ocular pulse and to investigate the role of biomechanical factors on optic nerve head (ONH) deformations during the cardiac cycle. The authors constructed a FE model of the eye and modelled the choroid as a biphasic material, constituted of a solid phase (connective tissues) and a fluid phase (blood). The model shows that fluctuations of the arterial blood pressure produce significant IOP changes and ONH deformations. Systolic ophthalmic artery pressure and choroidal stiffness are found to be the parameters with the strongest influence.

Chuangsuwanich *et al.*¹⁰ proposed a computational model to study oxygen concentration and consumption in the retinal ganglion cell axons in the lamina cribrosa (LC). They generated many artificial LC micro-capillary networks, in which they simulated numerically blood flow and oxygen diffusion and consumption. The model highlights the heterogeneous distribution of oxygen concentration within the LC, which may contribute to spatial variability of axonal loss in glaucoma.

We hope that you enjoy the extended abstracts here as much as we enjoyed learning about these and other results from ARVO 2018.

Acknowledgements

Richard J. Braun was supported by National Science Foundation (NSF) grant DMS 1412085. Kara Lee Maki was supported by NSF grant DMS 1412141.

References

1. Guidoboni G, Salerni F, Repetto R, Szopos M, Harris A. Relationship between intraocular pressure, blood pressure and cerebrospinal fluid pressure: a theoretical approach. *Invest Ophthalmol Vis Sci.* 2018;59(9):1665.
2. Ishihara A. A simulation study of information transmission in OFF cone bipolar cell pathway. *Invest Ophthalmol Vis Sci.* 2018;59(9):1873.
3. Maki K, McManus A, Henshaw W, Braun R. The influence of tear supply and drainage on tear film dynamics during a realistic blink. *Invest Ophthalmol Vis Sci.* 2018;59(9):3817.
4. Yabusaki K, Arita R, Yamauchi T. Automated classification of dry eye type analyzing interfering fringe color images of tear film using machine learning technologies. *Invest Ophthalmol Vis Sci.* 2018;59(9):4860.
5. Cwiklik L, Riedlova K, Melcrova A, Olzynska A, Daull P, Garrigue J. Influence of benzylalkonium chloride on tear film lipid layer stability: a molecular level view by employing in silico modeling. *Invest Ophthalmol Vis Sci.* 2018;59(9):3279.
6. Zhong L, Antwi D, Braun R, King-Smith P, Begley C. Simulation and measurement of glob-driven tear film breakup. *Invest Ophthalmol Vis Sci.* 2018;59(9):4907.
7. Tavakol B, Birkenfeld J, Ramier A, Yun S-H. Development of a time-domain finite-element model of acoustic wave propagation in the cornea. *Invest Ophthalmol Vis Sci.* 2018;59(9):1401.
8. Missel P, Sarangapani R. Comparing the predicted efficacy of one versus two supraciliary micro-stents for lowering IOP in glaucoma patients using an ocular computational fluid dynamic model. *Invest Ophthalmol Vis Sci.* 2018;59(9):2057.
9. Jin Y, Wang X, Zhang L, Jonas J, Aung T, Schmetterer L, et al. Finite element modeling predicts neural tissue shear in the neuroretinal rim caused by pulsatile blood pressure. *Invest Ophthalmol Vis Sci.* 2018;59(9):2037.
10. Chuangsuwanich T, Leo L, Schmetterer L, Girard MJ. An hourglass pattern of oxygen distribution in the lamina cribrosa predicted using a computational model. *Invest Ophthalmol Vis Sci.* 2018;59(9):4477.



Relationship between intraocular, blood, and cerebrospinal fluid pressures: a theoretical approach

Giovanna Guidoboni¹, Fabrizia Salerni², Rodolfo Repetto³, Marcela Szopos⁴, Alon Harris⁵

¹Department of Electrical Engineering and Computer Science, University of Missouri, Columbia, MO, USA; ²Department of Mathematical, Physical and Computer Science, University of Parma, Parma, Italy; ³Department of Civil, Chemical and Environmental Engineering, University of Genoa, Genoa, Italy; ⁴Laboratoire MAP5, UMR CNRS 8145, Université Paris Descartes, Sorbonne Paris Cité, Paris, France; ⁵Institute and Department of Ophthalmology, Indiana University School of Medicine, Indianapolis, IN, USA

Keywords: blood pressure, cerebrospinal fluid pressure (CSF), intraocular pressure (IOP)

1. Background and purpose

Intraocular pressure (IOP), arterial blood pressure (P_A), and cerebrospinal fluid (CSF) pressure have been identified as major players in several ocular pathologies, including glaucoma, central vein occlusion, and papilledema, to name a few. IOP, P_A , and CSF pressures are not independent from each other. For example, aqueous humor and CSF flows, whose mechanics contribute to establish IOP and CSF pressure levels, originate from blood flow, which is driven by P_A . As a consequence, it is difficult to experimentally isolate IOP, P_A , and CSF pressure and to disentangle their effect in pathological conditions. Here we utilize a theoretical approach to address this issue.

Correspondence: Fabrizia Salerni, Department of Mathematical, Physical and Computer Science, University of Parma, Parma, Italy. E-mail: fabrizia.salerni@studenti.unipr.it

2. Methods

The present mathematical model is developed to simulate fluid flow in the eyes (retina, choroid, ciliary body, and lamina cribrosa) and brain connected with a simplified description of the whole-body circulation consisting in central arteries and veins. We use an electrical circuit analog that accounts for:

1. the flows of blood and aqueous humor in the eyes;
2. the flows of blood, CSF, and interstitial fluid in the brain; and
3. lamina cribrosa biomechanics influenced by tissue pressure in the optic nerve head due to CSF within the subarachnoid space (SAS), represented by an extra ventricular compartment.

The lumped parameter circuit for the brain is adapted from the work described and validated in Lakin and Stevens¹; the eye model originates from the approach proposed in Guidoboni *et al.*² for the study of retinal circulation and has been extended to account for the three ocular vascular beds (retina, choroid, and ciliary body) on the basis of the work of Kiel *et al.*³ Finally, ocular hemodynamics is coupled with the aqueous humor dynamics as in Szopos *et al.*⁴ The model takes into account the complex interaction between different biofluids in the brain and in the eye. The flow is driven by P_A , which is given as a variable input, while the venous pressure P_V is kept constant. Intracranial pressure (ICP) is the pressure in the brain compartment and CSF production rate is imposed and kept constant. IOP results from the balance between aqueous humor production and drainage, and acts as an external pressure on ocular vascular veins that are modeled as Starling resistors (they collapse when the transmural pressure is negative). The lamina cribrosa exerts a compressive stress from the combined action between IOP, CSF pressure, and scleral tension on translaminar central retinal arteries and veins segments as in Guidoboni *et al.*² Model parameters have been calibrated on published data. The assumptions related to the coupling between the various elements is validated: the model is used to simulate changes in IOP, CSF pressure, flow, and pressure distributions across the whole system induced by changes in P_A . Results are compared to those reported in clinical studies. In this current version of the model, time dependence and blood flow regulation are not included.

3. Results

Our model predicts relationships between IOP, P_A , and CSF pressure that are within the same range as those reported in clinical studies. Figure 1 captures the overall trend of CSF pressure variations due to changes in blood pressure and IOP, as reported in Ren *et al.*⁵ Moreover, as show in Table 1, the model captures the trend of IOP variation due to changes in blood pressure, as reported by various authors.⁵⁻⁹ In addition, choroidal venous pressure in the vortex veins computed by the model

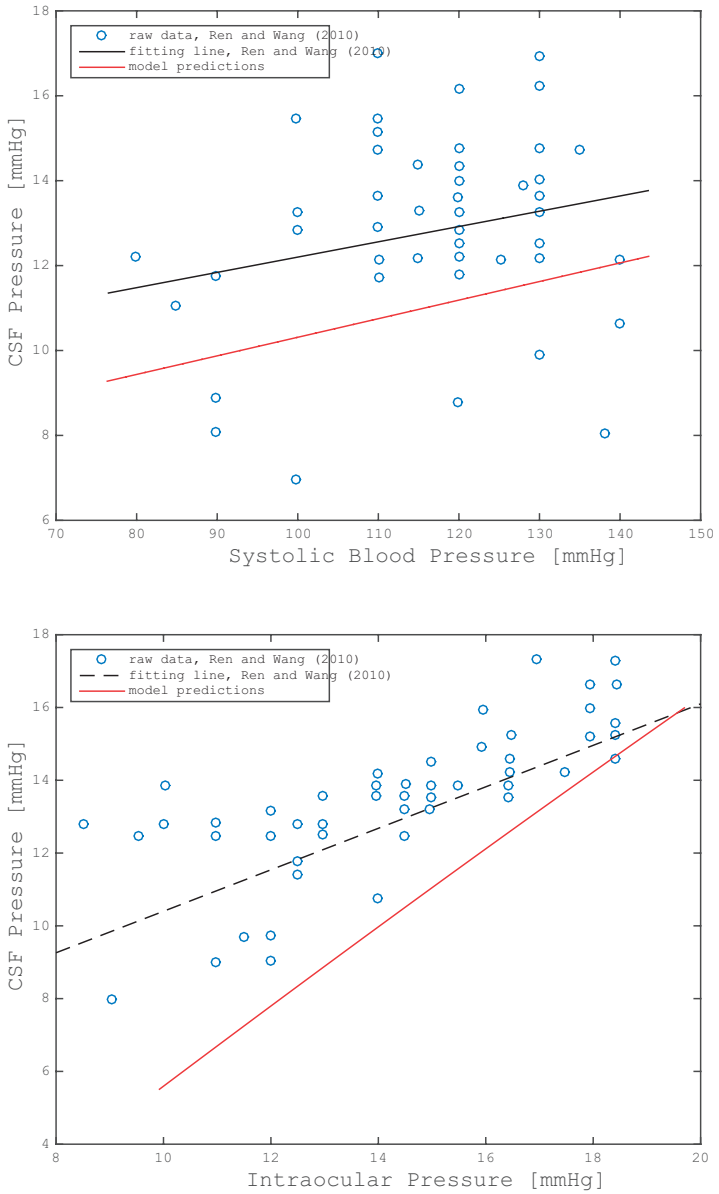


Fig. 1. (Top) Influence of systolic blood pressure on CSF pressure. (Bottom) Relationship between IOP and CSF pressure.

Table 1. Influence of systolic and diastolic blood pressures on IOP. Comparison between population-based studies and model simulations.

Source	mmHg increase in IOP/10 mmHg increase in SBP	mmHg increase in IOP/ 10 mmHg increase in DBP
Dielemans <i>et al.</i> ⁷	0.23 ± 0.02	0.24 ± 0.04
Mitchell <i>et al.</i> ⁸	0.28 ± 0.05	0.52 ± 0.12
Xu <i>et al.</i> ⁹	-	0.39
Model Predictions	0.42	0.83

IOP: intraocular pressure; SBP: systolic blood pressure; DBP: diastolic blood pressure

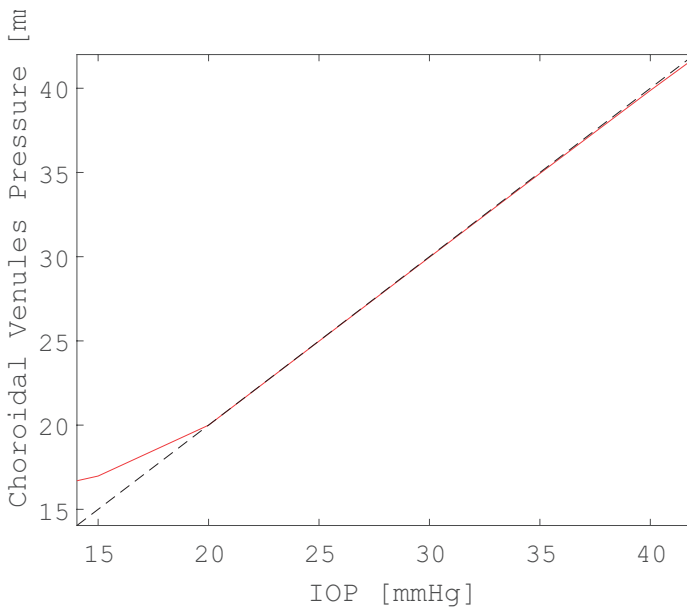


Fig. 2. Choroidal venules pressure vs IOP as predicted by the model (red curve). The black dashed line corresponds to equality between the two pressures.

from flow and pressure distribution within the body results to be approximately equal to IOP over a wide range of values (Fig. 2), confirming the findings by Bill.⁶ Differences between model predictions and clinical data might be due to blood flow regulation (currently not included) or particular conditions of clinical studies.

4. Conclusions and future perspectives

Simulation results validate the predictive capability of the model, which provides a powerful virtual laboratory where the relationships between IOP, P_A , and CSF pressure can be assessed based on patient-specific conditions. Thus, our model may have an important clinical role as medicine is moving in the direction of individualized treatments for specific patients.

References

1. Lakin WD, Stevens SA. Modelling the Response of Intracranial Pressure to Microgravity Environments. *Aspects of Mathematical Modelling*. Springer, 2008;211–227.
2. Guidoboni G, Harris A, Cassani S, et al. Intraocular pressure, blood pressure, and retinal blood flow autoregulation: a mathematical model to clarify their relationship and clinical relevance. *Invest Ophthalmol Vis Sci*. 2014;55(7):4105–4118.
3. Kiel JW, Hollingsworth M, Rao R, Chen M, Reitsamer HA. Ciliary blood flow and aqueous humor production. *Prog Retin Eye Res*. 2011;30(1):1–17.
4. Szopos M, Cassani S, Guidoboni G, et al. Mathematical modeling of aqueous humor flow and intraocular pressure under uncertainty: towards individualized glaucoma management. *Journal for Modeling in Ophthalmology*. 2016;1(2):29–39.
5. Ren R, Jonas JB, Tian G, et al. Cerebrospinal fluid pressure in glaucoma: a prospective study. *Ophthalmology*, 2010;117(2): 259–266.
6. Bill A. The uveal venous pressure. *Arch Ophthalmol*. 1963;69(6):780–782.
7. Dielemans I, Vingerling JR, Algra D, Hofman A, Grobbee DE, de Jong PT. Primary open-angle glaucoma, intraocular pressure, and systemic blood pressure in the general elderly population: the Rotterdam Study. *Ophthalmology*. 1995;102(1):54–60.
8. Mitchell P, Lee AJ, Wang JJ, Rochtchina E. Intraocular pressure over the clinical range of blood pressure: Blue Mountains Eye Study findings. *Am J Ophthalmol*. 2005;140(1):131–132.
9. Xu L, Wang H, Wang Y, Jonas JB. Intraocular pressure correlated with arterial blood pressure: the Beijing Eye Study. *Am. J. Ophthalmol*. 2007;144(3):461–462.



A simulation study on the effect of ionic currents on transmission from cones to retinal OFF type cone bipolar cells

Akito Ishihara

Department of Mechanical and Systems Engineering, School of Engineering, Chukyo University, Nagoya, Japan

Keywords: glutamate receptor, ionic current light response, retinal OFF type bipolar cell

1. Background and purpose

The retinal cone bipolar cells are interneurons which receive inputs from cone photoreceptors and send outputs to retinal ganglion cells. Several subtypes of bipolar cells have been identified by morphology and electrophysiology in the mammalian retina, which convey distinct visual information to higher order neurons in parallel.¹ The neural circuit in the retina not only converts light information to neural information, but also performs visual information preprocessing that has not yet been fully understood. Recently, it has been revealed that the neural circuits in retinas of higher vertebrates, such as mammals and primates, have various biophysical properties arising from being composed of ionic channels, ionic pumps, and neurotransmitter receptors. Analysis using a mathematical model based on their ionic mechanisms is essential to understand the visual information processing in the retinal neural circuit of the higher vertebrates.

The cones and the bipolar cells respond to continuous variation of light with a graded potential, in an analog manner. Especially, glutamate is continuously released from a cone synapse in the dark and is decreased by hyperpolarization of the

Correspondence: Akito Ishihara, 101-2 Yagoto-honmachi, Showa-ku, Nagoya, 466-8666 Japan. E-mail: aishi@sist.chukyo-u.ac.jp

cone that receives the light stimulus. The alpha-amino-3-hydroxy-5-methyl-4-isoxazolepropionic acid (AMPA) and kainate type ionotropic glutamate receptors (iGluRs) of the OFF type bipolar cells (OFF-BCs) exhibit partial or nearly complete desensitization in the sustained presence of glutamate.²⁻⁴ In the dark, glutamate concentration in the synaptic cleft of the cone pedicle rises to 0.1–0.5 mM.^{5,6} The baseline glutamate concentration depends on a sustained hyperpolarization of the cone by light. Thus, for understanding the working of the OFF-BCs, it is important to elucidate the mechanisms of synaptic transmission from cones to OFF-BCs via iGluRs, which undergo desensitization in the various background light conditions. Furthermore, there are various kinds of ionic channels in OFF-BCs that mediate membrane potential responses.⁷⁻⁹ It is considered that information transmitted from cones to OFF-BCs is modulated by the intrinsic ionic currents. We analyzed how ionic currents of OFF-BCs contribute to the transmission of light responses by developing a mathematical model.

2. Methods

To analyze the effect of ionic currents on transmission properties from cones to OFF-BCs, we constructed a mathematical model based on their ionic currents, as shown in the left panel in Figure 1. The OFF-BC model consists of an iGluR-mediated current and two voltage-dependent ionic currents in the soma, a delayed rectifying potassium current ($i_{Kv}(t)$), and an inward rectifying current ($i_h(t)$). The models of these ionic currents have already been proposed in our previous research.^{10,11} Briefly, the parameters of $i_{Kv}(t)$ and $i_h(t)$ which are described by the Hodgkin-Hux-

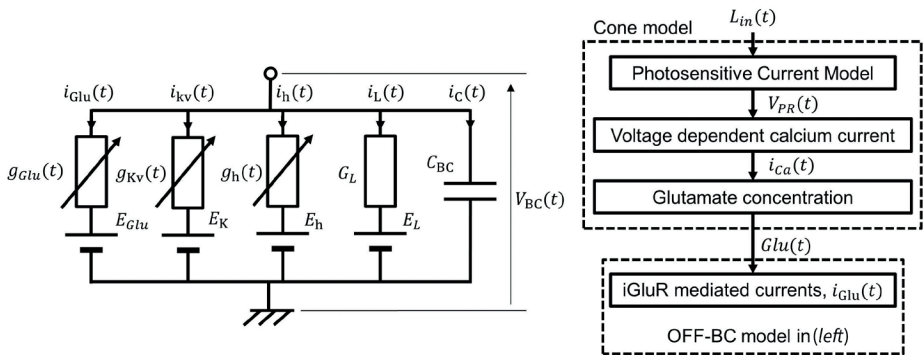


Fig 1. (Left) OFF-BCs were modeled by a parallel conductance model that introduced an iGluR-mediated current ($i_{Glu}(t)$), a delayed rectifying potassium current ($i_{Kv}(t)$), an inward rectifying current ($i_h(t)$), and a leakage current ($i_L(t)$). (Right) Glutamate concentration ($Glu(t)$) in the postsynaptic site was modulated by voltage-dependent calcium current ($i_{Ca}(t)$), which was inactivated by membrane hyperpolarization of the cone ($V_{PR}(t)$).

ley type equation, were re-estimated by using electrophysiological data from the mammalian retina.^{7,8}

The simulations of light responses of OFF-BCs were calculated by a network model which was constructed by adding the cone model¹² to the OFF-BC model. The membrane potential of the cone model ($V_{PR}(t)$) was hyperpolarized to light stimuli by a photo-sensitive current. After the membrane potential change at the inner segment propagates to the cone pedicle, the hyperpolarization reduces glutamate release due to inactivation of the voltage dependent calcium current (i_{Ca}). The response of glutamate concentration ($Glu(t)$) at the postsynaptic site was modeled simply with the i_{Ca} system.¹³

Some model parameters were not able to be estimated due to lack of physiological data. We analyzed the effect of the model parameters on synaptic transmission properties and light responses of OFF-BCs. Numerical solutions and computer simulations were obtained using the developed model and run using Matlab (Mathworks, Natick, MA, USA).

3. Results

We computationally analyzed the effect of the kinetics of iGluR-mediated currents and somatic voltage-dependent currents on responses of OFF-BCs to sinusoidal glutamate inputs. The left panel in Figure 2 shows the simulated responses of the OFF-BC model (Fig. 2, bottom left) to sinusoidal glutamate inputs (Fig. 2, top left). The baseline of V_{BC} was hyperpolarized and the amplitude of V_{BC} response was increased when glutamate concentration was decreased (Fig. 2, blue line in left panel). The right panel in Figure 2 shows the relationship of the peak-to-peak amplitude of the V_{BC} (V_{pp}) with the temporal frequency of inputs. The responses under high glutamate concentration showed a band-pass filtering feature (Fig. 2, black open circles in right panel), whereas the frequency profile showed a low-pass filtering manner in the low baseline glutamate concentrations (Fig. 2, blue filled circles in right panel). Our analysis of the model responses (data not shown) showed that the upper cutoff frequency of the band-pass filtering responses depends on the rate of desensitization of iGluR and the membrane time constant, which is given by the membrane capacitance (C_{BC}), the sum of the leakage conductance (G_L), and other ionic conductance. The frequency characteristics also depend on i_{Kv} and i_h . V_{pp} to low-frequency inputs were decreased with increased maximal conductance of i_{Kv} and i_h (Fig. 2, open circles in right panel), when at least one of the i_{Kv} or i_h was activated at V_{BC} . These results suggest that transmission of temporal low-frequency signals in OFF-BCs depends on the baseline glutamate concentrations in the postsynaptic site, which are mainly controlled by the mean light intensity. This also suggests that the components of OFF-BC responses are modified by ionic current rectification of the membrane.

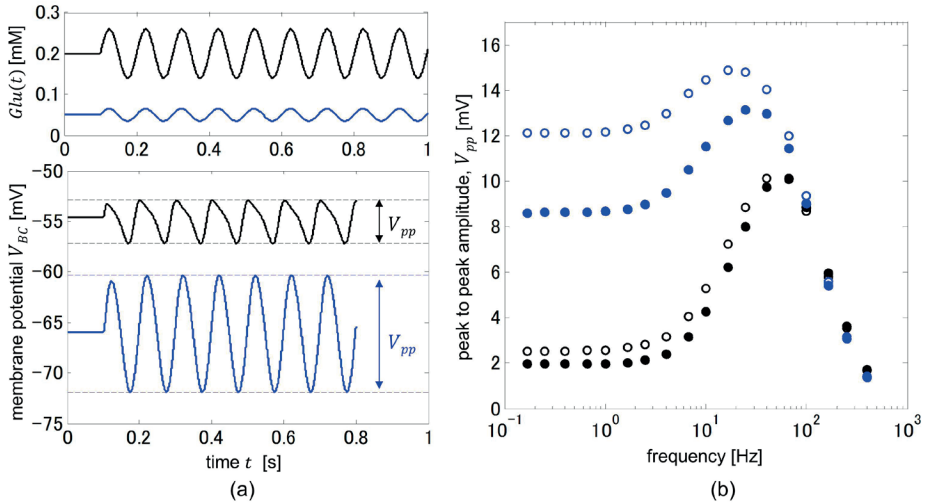


Fig 2. (Left) Time course of membrane potential responses of the OFF-BC model (V_{BC} , bottom) to sinusoidal glutamate wave inputs (top) with frequency of 10 Hz and amplitude of 30% of the baseline value of 0.2 mM (black line), 0.05 mM (blue line). (Right) The peak-to-peak amplitude of V_{BC} (V_{pp} , the arrows in (left)) were plotted versus the frequency of the sinusoidal stimulus under a baseline glutamate concentration of 0.2 mM (black circles), 0.05 mM (blue circles). Open circles indicate the frequency characteristics of the model without i_{KV} and i_h ; filled circles with i_{KV} and i_h .

We next analyzed the effect of ionic mechanisms in OFF-BCs to light responses of the cells by using the network model of a cone and an OFF-BC. OFF-BC responses showed a stronger temporal band-pass filtering feature (Fig. 3, bottom left) than cone responses (Fig. 3, top left). In the cone, the frequency relationship of responses to mean intensity of 4000 td (Fig. 3, black circles in left panel) were the same as that to a mean intensity of 10000 td (Fig. 3, blue circles in left panel). In the OFF-BC, the aforementioned frequency relationship is different in both of the mean intensities (Fig. 3, bottom left). The right panel in Figure 3 shows the time courses of $V_{PR}(t)$, $Glu(t)$ and $V_{BC}(t)$ with response to a mean intensity of 4000 td (Fig. 3, black dashed lines in right panel) and 10000 td (Fig. 3, blue solid lines in right panel). The ratio (C, Fig. 3, in set in right panel) of peak-to-peak amplitudes of OFF-BC fluctuation response to a mean intensity of 10000 td and 4000 td was greater than 1, although the ratio of amplitudes of $Glu(t)$ response was nearly equal to 1. The results suggest that the difference of the frequency characteristics of OFF-BC response was produced by the iGluR current and their somatic ionic currents.

OFF-BC responses were strongly attenuated by the light stimulus with a mean intensity of 1000 td, under which both the cones and rods act. In this dark condition,

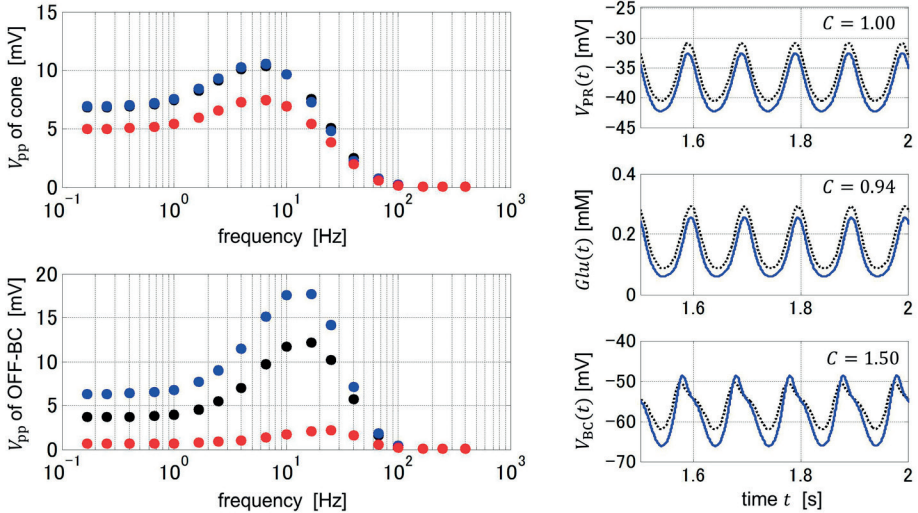


Fig 3. (Left) Relationship V_{pp} of the cone model (top) and the OFF-BC model (bottom) with the frequency of sinusoidal light inputs with amplitude of 60% of mean intensities of 1000 td (red circles), 4000 td (black circles), and 10000 td (blue circles). (Right) Time course of the response of $V_{PR}(t)$ (top), $Glu(t)$ (middle), and $V_{BC}(t)$ (bottom) to sinusoidal light stimulus with a frequency of 10 Hz. The black dashed lines indicate responses under the mean intensity of 4000 td and the blue solid lines indicate those under 10000 td. The values of C (in set) express the ratio between the V_{pp} of responses to the mean intensity 10000 td/4000 td.

the glutamate concentration in the postsynaptic site was high. Therefore, the OFF-BC responses were suppressed by desensitization of iGluRs and depolarization of mean membrane potential (Fig. 2, black line in left panel). Our simulation analysis using square pulse light waves demonstrated that the OFF-BC transmit temporal transient signals such as ON-OFF signals under the dark-illumination condition.^{10,14}

4. Conclusions and future perspectives

The results show that the temporal frequency responses of the OFF-BCs depend on the iGluR current and the somatic ionic currents. Moreover, its characteristics are modulated by mean illumination. These results suggest that the iGluR current acts to transmit low pass filtering signals under the day-light condition and it acts to attenuate temporal low-frequency signals under the dark condition. Furthermore, the results suggest that somatic ionic currents i_{KV} and i_h also attenuate low-frequency signals of high mean light intensity.

Our simulated results showed that the transmission from a cone to an OFF-BC adaptively change with mean light intensity in the mammalian retina. It has been

reported that bipolar cells in the mammalian retina have voltage-gated sodium channels^{6,15} and some subtypes of the cells respond to light with a spike.¹³ Since the sodium channels are activated from a hyperpolarized potential to depolarization, it is possible that light responses under dark conditions are affected by current through the channels, if there are channels in OFF-BCs. Other ionic currents such as calcium-dependent currents have been reported in the synaptic terminal of bipolar cells.¹ By modeling the bipolar cells with integration of these ionic mechanisms, we can help elucidate how these cells play a role in visual information processing.

The five types of OFF-BCs in the mammalian retina are characterized by the temporal response to glutamate application.^{3,4} It is expected that OFF signals of visual information could be processed in parallel by these five channels.⁴ With the improvement of our model based on the electrophysiological evidence, we expect that visual information processing in the OFF pathway of the higher vertebrate retina will be clarified in detail, especially with respect as to why the five channels are needed.

Acknowledgements

This research was partially supported by the Ministry of Education, Culture, Sports, Science and Technology (Japan) through a Grant-in-Aid for Scientific Research (C), 25330353.

References

1. Euler T, Haverkamp S, Schubert T, Baden T. Retinal bipolar cells: elementary building block of vision. *Nat Rev Neurosci.* 2014;15:507-519.
2. DeVries SH. Bipolar cells use kainate and AMPA receptors to filter visual information into separate channel. *Neuron.* 2000;28:847-856.
3. Lindstrom SH, Ryan DG, Shi J, DeVries SH. Kainate receptor subunit diversity underlying response diversity in retinal Off bipolar cells. *J Physiol.* 2014;592:1457-1477.
4. Ichinose T, Hellmer CB. Differential signalling and glutamate receptor compositions in the Off bipolar cell types in the mouse retina. *J Physiol.* 2016;596:883-894.
5. DeVries SH, Li W, Sazik S. Parallel processing in two transmitter microenvironments at the cone photoreceptor synapse. *Neuron.* 2006;50:735-748.
6. Nielson TA, DiGregorio DA, Silver RA. Modulation of glutamate mobility reveals the mechanism underlying slow-rising AMPAR EPSCs and the diffusion coefficient in the synaptic cleft. *Neuron.* 2004;42:757-771.
7. Pan Z, Hu H. Voltage-dependent Na⁺ current in mammalian retinal cone bipolar cells. *J Neurophysiol.* 2000;84:2564-2571.
8. Hu H, Pan Z. Differential expression of K⁺ currents in mammalian retinal bipolar cells. *Vis Neurosci.* 2002;19:163-173.
9. Ma Y, Cui J, Hu H, Pan Z. Mammalian retinal bipolar cells express inwardly rectifying K⁺ currents (Ikir) with a different distribution than that of Ih. *J Neurophysiol.* 2003;90:3479-3489.

10. Usui S, Ishihara A, Kamiyama Y. Ionic current model of bipolar cells in the lower vertebrate retina. *Vis Neurosci.* 1996;36:4069-4076.
11. Ishihara A. Simulation analysis of temporal coding by ionotropic glutamate receptors of retinal Off-type bipolar cells. *Sensor and Materials* 2018;30:299-313.
12. van Hateren JH, Snippe HP. Simulating human cones from mid-mesopic up to high-photopic luminances. *J Vis.* 2007;7:1-11.
13. Ishihara A, Kamiyama Y, Usui S. Analysis of light response of the retinal bipolar cells based on ionic current model. *Computational Neuroscience: Trend in Research*. New York: Plenum Press, 1998; 203-209.
14. Ishihara A. Simulation study of information transmission in OFF cone bipolar cell pathway. ARVO Annual Meeting. Honolulu, HI, 2018; Abstract 1873-C0177.
15. Ma Y, Cui J, Pan Z. Heterogeneous expression of voltage-dependent Na⁺ and K⁺ channel in mammalian retinal bipolar cells. *Vis Neurosci.* 2005;22:119-133.
16. Ichinose T, Shields CR, Lukasiewicz PD., Sodium channels in transient retinal bipolar cells enhance visual responses in ganglion cells. *J Neurosci.* 2005;25:1856-1865.



A model for tear film dynamics during a realistic blink

Kara L. Maki¹, William D. Henshaw², Alex McManus¹, Richard J. Braun³, Dylan M. Chapp³, Tobin A. Driscoll³

¹School of Mathematical Sciences, Rochester Institute of Technology, Rochester, NY, USA, ²Department of Mathematical Sciences, Rensselaer Polytechnic Institute, Troy, NY, USA, ³Department of Mathematical Sciences, University of Delaware, Newark, DE, USA

Keywords: blink, tear breakup, tear film, thin film equation

1. Background and purpose

Each time one blinks, a stable tear film (TF) must reestablish itself on the ocular surface to ensure the function and health of the eye. Although the formation of the TF has been extensively studied both experimentally and theoretically,^{1,2} the influence of the lid dynamics on the TF formation is still not fully understood. Experimental instrumentation does not yet have the capability to estimate the TF thickness *in vivo* over the entire front of the eye, especially near the lids during a blink, where the eyelashes obstruct the view of the ocular surface. Additionally, a realistic blinking eye-shaped domain presents challenges in approximating the motion of the TF in theoretical studies. In this work, we overcome these theoretical challenges by implementing a moving overset grid method to study the influence of the lid motion on the formation of TF.

2. Methods

The realistic eye-shaped domain is described by curves fit to the lid margin of a partial blinking eye. Figure 1 shows one frame from a video of a partial blink, and the curve fit to the lid margin. In each frame of the video, a Fourier series in space, with fifteen nodes, is fit using a least-squares approximation to the lid margin data. Next, each coefficient of the Fourier series describing the lid margin in each frame of the video is treated as a time series of data and fit to a Fourier series in time with five nodes. Thus, the shape of the eye, and boundary of our domain, $\partial\Omega(t)$, can be characterized at any given time during the partial blink.

Correspondence: School of Mathematical Sciences, Rochester Institute of Technology, Rochester, NY, USA.

E-mail: kmaki@rit.edu

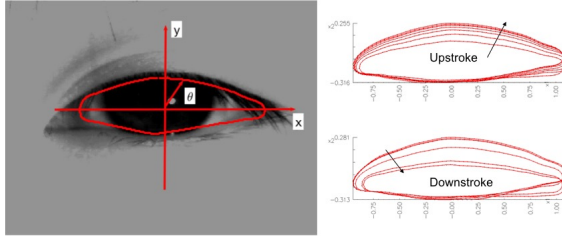


Fig. 1. (Left) Frame from a video of a blink with the curve approximating the lid margin. (Right) A family of curves approximating the lid margin during the upstroke (top) and the downstroke (bottom).

Here, we describe our mathematical model for the evolution of the aqueous layer thickness of the TF, denoted by $z = h(x, y, t)$. We assume the TF is aqueous tears with fluid properties matching water and viscosity μ . In this work, we ignore gravitational effects. On the ocular surface, approximated as the plane, $z = 0$, we assume no slip and impermeability. At the TF/air interface, $z = h(x, y, t)$, we assume the lipid layer has rendered the surface tangentially immobile, and the difference in the normal stresses across the interface is equal to capillary pressure due to surface tension σ . The characteristic length scale for the ocular surface is $L = 2$ cm, whereas the characteristic thickness of the tears is $H = 16 \mu\text{m}$.³ The aspect ratio $\epsilon = H/L = 8 \times 10^{-4}$ arises as a small parameter when we nondimensionalize the Navier-Stokes equations; we then apply lubrication theory⁴ to derive a thin film equation for the TF thickness:

$$\frac{\partial h}{\partial t} = \nabla \cdot \left(\frac{h^3}{12} \nabla p \right), \quad (1)$$

$$p = -S\Delta h, \quad (2)$$

on $(x, y) \in \Omega(t)$, where $p(x, y, t)$ denotes the pressure of the aqueous tears. The nondimensional parameter $S = \epsilon^3 \sigma / \mu V \approx 7.8 \times 10^{-7}$ characterizes the relative importance of viscous and capillary effects. Changes in h are determined by spatial variations in the aqueous volumetric flux, $\mathbf{Q} = -\frac{h^3}{12} \nabla p$. Note that we solve the problem as a system of nonlinear partial differential equations (PDEs) to facilitate the numerical approximation of the solution.^{5,6}

To close the system of PDEs, we enforce boundary conditions (BCs) to mimic realistic TF dynamics. The first specifies the TF meniscus width at the lid margins; specifically, we set $h|_{\partial\Omega(t)} = h_0 = 13$; dimensionally, $208 \mu\text{m}$ falls into the range of reported average values for the tear meniscus width h_0 from $6 \times 10^{-5} \text{ m}$,^{7,8} to $3.65 \times 10^{-4} \text{ m}$.⁹ The second BC specifies the flux of fluid entering and exiting the exposed ocular surface; the flux may be chosen to mimic the lacrimal system as characterized by Doane.¹⁰ Specifically, we may specify the aqueous volumetric flux, \mathbf{Q} , normal to the boundary:

$$\mathbf{Q}(\theta, t) \cdot \mathbf{n}_{\partial\Omega}(\theta, t) = Q_{lm}(\theta, t) + Q_{lg}(\theta, t) + Q_p(\theta, t), \quad (3)$$

where $\mathbf{n}_{\partial\Omega}(\theta, t)$ is the normal vector to lid margins at position θ and time t ; θ is the angle relative to the positive x -axis, with the y -axis at $\theta = \pi$; $Q_{lm}(\theta, t)$ is the flux proportional to lid motion (FPLM); $Q_{lg}(\theta, t)$ is the lacrimal gland influx; and $Q_p(\theta, t)$ is the punctal drainage efflux. In this work, we assume that during lid motion, the lacrimal gland supply and punctal drainage are not active, *i.e.*, $Q_{lg} = Q_p = 0$, and the FPLM is given by:

$$Q_{lm}(\theta, t) = h_{lm} \mathbf{v}_{\partial\Omega}(\theta, t) \cdot \mathbf{n}_{\partial\Omega}(\theta, t), \quad (4)$$

where $\mathbf{v}_{\partial\Omega}(\theta, t)$ is the velocity of the lid, found by taking the time derivative of the double Fourier series representation of the lid margin.¹¹ When $h_{lm} = h_0$, the tear volume is conserved during the blink. When $h_{lm} = h_0 - h_e/2$, we assume there exists a layer of aqueous tears of thickness h_e under the lid margins and there is a Couette flow between the unexposed eye surface and the lids that enters and exits the TF during the blink.¹¹ In the results presented below, $h_e = 1.6$ (12% of the tear meniscus width).

The initial TF thickness and pressure distributions are shown in Figure 2. The initial TF distribution is found by solving $p = -S\Delta h$, where the pressure distribution is specified by $p = -S(3.5x^4 + 2y^2 + 1)$, chosen to mimic features seen *in vivo*. The initial dimensional tear volume is 21.25 μl which is eight times the 2.45 μl volume of the TF estimated *in vivo* on an open eye.¹²

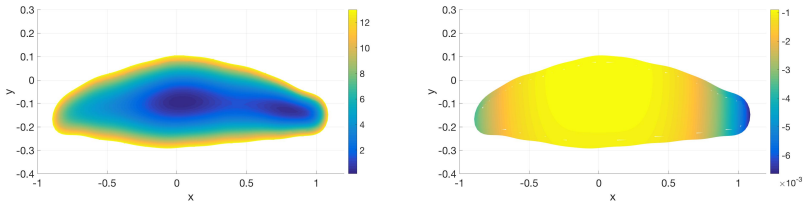


Fig. 2. The initial TF thickness (*left*) and pressure distribution (*right*).

The evolution equations (1) and (2) are approximated using an overset moving grid method in *Overture* (<http://www.overtureframework.org>). The eye-shaped domain is discretized using moving overlapping grids (a collection of logically rectangular curvilinear component grids) where a boundary-fitted grid is used to represent the moving lids, and this grid overlaps with a stationary background Cartesian grid.^{13,14} Each component grid is defined by a smooth mapping from computational space (the unit square) to the physical domain. The governing equations are transformed to the unit square and then discretized in space using standard finite difference approximations. On the moving boundary-fitted grid, the equations are solved in a moving coordinate system. The solutions on the different component grids are connected by interpolation. The nonlinear equations are advanced in time using a second-order accurate backward-differentiation (BDF) scheme. The numerical accuracy has been verified on test problems with exact solutions.¹⁵

3. Results

We validated the performance of the numerical approach on the current problem by analyzing the conservation of the TF volume during the blink with no flux BCs. The volume change is less than 2% of the initial tear volume for the entire blink cycle.

We now examine how different flux BCs, linked to lid motion and lid speed, affect the tear formation and subsequent TF breakup times.

3.1 TF formation: the upstroke

We first consider the no flux BC where TF volume is conserved. The left panel in Figure 3 shows the evolution of the TF during the upstroke. As the upper lid opens, the TF thins along the lid margin as more eye surface is exposed, thus creating the black line (shown as dark blue). The local thinning near the upper lid is consistent with prior work with 1-D models.² However, now we can see how spatial variation in the lid motion affects TF formation. In this model, the black line first forms in the center of the eye ($\theta \approx \pi/2$) and then extends towards the temporal canthus ($\theta \approx 0$). The thinning continues as more eye surface is exposed, causing the radius of curvature of the upper meniscus to decrease. This creates an even lower pressure region in the upper meniscus and accelerates meniscus-induced thinning.

The right panel in Figure 3 shows the evolution of the TF during the upstroke, when aqueous tears are supplied from under the lids via the FPLM BC. The supplied tears suppress the formation of the black line along the upper lid margin. We still see evidence of the meniscus-induced thinning in the corners, with the black line first appearing in the temporal canthus.

The different flux BCs result in different TF distributions at the end of the upstroke and the end of the downstroke. Figure 4 compares the TF thickness after the upstroke ($t = 1$) and a complete blink ($t = 3/2$). Unsurprisingly, in the upper meniscus, the no flux BC simulation results in a thinner TF than with FPLM BC. In the center of the exposed area, the difference in the thickness at the end of upstroke is nearly zero; the effect of the flux BCs is localized to the menisci regions. Interestingly, at the end of the downstroke, in the center of the exposed area, the no flux BC yields a thicker TF than for the FPLM BC. The "snow plow" effect of the upper lid during the downstroke causes more global thickness variation.

3.2 Tear relaxation: the interblink

Figure 5 shows the continuation of the tears supplied under lids during the upstroke into the interblink period. After completion of the upstroke, the eye remains open for ~ 2 seconds. The figure shows the TF thickness and the aqueous flux after the eye remains open for approximately 1.5 seconds. Meniscus-induced thinning continues to form the black line. As found in the prior work on a stationary eye-shaped domain,^{4,16} the tears in the lower meniscus collect near the canthi due to the increased curvature of the lid margin. An interesting flow pattern develops in the upper meniscus. In the

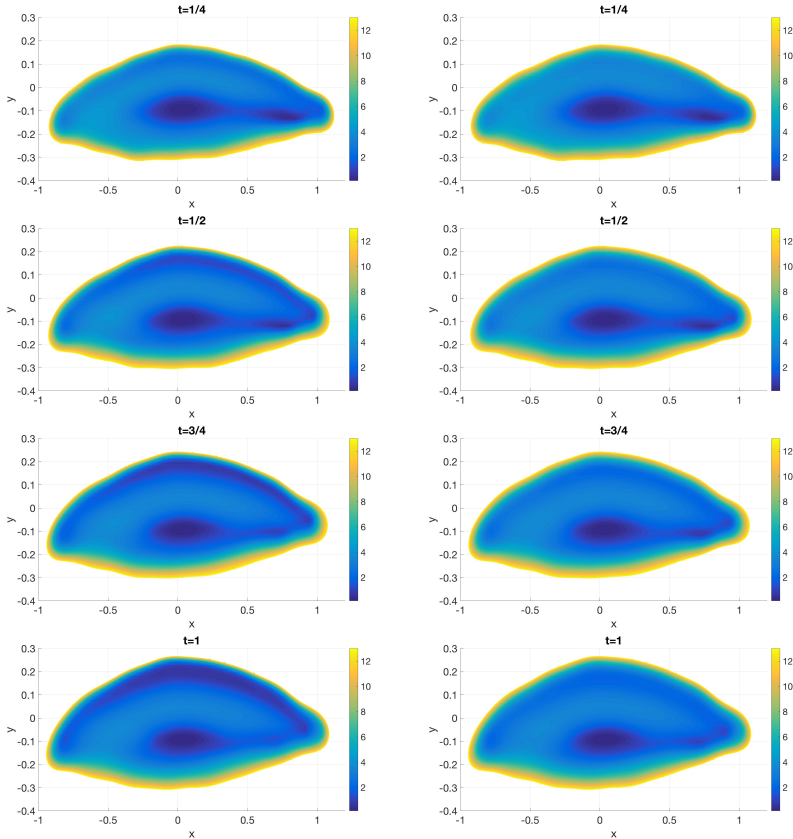


Fig. 3. (Left) TF thickness during the upstroke, when the volume is conserved (no flux BC). (Right) TF thickness using the FPLM BC, where the upper lid exposes aqueous tears from under the lid.

nasal canthus, the tears continue to flow into the upper meniscus region towards the temporal canthus. Unlike previous work on the stationary domain, we find the lower-pressure region that forms in the upper meniscus during the upstroke continues to draw fluid into the upper meniscus after the lid motion has stopped. These spatial variations in the upper tear meniscus curvature at the end of the upstroke (and consequently, the pressure) depend on spatial variations in the lid speed and influxes. We note that adding punctal drainage and lacrimal gland supply may reverse that flow.

4. Conclusions and future perspectives

We find the formation of the TF during the upstroke is sensitive to the lid motion and the tear supply from under lids. The local tear film thinning in the upper meniscus is dependent on the rate of the exposure of the eye surface and the influxes/effluxes.

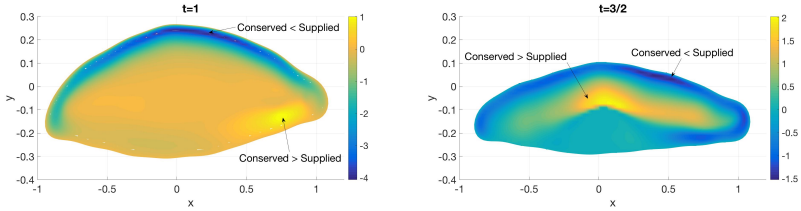


Fig. 4. The difference in the thickness distribution between the no flux and FLPM BCs. (Left) The end of the upstroke ($t = 1$). (Right) The end of the downstroke ($t = 3/2$).

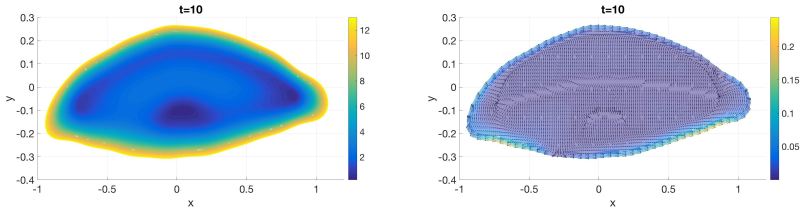


Fig. 5. Relaxation of the TF during the interblink. The TF thickness and aqueous flux after the eye has been open for 1.5 seconds.

Any spatial variation in the local tear film thinning rates establishes a flow within upper meniscus region. During the interblink period, we found that the curvature of the lid margin can accelerate the formation of the black lines by establishing low-pressure regions in the menisci. In future work, the model described here should be extended to include gravitational and evaporative effects, and more realistic influxes/effluxes to provide insight into the tear film dynamics near the upper lid during a blink, a region that is difficult to image.

Acknowledgements

This material is based upon work supported by the National Science Foundation (NSF) under Grant Numbers DMS 1412141 (KLM) and 1412085 (RJB and TAD), and does not necessarily represent the official view of the NSF.

References

1. Braun R, King-Smith P, Begley C, Li L, Gewecke N. Dynamics and function of the tear film in relation to the blink cycle. *Prog Ret Eye Res.* 2015;45: 132–164.
2. Braun RJ. Dynamics of the tear film. *Annu Rev Fluid Mech.* 2012;44: 267–297.
3. King-Smith E, Fink B, Hill R, Koelling K, Tiffany J. The thickness of the tear film. *Curr Eye Res.* 2004;29(4-5): 357–368.
4. Maki KL, Braun RJ, Ucciferro P, Henshaw WD, King-Smith PE. Tear film dynamics on an eye-shaped domain. Part 2. Flux boundary conditions. *J Fluid Mech.* 2010;647: 361–390.

5. Heryudono A, Braun RJ, Driscoll TA, Cook LP, Maki KL, King-Smith PE. Single-equation models for the tear film in a blink cycle: Realistic lid motion. *Math Med Biol.* 2007;24: 347–377.
6. Maki KL, Braun RJ, Driscoll TA, King-Smith PE. An overset grid method for the study of reflex tearing. *Math Med Biol.* 2008;25: 187–214.
7. Mainstone JC, Bruce AS, Golding TR. Tear meniscus measurement in the diagnosis of dry eye. *Curr Eye Res.* 1996;15(6): 653–661.
8. Golding TR, Bruce AS, Mainstone JC. Relationship between tear-meniscus parameters and tear-film breakup. *Cornea.* 1997;16(6): 649–661.
9. Gaffney E, Tiffany J, Yokoi N, Bron A. A mass and solute balance model for tear volume and osmolarity in the normal and the dry eye. *Prog Ret Eye Res.* 2010;29(1): 59 –78.
10. Doane MG. Blinking and the mechanics of the lacrimal drainage system. *Ophthalmology.* 1981;88: 844–851.
11. Jones MB, Please CP, McElwain DLS, Fulford GR, Roberts AP, Collins MJ. Dynamics of tear film deposition and drainage. *Math Med Bio.* 2005;22: 265–288.
12. Mishima S, Gasset A, Klyce SD, Baum JL. Determination of tear volume and tear flow. *Ophthalmol Vis Sci.* 1966;5: 264–276.
13. Chesshire G, Henshaw WD. Composite overlapping meshes for the solution of partial differential equations. *J Comput Phys.* 1990;90: 1–64.
14. Henshaw WD, Schwendeman DW. Moving overlapping grids with adaptive mesh refinement for high-speed reactive and non-reactive flow. *J Comput Phys.* 2006;216(2): 744 –779.
15. Roache PJ. Verification of codes and calculations. *AIAA J.* 1998;36(5): 696–702.
16. Li L, Braun RJ, Maki KL, Henshaw WD, King-Smith PE. Tear film dynamics with evaporation, wetting and time-dependent flux boundary condition on an eye-shaped domain. *Phys Fluids.* 2014;26: 052101.



Automated classification of dry eye type analyzing interference fringe color images of tear film using machine learning techniques

Katsumi Yabusaki¹, Reiko Arita^{2,3}, Takanori Yamauchi⁴

¹Tokyo New Drug Research Laboratories, Kowa Company Ltd., Tokyo, Japan; ²Itoh Clinic, Saitama, Japan; ³Lid and Meibomian Gland Working Group, Tokyo, Japan; ⁴Chofu Factory, Kowa Company Ltd., Tokyo, Japan

Keywords: artificial intelligence, diagnostic support, dry eye disease, machine learning, type classification

1. Background and purpose

The unstable balance in secretions of lipids and aqueous fluid to tear film is a significant cause of dry eye disease (DED).^{1,2} Arita et al. demonstrated a simple but very effective method that classifies dry eye types to the aqueous deficient dry eye (ADDE) and the evaporative dry eye (EDE) by focusing on the dry eye type-unique appearances of interference fringe colors and patterns of tear films.³ We thought this simple classification is very helpful for diagnoses and treatments. However, diagnostic bias by unskilled observers remains an issue to be solved.³

The artificial intelligence (AI)-based support for diagnosis is one of the hottest topics in the field of ophthalmology research. We expected that the AI-based model would reduce bias in DED-type diagnoses. Many studies have been reported targeting retinal diseases like age-related macular degeneration and/or diabetic retinopathy. Most of the works established AI-based predicting models using images taken by fundus cameras and/or optical coherence tomography (OCT)

Correspondence: Katsumi Yabusaki, Kowa Company Ltd., 2-17-43 Noguchicho, Higashimurayama, Tokyo 189-0022, Japan.
E-mail: yabusaki@kowa.co.jp

devices to capture disease-related structural disorders.⁴⁻⁷ In contrast, the interference fringes dynamically change the colors and patterns spatiotemporally. To the best of our knowledge, there is no AI-based model studied for distinguishing ADDE and EDE using interference fringe images. However, an AI-based study classifying the condition of the tear lipid layer by analyzing the textures of interference fringes compared to the device-unique grades has been reported.⁸ This suggested the possibility of using the unstructured characteristics, such as colors and/or complexities of interference fringes, as the numerical image features when building AI-based prediction models. In this study, we first examined several types of image characteristics extracted from the colors and patterns of fringes to obtain effective image features for the DED-type classification. We then evaluated whether the AI-based models would have sufficient abilities for this type of prediction by comparing their diagnoses with those made by an ophthalmologist skilled in this classification (the founder of this type classification).³

2. Methods

The interference fringe of tear film is generated by the phase difference between reflected lights from the surface of the lipid layer and the border formed between lipid and water layers (Fig. 1). It seems the colors and appearances of interference fringes are primarily determined only by the lipid conditions; however, we consider that the balance of secreted amounts of lipid and water component in tear film is key to keep the appearance of the interference fringe at normal type. Therefore, the interference fringe would show a colorful and complex appearance (ADDE type) when the balance is off due to conditions such as excess secretion of the lipid component and/or shortage of the water component, since the excess amount of lipid might be pooled at the lower side of the corneal surface due to the shortage in upward movement of the tear film. The pooled lipids would induce an uneven thickness of lipid layer, and this could cause the colorful and complex appearance of the interference fringe.

Interference fringe images were taken with the Kowa DR-1 α tear interferometer (Kowa Company Ltd., Tokyo, Japan) at 5 seconds after blinking (Fig. 1A and B). We used these fringe images to build the linear support vector machine (SVM)-based machine learning (ML) models. We converted the unstructured properties (characteristics), such as fringe colors, color saturations, color diversities, and/or textures of fringes, to numerical values through several image processing techniques. These numerical values were normalized to range from 0 to 1 to define the image features used for this study. Examining image characteristics in a multifaceted manner, we finally chose a minimum necessary of 11 image features to build the models. A detailed definition of each image feature is shown in Table 1 and examples explaining how to extract the numerical values from interference fringe images are shown in

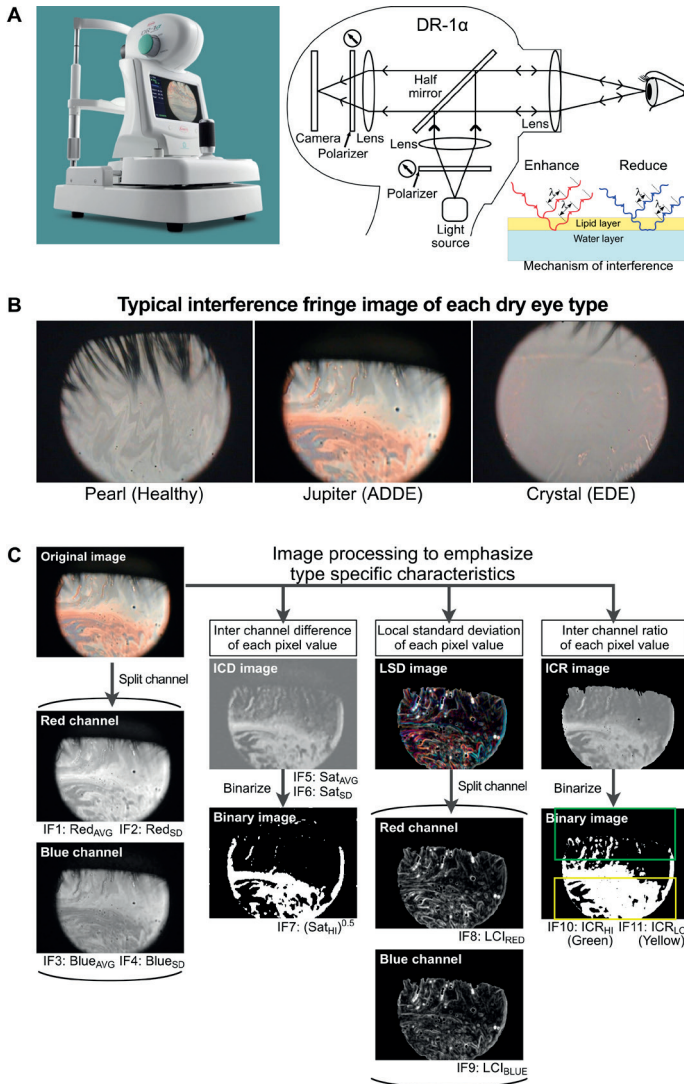


Fig. 1A. Typical interference fringe color images captured by the Kowa DR-1 α . (A) Interference fringes are generated on the surface of tear film under special illumination of the device. The colors of the fringes represent the thickness of the lipid layer, which covers the water layer of tear film. (B) Interference fringe images show dry-eye-specific colors and appearances. (C) Eleven image features (IFs) optimized to classify three dry-eye types were prepared by using several image processing techniques. IFs can be divided to three categories by the functions: 1. IFs represent color properties of IFCl (IF1 ~ IF6); 2. IFs show the existences of breakup of tear film (IF8 and IF9); and 3. IFs show the size and location of interference fringes (IF7, IF10, and IF11).

Table 1. Definitions of image features

ID	Name	Definitions of image features
IF1	RedAVG	Averaged pixel value of red channel of target area
IF2	RedSD	Standard deviation of red channel of target area
IF3	BlueAVG	Averaged pixel value of blue channel of target area
IF4	BlueSD	Standard deviation of blue channel of target area
IF5	SatAVG	Averaged pixel value of saturation of target area
IF6	SatSD	Standard deviation of saturation of target area
IF7	(SatHI)0.5	Square root of pixel number where saturation shows high level
IF8	LCIRED	Local complexity of pixel value of red channel of SD image
IF9	LCIBLUE	Local complexity of pixel value of blue channel of SD image
IF10	ICRHI	Averaged pixel value of upper area of inter-channel ratio (R/B) image
IF11	ICRLO	Averaged pixel value of lower area of inter-channel ratio (R/B) image

Figure 1C and Figure 2A. Image features were averages and/or standard deviations and/or region of interest (ROI) areas calculated from pixel values of color channels, and can be largely sorted into three classes:

1. class-1 represents color properties of interference fringes obtained as averaged pixel values of color channels (including IF1, IF3, and IF5);
2. class-2 indicates complexities of fringe appearance and/or colors determined by the variations of pixel colors for complexities of whole cornea areas or local cornea area (including IF2, IF4, IF6, IF8, and IF9); and
3. class-3 shows localizing areas of fringes and breakups of tear film in the corneal surface (including IF7, IF10, and IF11).

We collected 138 images (46 images were contained in each type) to build ML models. The models were trained using training images (including 31 randomly chosen images from each type, for a total of 93 images) and type predictions were examined using 45 residual images containing 15 images for each type, with averaged values and standard deviations calculated from 10-time-running using randomly chosen data from the data set. DED types predicted by the ML models were compared to ones diagnosed by a skilled ophthalmologist to obtain F-scores and Kappa coefficients. We also ranked image features by the significance in efficacies of type classification from the F-scores under independent use.

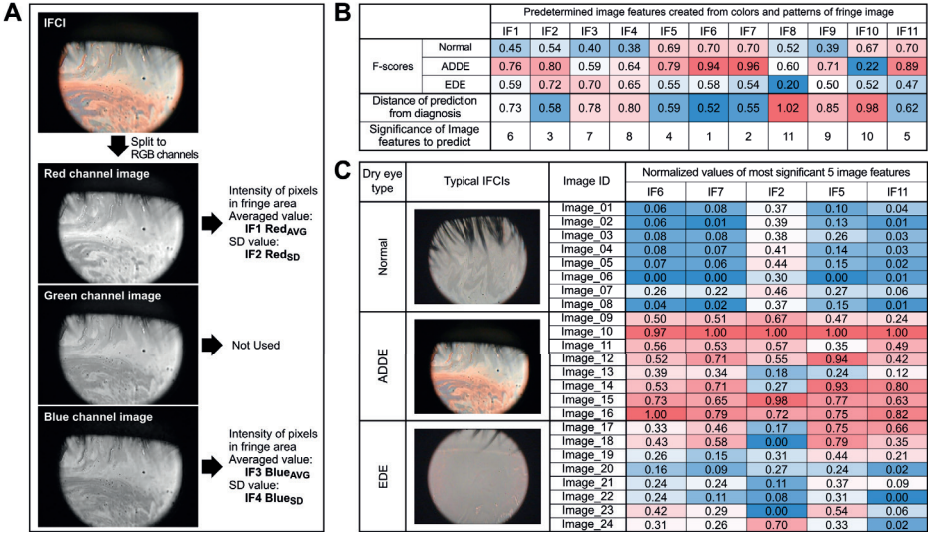


Fig 2. Definition and ability in independent use of each image feature. (A) An example of image processing to extract image features (IF1 – IF4) from the split channels of interference fringe image. Averaged pixel values (IF1: Red_{AVG} and IF3: $Blue_{AVG}$) and standard deviation values (IF2: Red_{SD} and IF4: $Blue_{SD}$) were calculated by only targeting the areas of interference fringe limited by thresholding values applied to pixel brightness. (B) Ability of each image feature to classify DED types under individual use. The abilities were indicated as F-scores and colored as heat map (blue for lower and red for higher values). Image features were ranked by the integrated ability of DED-type prediction (defined by Equation 1 as shown in Results section). (C) DED-type dependent trends were visualized by image feature values shown as heat map.

3. Results

First, we examined the ability of every single image feature to predict DED type. As shown in Figure 2B, the image feature defined as $Blue_{SD}$ (IF4) had the lowest contribution for normal-type prediction, while ICR_{LO} (IF11) had the highest contribution. Likewise, the lowest and highest image features for ADDE-type prediction were ICR_{HI} (IF10) and $(Sat_{HI})^{0.5}$ (IF7), respectively, while LCI_{RED} (IF8) and Red_{SD} (IF2) had the lowest and highest features for EDE-type prediction, respectively. Distance of prediction from diagnosis (DP), indicating combined error in the predicting performance of each image feature (lower value had lower error), was given by each F-score value (FS_{NORMAL} , FS_{ADDE} , and FS_{EDE}) as below:

$$DP = \frac{(1 - FS_{NORMAL}) + (1 - FS_{ADDE}) + (1 - FS_{EDE})}{3} \quad (1)$$

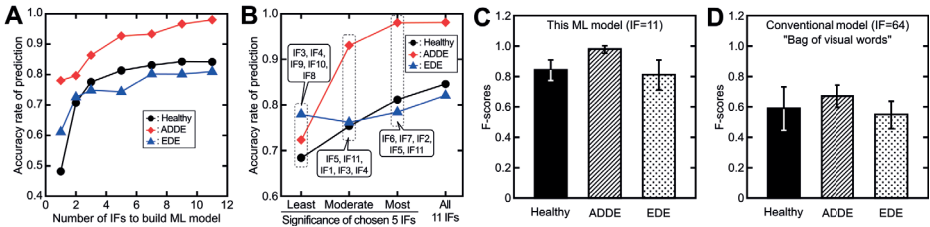


Fig 3. Accuracy rates of our ML model to predict DED type. (A) Dependencies of accuracy rate of DED-type prediction on the increase in applied number of image features. Image features were added to the queue with an order of [IF1, IF3, IF5, IF7, IF8, IF10, IF2, IF4, IF6, IF9, IF11]. (B) Different efficacies observed under the different sets of the five selected image features chosen by the rank in the ability of prediction (determined in Fig 2B). (C) Accuracy rates of DED-type prediction evaluated by our ML model using 11 image features. (D) Accuracy rates of DED-type prediction evaluated by orthodox ML model (bag of visual words) using 64 automatically determined image features.

DP values showed that Sat_{SD} (IF6) was the most significant image feature for type-predicting ability, while LCI_{RED} (IF8) was the least significant one. We found DED-type-specific trends in image feature values when using the five most significant image features determined by the DP values (IF6, IF7, IF2, IF5, and IF11 ranked under independent use, Fig. 2C). Normal type showed very low image feature values in almost all interference fringe images except IF2. ADDE type very clearly indicated very high values in all image features and EDE type showed moderate image feature values except for IF2, which showed very low values. In general, normal-type images tended to show clear fringe patterns with very lower color saturations; ADDE-type images showed complicated fringes containing many colors with higher saturations. In contrast, EDE-type images had a uniform and slightly colored surface with no fringes just after blinking. In many cases of ADDE and EDE patients, fringe images were accompanied by breakups of tear film. In the areas where tear film broke up, local roughness increased as a complicated texture (IF8 and IF9). These trends seemed to be the strong driving forces that would bring accurate type prediction by our ML models.

Next, we determined the minimum number of image features necessary to create accurate ML models (Fig. 3A). All three types (normal, ADDE, and EDE) showed an increase in accuracy rates depending on the number of image features added to the models; the accuracy rate curves were followed by plateaus at nine image features. In addition, predictions using all 11 image features showed higher accuracy rates than ones assessed by the most significant 5 image features (Fig. 3B). This indicated that 11 was the sufficient minimum necessary number of image features for this case.

Our ML model built using 11 image features showed effectively high F-scores (normal, 0.845 ± 0.067 ; ADDE, 0.981 ± 0.023 ; EDE, 0.815 ± 0.095) and high inter-rater agreement value (kappa coefficient = 0.820) with the predetermined DED-types

diagnosed by the skilled ophthalmologist, whereas the orthodox method using “bag of visual words” technique (we used 64 automatically determined image features by the algorithm to predict the types) showed very low F-scores (normal, 0.587 ± 0.146 ; ADDE, 0.669 ± 0.073 ; EDE, 0.549 ± 0.088) and agreement (kappa coefficient = 0.367). These results strongly indicate that the ML model built with a small but highly capable number of image features generated through minute investigation is able to bring effective diagnostic support, even though the image features have been created from non-structural image characteristics.

4. Conclusions and future perspectives

In this study, we originally developed a ML-based predictive model for DED diagnosis. In a previous study, it was reported that inter-rater agreement showed wide variation between observers in a range from 0.57 to 0.94.3 Even though we were not able to examine the same data set used in the report, our ML model demonstrated almost perfect inter-rater agreement with those diagnosed by the skilled ophthalmologist. The results indicate that our predictive model would help reduce diagnostic biases by providing observers with additional accurate diagnostic support, which is one of main purposes of this work. Nevertheless, accuracy rates for normal- and EDE-type predictions are lower than the accuracy rate for ADDE. We believe this is caused by the lower distinction between normal and EDE types, since they showed similar appearances in fringe colors. Our next step will be to further examine other image features that may enhance model performance in distinguishing between normal and EDE types, hence confirming the ability of this model through clinical evaluations using images collected from many more patients.

References

1. Craig JP, Nichols KK, Akpek EK, et al. TFOS DEWS II Definition and Classification Report. *Ocul Surf.* 2017;15: 276-283.
2. Arita R, Morishige N, Koh S, et al. Increased tear fluid production as a compensatory response to Meibomian gland loss: a multicenter cross-sectional study. *Ophthalmology.* 2015;122: 925-933.
3. Arita R, Morishige N, Fujii T, et al. Tear interferometric patterns reflect clinical tear dynamics in dry eye patients. *IOVS.* 2016;57: 3928-3934.
4. Liu YY, Chen M, Ishikawa H, Wollstein G, Schuman JS, Rehg JM. Automated macular pathology diagnosis in retinal OCT images using multi-scale spatial pyramid and local binary patterns in texture and shape encoding. *Med Image Anal.* 2011;15: 748-759.
5. Schmidt-Erfurth U, Klmscha S, Waldstein SM, Bogunović H. A view of the current and future role of optical coherence tomography in the management of age-related macular degeneration. *Eye.* 2017;31: 26-44.
6. Ataer-Cansizoglu E, Bolon-Canedo V, Campbell JP, et al. Computer-based image analysis for plus disease diagnosis in retinopathy of prematurity: performance of the “i-ROP” system and image features associated with expert. *TVST.* 2015;4: Article 5.

7. Jaya T, Dheeba J, Singh NA. Detection of hard exudates in colour fundus images using fuzzy support vector machine-based expert system. *J Digit Imaging*. 2015;28: 761-768.
8. Remeseiro B, Bolon-Canedo V, Peteiro-Barral D, et al. A methodology for improving tear film lipid layer classification. *IEEE J Biomed Health Inform*. 2014;18: 1485-1493.



Influence of benzalkonium chloride on tear film lipid layer stability: a molecular level view by employing *in silico* modeling

Kamila Riedlova¹, Adela Melcrova¹, Agnieszka Olzynska¹, Philippe Daull², Jean-Sebastien Garrigue², Lukasz Cwiklik¹

¹J. Heyrovsky Institute of Physical Chemistry, Czech Academy of Sciences, Prague, Czech Republic; ²Novagali Innovation Center, Santen SAS, Evry, France

Keywords: dry eye disease (DED), molecular dynamics, molecular simulations, tear film, tear film lipid layer

1. Background and purpose

Benzalkonium chloride (BAK) is a mixture of aliphatic C12 and C14 quaternary ammoniums. These molecules are traditionally used to preserve eye drops because of their bactericidal and bacteriostatic properties.^{1,2} The compounds of BAK have an amphiphilic character, hence it can be assumed that on the ocular surface they can interact and alter the properties of the tear film lipid layer (TFLL). Indeed, BAK was demonstrated to decrease the breakup time in patients, which is a hallmark of TFLL destabilization.³⁻⁶ The amphiphilic and water-soluble C12 and C14 BAK molecules are expected to act predominantly at the aqueous-lipid interface that, as we have demonstrated earlier, is populated mostly by polar lipids.^{7,8} Notably, these BAK species are short-chain analogues of cetalkonium chloride (CKC) that, as we have shown previously, interact with the TFLL model, improving its stability.⁹ We hypothesize that by influencing polar lipids, BAK (C12 and C14) can alter the details of molecular-level interactions between individual species of TFLL and indirectly influence the macroscopic behavior of the film, in particular its organization and stability.

Correspondence: Lukasz Cwiklik, J. Heyrovsky Institute of Physical Chemistry CAS, Dolejskova 2155/3, 18223 Prague, Czech Republic. E-mail: lukasz.cwiklik@jh-inst.cas.cz

2. Methods

In order to assess molecular-level properties of TFLL models, we employed *in silico* molecular dynamics (MD) simulations. This technique, widespread in biophysics, is unique in providing molecular-level information regarding the organization of molecular species, particularly at interfaces. In MD simulations, we considered lipid films at the water-air interface by employing coarse grain MARTINI model.¹⁰ This approach was proven to realistically model the biophysical properties of tear film (TF) and TFLL in our earlier studies.^{7,11,12} In the model, the lipid composition of TFLL was approximated by using main lipid classes found in human tears in lipidomics studies.¹³ More specifically, 1-palmitoyl-2-oleoyl-phosphatidylcholine (POPC); 1-palmitoyl-2-oleoyl-phosphatidylethanolamine (POPE); N-palmitoyl-d-erythro-sphingosine (PPCE); and N-palmitoyl-d-erythro-sphingosylphosphorylcholine (PPCS) were used as polar lipids employing the ratio found in the lipidome of human TF.¹³ Nonpolar lipid fraction was modeled by equimolar mixture of glycerine trioleate (TO) and cholesteryl oleate (CO). In order to address the issue of BAK interactions with deficient TFLL, here we used our previous TFLL *in silico* model⁷ with 20% of polar lipids removed. The polar lipids-deficient system was chosen in order to facilitate incorporation of BAK in the polar sublayer. Furthermore, such a system is a practical model of TFLL with decreased structural stability. Molecules of BAK,

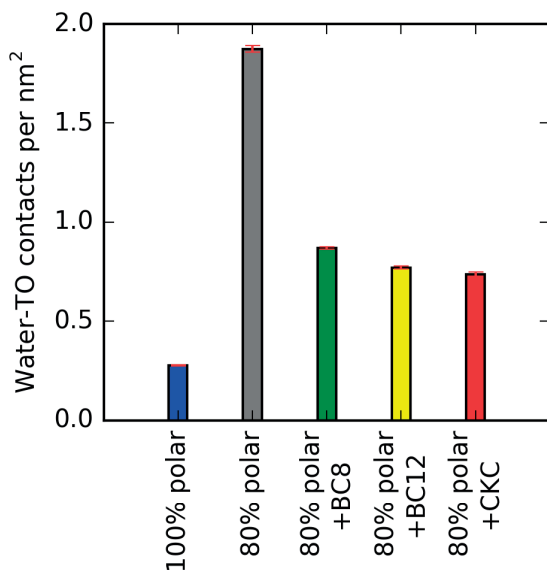


Fig. 1. Number of water-nonpolar lipid contacts (defined employing 08 nm cutoff) per interfacial unit area in the system with full polar sublayer and the systems with 20% reduction of polar lipids. Influence of BC8, BC12, and CKC on polar lipids-deficient TFLL model is shown.

namely, benzalkonium cations with either a C8 or C12 lipid chain (designated as BC8 and BC12) were added to the polar lipids-deficient TFL model. Additionally, we considered C16 BAK analog, *i.e.*, CKC. All three types of molecules were parameterized in-house using a standard MARTINI approach. In MARTINI representation, roughly four-to-one coarse graining is used for heavy atoms. Hence, for instance, POPC acyl chains containing 16 and 18 carbon atoms are represented, correspondingly, by 4 and 5 coarse grain beads that model hydrocarbon groups. Accordingly, the molecules of BC8, BC12, and CKC have two, three and four hydrocarbon beads in their nonpolar chain.

The simulation box typically consisted of 6000-25,000 lipids and 90,000-350,000 water beads. A lateral size of 34 x 34 nm² was considered, corresponding to a laterally relaxed TFL model.⁷ MD trajectories of ~2 μ s duration were simulated under equilibrium conditions. A lipid film completely covering the water surface was equilibrated at the water-air interface and its properties were analyzed.

3. Results

In our previous study, we identified a reduction of polar lipids in the TFL model as a major factor leading to lipid film destabilization.⁹ A reduced number of polar lipids results in enhanced water-nonpolar lipid contacts, the latter being an unfavorable factor reducing TFL stability. The number of these contacts in the TFL model (100% polar) as well as in the polar lipid-deficient system (80% polar) are shown for comparison in Figure 1. In the case of supplementation by BC8, BC12, and CKC, these unfavorable contacts are clearly reduced. The extent of this reduction can be ordered as BC8 < BC12 < CKC. It proves that all three considered surfactants interact with the TFL model. Moreover, it can be indirectly concluded that their presence would enhance model stability.

The details of molecular-level interaction between the system components can be analyzed using density profiles, as shown in Figure 2. In the case of all three considered surfactants, the supplemented molecules are localized in the polar sublayer of the considered TFL model. Their polar headgroups (red dashed lines) are located somehow closer to the nonpolar layer than the headgroups of phospholipids, while their tail terminals (red solid lines) penetrate into the nonpolar layer. A separation between the headgroup-tail terminal increases in a row BC8 < BC12 < CKC. Overall, all three surfactants accommodate into the polar sublayer, in between other polar lipids, somewhat sealing the interface and hence, reducing water-nonpolar lipids contacts as discussed beforehand.

Further insight into localization of BAK and CKC in the polar layer can be obtained from an analysis of their orientation with respect to other lipids. In Figure 3, the tilt angles of BC8, BC12, and CKC are compared with those of sn-2 (oleoyl) chains of POPC phospholipids in the corresponding systems as well as in the TFL system

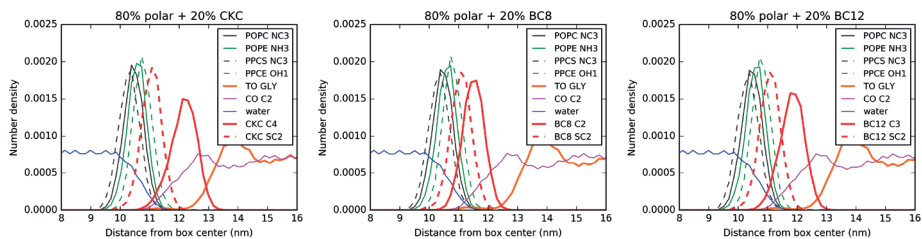


Fig. 2. Density profiles (number of molecules as a function of a distance from the simulation box center) of selected atoms/groups of the molecules present at the water air interface. The profiles of the polar headgroups of the considered phospholipids (POPC NC3, POPE NH3, PPCS NC3, PPCE OH1) are shown together with the glycerol backbone of TO molecule (TO GLY), C2 carbon of CO, and water. Profiles of polar headgroup (SC2) and nonpolar chain terminals of the supplementing surfactants (BC8 C2, BC12 C3, and CKC C4) are also depicted.

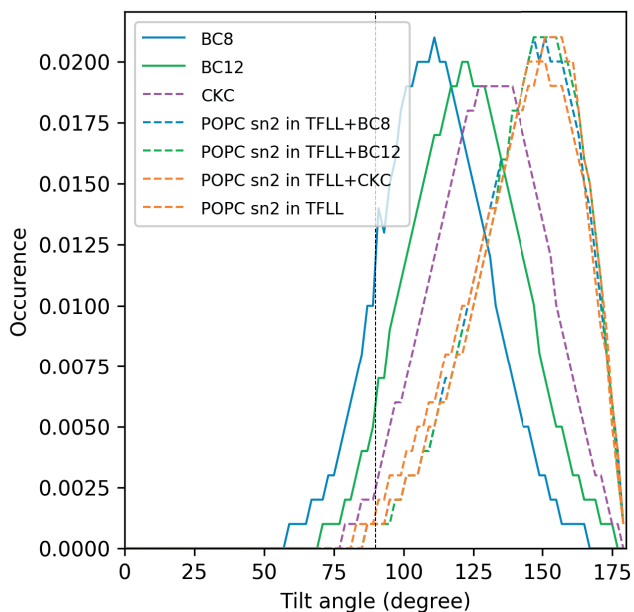


Fig. 3. Tilt angle distributions of selected chains. The tilt angle is defined as the angle between the vector formed between the initial and terminal carbon atom of a chain and the interface normal. The angle of 180° corresponds to a chain oriented perpendicular to the water-air interface and directed toward the nonpolar lipids phase. The angle of 90° (marked in the plot with dashed line) corresponds to a chain parallel to the interface. The angle of 0° describes a chain oriented perpendicular to the interface and directed toward the water phase.

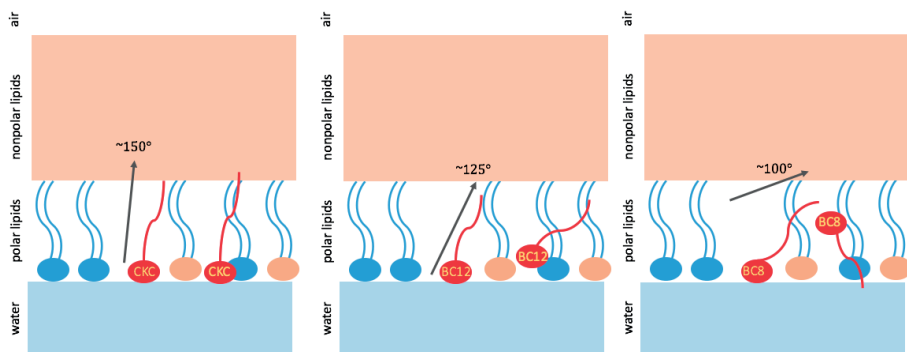


Fig. 4. A cartoon representation of tilt angles and orientation of CKC, BC12, and BC8 molecules in the TFL model. Estimates of the most populated tilt angle values from Figure 3 are given.

without polar lipids deficiency. First, the sn-2 chains in all considered cases attain orientations parallel to the water-air interface, pointing toward the nonpolar lipids phase. Such an orientation was observed also in our previous studies of relaxed TFL models.^{7,14} Second, all three surfactants have reduced values of tilt angles with respect to sn-2 of POPC. This effect is weak in the case of CKC, more pronounced in BC12, and the most significant in BC8. It demonstrates that the hydrophobic chains of the added surfactants do not fully match orientation of their phospholipid counterparts in the polar sublayer of TFL model. Notably, the chains of BC8 and BC12 have non-negligible angle populations below 90° C, which means that the nonpolar tails of these molecules reorient toward the water phases.

In Figure 4, a schematic representation of the calculated tilt angles and orientation of the surfactants is shown. This representation also corresponds to typical snapshots observed during MD simulations (not shown). It can be seen that orientation of CKC molecules is close to that of other polar lipids, while in the case of BC12 and BC8 it is less ordered. In particular, BC8 is able to significantly reorient while being in the polar sublayer, forming defects in the polar lipids structure.

4. Conclusions and future perspectives

According to MD simulations, all three considered surfactants, BC8, BC12, and CKC, incorporate into the polar sublayer of the TFL model. As they populate the water-lipid interface, they reduce water-nonpolar lipids contacts. The details of their orientation in the lipid film differ. CKC, which is the longest from the considered surfactants molecules, behaves similarly to the phospholipids that form the polar sublayer; it is predominantly located parallel to the phospholipid acyl chains, with its headgroup pointing toward the aqueous subphase. On the other hand, both BC8 and BC12 attain a more flexible orientation, with their hydrophobic chains being

able to reorient. This reorientation is particularly significant for the shortest BC8 with its tail often pointing toward the aqueous subphase. Overall, the obtained molecular-level picture allows to conclude that CKC stabilizes the TFL (as seen in patients and *in vitro*),¹⁵⁻¹⁷ while the shorter BAK molecules may have a destabilizing effect, similar to that observed experimentally.^{3,18,19}

Acknowledgements

This work was supported by grant 18-26751S from the Czech Science Foundation. Adela Melcrova was supported by grant SVV 2017 No. 260 443 and by the Martina Roeselová foundation. Agnieszka Olzynska and Lukasz Cwiklik are in commercial relationship with Santen SAS.

References

1. Kurup TR, Wan L, Chan L. Preservative requirements in emulsions. *Pharm Acta Helv.* 1992;67(7):204-208.
2. Campanac C, Pineau L, Payard A, Baziard-Mouysset G, Roques C. Interactions between biocide cationic agents and bacterial biofilms. *Antimicrob Agents Chemother.* 2002;46(5):1469-1474. doi: 10.1128/AAC.46.5.1469-1474.2002.
3. Baudouin C, Labbé A, Liang H, Pauly A, Brignole-Baudouin F. Preservatives in eyedrops: the good, the bad and the ugly. *Prog Retin Eye Res.* 2010;29(4):312-334. doi: 10.1016/j.preteyeres.2010.03.001.
4. Wilson W, Duncan A, Jay J. Effect of benzalkonium chloride on the stability of the precorneal tear film in rabbit and man. *Br J Ophthalmol.* 1975;59(11):667-669. doi: 10.1136/bjo.59.11.667.
5. Campagna P, Macri A, Rolando M, Calabria G. Chronic topical eye preservative free beta blocker therapy effect on the ocular surface in glaucomatous patients. *Acta Ophthalmol Scand Suppl.* 1997;75(S224):53. doi: 10.1111/j.1600-0420.1997.tb00480.x
6. Herreras JM, Pastor JC, Calonge M, Asensio VM. Ocular surface alteration after long-term treatment with an antiglaucomatous drug. *Ophthalmology.* 1992;99(7):1082-1088. doi: 10.1016/S0161-6420(92)31847-0.
7. Wizert A, Iskander DR, Cwiklik L. Organization of lipids in the tear film: a molecular-level view. *PLoS One.* 2014;9(3). doi: 10.1371/journal.pone.0092461. PubMed PMID: WOS:000333352800111.
8. Cwiklik L. Tear film lipid layer: A molecular level view. *Biochim Biophys Acta.* 2016;(10):2421-2430. doi: 10.1016/j.bbamem.2016.02.020.
9. Nencheva Y, Olzynska A, Melcrova A, et al. Improving stability of tear film lipid layer via concerted action of two drug molecules: a biophysical view. *Biophys J.* 2018;114(3):104a. doi: 10.1016/j.bpj.2017.11.609.
10. Marrink SJ, Risselada HJ, Yefimov S, Tieleman DP, de Vries AH. The MARTINI force field: coarse grained model for biomolecular simulations. *J Phys Chem B.* 2007;111(27):7812-7824. doi: 10.1021/jp071097f. PubMed PMID: 17569554.
11. Olżyńska A, Cwiklik L. Behavior of sphingomyelin and ceramide in a tear film lipid layer model. *Ann Anat.* 2017;210:128-134. doi: 10.1016/j.aanat.2016.10.005.
12. Wizert A, Iskander DR, Cwiklik L. Interaction of lysozyme with a tear film lipid layer model: A molecular dynamics simulation study. *Biochim Biophys Acta.* 2017;1859(12):2289-2296. doi: 10.1016/j.bbamem.2017.08.015. PubMed PMID: WOS:000415770900002.

13. Rantamaki AH, Seppanen-Laakso T, Oresic M, Jauhiainen M, Holopainen JM. Human tear fluid lipidome: from composition to function. *PLoS One*. 2011;6(5):e19553. doi: 10.1371/journal.pone.0019553. PubMed PMID: 21573170; PubMed Central PMCID: PMC3088682.
14. Olzyska A, Cwiklik L. Behavior of sphingomyelin and ceramide in a tear film lipid layer model. *Anat Anat*. 2017;210:128-134. doi: 10.1016/j.aanat.2016.10.005. PubMed PMID: WOS:000395610600016.
15. Robert P-Y, Cochener B, Amrane M, et al. Efficacy and safety of a cationic emulsion in the treatment of moderate to severe dry eye disease: a randomized controlled study. *Eur J Ophthalmol*. 2016;26(6):546-555. doi: 10.5301/ejo.5000830.
16. Georgiev GA, Yokoi N, Nencheva Y, Peev N, Daull P. Surface chemistry interactions of cationorm with films by human meibum and tear film compounds. *Int J Mol Sci*. 2017;18(7):1558. doi: 10.3390/ijms18071558.
17. Amrane M, Creuzot-Garcher C, Robert P-Y, et al. Ocular tolerability and efficacy of a cationic emulsion in patients with mild to moderate dry eye disease–A randomised comparative study. *J Fr Ophthalmol*. 2014;37(8):589-598. doi: 10.1016/j.jfo.2014.05.001.
18. Baudouin C, de Lunardo C. Short term comparative study of topical 2% carteolol with and without benzalkonium chloride in healthy volunteers. *Br J Ophthalmol*. 1998;82(1):39-42. doi: 10.1136/bjo.82.1.39.
19. Ishibashi T, Yokoi N, Kinoshita S. Comparison of the short-term effects on the human corneal surface of topical timolol maleate with and without benzalkonium chloride. *J Glaucoma*. 2003;12(6):486-90.



Image processing-based model for tortuosity measurement of retinal blood vessels

Sanyukta Chetia, S.R. Nirmala

Department of Electronics and Communication Engineering, Gauhati University, Guwahati, Assam, India

Abstract

Purpose: The study of retinal blood vessel morphology is of great importance in retinal image analysis. The retinal blood vessels have a number of distinct features such as width, diameter, tortuosity, etc. In this paper, a method is proposed to measure the tortuosity of retinal blood vessels obtained from retinal fundus images. Tortuosity is a situation in which blood vessels become tortuous, that is, curved or non-smooth. It is one of the earliest changes that occur in blood vessels in some retinal diseases. Hence, its detection at an early stage can prevent the progression of retinal diseases such as diabetic retinopathy, hypertensive retinopathy, retinopathy of prematurity, etc. The present study focuses on the measurement of retinal blood vessel tortuosity for the analysis of hypertensive retinopathy. Hypertensive retinopathy is a condition in which the retinal vessels undergo changes and become tortuous due to long term high blood pressure. Early recognition of hypertensive retinopathy signs remains an important step in determining the target-organ damage and risk assessment of hypertensive patients. Hence, this paper attempts to estimate tortuosity using image-processing techniques that have been tested on artery and vein segments of retinal images.

Design: Image processing-based model designed to measure blood vessel tortuosity.

Methods: In this paper, a novel image processing-based model is proposed for tortuosity measurement. This parameter will be helpful for analyzing hypertensive retinopathy. To test the effectiveness of the system in determining tortuosity, the method is first applied on a set of synthetically generated blood vessels. Then, the method is repeated on blood vessel (both artery and vein) segments extracted

Correspondence: S.R. Nirmala, Department of Electronics and Communication Engineering, Gauhati University, Assam, India. E-mail: nirmalr3@gmail.com

from retinal images collected from publicly available databases and on images collected from a local eye hospital. The blood vessel segment images that are used in the method are binary images where blood vessels are represented by white pixels (foreground), while black pixels represent the background. Vessels are then classified into normal, moderately tortuous, and severely tortuous by following the analysis performed on the images in the Retinal Vessel Tortuosity Data Set (RET-TORT) obtained from BioIm Lab, Laboratory of Biomedical Imaging (Padova, Italy). This database consists of 30 artery segments and 30 vein segments, which were manually ordered on the basis of increasing tortuosity by Dr. S. Piermarocchi, a retinal specialist belonging to the Department of Ophthalmology of the University of Padova (Italy). The artery and vein segments with the fewest number of turns are given a low tortuosity ranking, while those with the greatest number of turns are given a high tortuosity ranking by the expert. Based on this concept, our proposed method defines retinal image segments as normal when they present the fewest number of twists/turns, moderately tortuous when they present more twists/turns than normal but fewer than severely tortuous vessels, and severely tortuous when they present a greater number of twists/turns than moderately tortuous vessels. On implementing our image processing-based method on binary blood vessel segment images that are represented by white pixels, it is found that the vessel pixel (white pixels) count increases with increasing vessel tortuosity. That is, for normal blood vessels, the white pixel count is less compared to moderately tortuous and severely tortuous vessels. It should be noted that the images obtained from the different databases and from the local hospital for this experiment are not hypertensive retinopathy images. Instead, they are mostly normal eye images and very few of them show tortuous blood vessels.

Results: The results of the synthetically generated vessel segment images from the baseline for the evaluation of retinal blood vessel tortuosity. The proposed method is then applied on the retinal vessel segments that are obtained from the DRIVE and HRF databases, respectively. Finally, to evaluate the capability of the proposed method in determining the tortuosity level of the blood vessels, the method is tested with a standard tortuous database, namely, the RET-TORT database. The results are then compared with the tortuosity level mentioned in the database. It was found that our method is able to classify blood vessel images as normal, moderately tortuous, and severely tortuous, with results closely matching the clinical ordering provided by the expert in the RET-TORT database. Subjective evaluation was also performed by research scholars and postgraduate students to cross-validate the results.

Conclusion: The close correlation between the tortuosity evaluation using the proposed method and the clinical ordering of retinal vessels as provided by the retinal specialist in the RET-TORT database shows that, although simple, this method can evaluate the tortuosity of vessel segments effectively.

Keywords: blood vessel pixels, hypertensive retinopathy, retinal blood vessels, tortuosity

1. Introduction

The retina, which forms the third and inner coating of the eye, contains arteries and veins. These retinal blood vessels can be easily imaged non-invasively using a fundus camera.¹ Retinal vessels have a number of observable features such as width, diameter, tortuosity, etc. These blood vessels are part of the circulatory system that supplies oxygen and nutrients throughout the body. The arteries carry oxygenated blood away from the heart to the body, while veins carry deoxygenated blood from the body to the heart. Thus, the retinal arteries supply oxygenated blood to the retina, while the retinal veins carry away oxygen-poor blood from the retina. Hence, proper functioning of arteries and veins is essential for a healthy retina; changes in retinal vessel features can lead to an unhealthy retina. The pathophysiological changes of these features may be associated with retinopathies or cardiovascular disease.²

The term retinopathy refers to damage to the retina. Hypertensive retinopathy is a condition in which the retinal vessels undergo changes due to high blood pressure.³ The various vascular signs that arise from elevated blood pressure include arteriolar narrowing, arteriovenous nicking, cotton-wool spots, hard exudates, and optic disc swelling.⁴ Individuals with elevated blood pressure often develop an abnormal curvature along the vessel length, which is referred to as tortuosity.⁵ Generally, in individuals with normal blood pressure (120/80 mmHg), blood vessels have smooth inner walls and blood flows through them without any trouble. However, when this pressure rises, *i.e.*, in cases of hypertension (140/90 mmHg or higher over a number of weeks), blood flows through the vessels with a large force, damaging blood vessel walls in such a way that they become thick and non-smooth. This, in turn, causes blood vessels to take on twisted paths, giving rise to tortuosity. Hence, in cases of acute hypertension, there is an increase in vascular tortuosity.⁶ Figures 1a and 1b show a retinal image with normal blood vessels and tortuous blood vessels, respectively. The normal blood vessels are smooth, whereas the tortuous blood vessels are not smooth in appearance. Thus, a blood vessel is said to be tortuous when it presents several twists and turns instead of being straight or gently curved.⁷

Hypertension leads to a number of complications. Hypertensive retinopathy is considered to be one such major complication. A person with hypertensive retinopathy may also develop other complications of hypertension, such as cardiovascular risk and nephropathy.⁸ Hypertensive retinopathy is also associated with congestive heart failure, cerebrovascular disease, and stroke mortality.⁴ A study showed that hypertensive retinopathy is linked to coronary heart disease.⁹ In a population-based study among individuals with hypertension, hyperten-

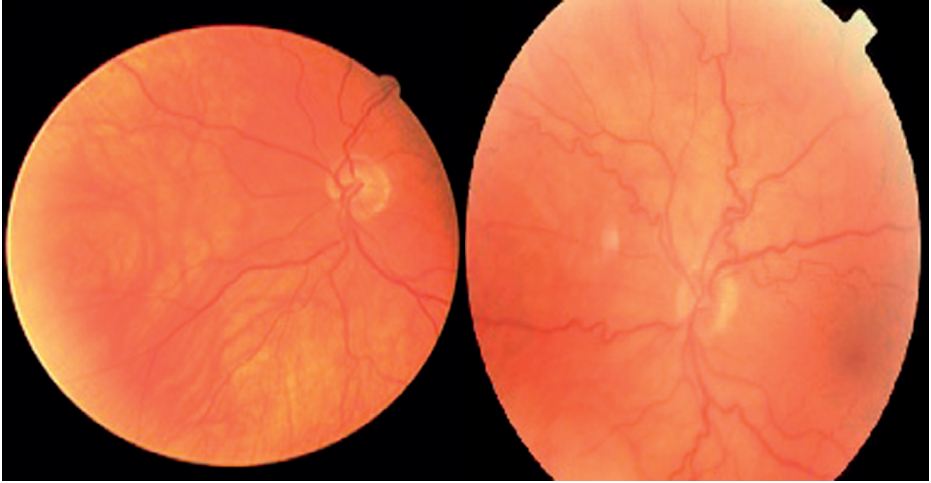


Fig. 1. Retinal fundus images with (a) normal blood vessels and (b) tortuous blood vessels.

sive retinopathy was related to an elevated risk of stroke. Thus, for hypertensive individuals, retinal examination can provide necessary information to determine the risk of stroke.¹⁰ Retinal examination of hypertensive patients shows that vessel tortuosity increases in case of long-term acute hypertension. Hence, in this work, we present a method based on image processing techniques for measuring retinal blood vessel tortuosity. The proposed method considers both retinal arteries and veins for the purpose of evaluating tortuosity.

2. Literature review

Different methods have been proposed to assess retinal vessel tortuosity. Sharbaf *et al.* proposed a curvature-based algorithm for automatic grading of retinal vessel tortuosity.¹¹ The algorithm was applied to evaluate tortuosity in single vessels as well as in a vessel network. To measure tortuosity, the authors used the concept of curvature, which is a mathematical measure for how inflected a curve is at a certain coordinate. The method used for calculating curvature is the template disc method. The basic principle of curvature calculation using this method is to relate the area between the curve and a template disc of a suitable radius of curvature, as shown in Figure 2. To calculate curvature at a point $p(x,y)$, initially a template disc of radius b is drawn around the point. Then the center of the Cartesian coordinate system is set on the point. In the figure, $f(x)$ is a planar curve representing the blood vessel, A is the area between the curve and the template disc of radius b , θ_c is the cross-over angle between the template disc and the cross-over point (κ_{cp}) with respect to the x-axis. The authors have defined the curvature as $k = 1/A^2$. Thus, for a large area,

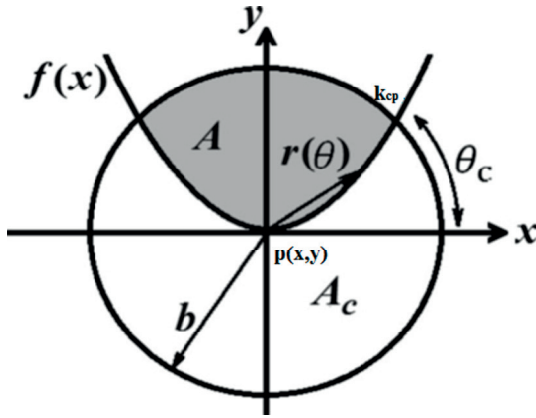


Fig. 2. Curvature calculation using the template disc method.

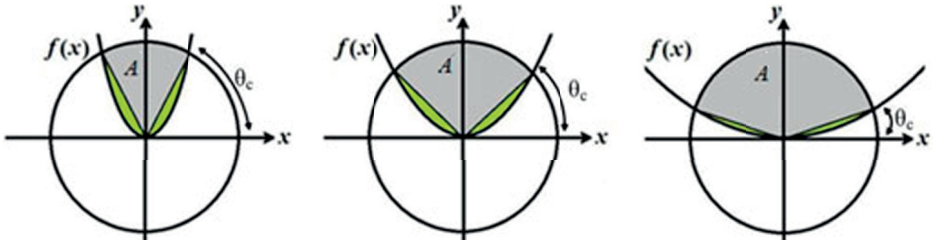


Fig. 3. Approximating area A using the cross-over point of the curve and the template disc.

the curvature is small and vice versa, as shown in Figure 3. After calculating the curvature using the above equation for a single vessel, tortuosity is evaluated for the vessel network. The authors segmented the blood vessels, generated the vascular skeleton map, and evaluated the tortuosity using the formula:

$$\tau = \frac{1}{m} \sum_{i=1}^m k_i \quad (1)$$

where k_i denotes curvature for the i^{th} point on the vessel map and m denotes the total number of points for which curvature is measured. The authors used three databases to find the correlation between their algorithm and the results obtained for these databases. For evaluating tortuosity in a single vessel, the authors used the RET-TORT dataset obtained from Biolm Lab, Laboratory of Biomedical Imaging.¹² This database was introduced by Grisan *et al.*¹³ and comprises 30 artery segments and 30 vein segments from normal and hypertensive patients, arranged in order of increasing tortuosity by an expert. In this case, the correlation between the ranking obtained by the algorithm developed by the authors and the expert's ranking is 0.94. The second dataset was provided by Khatam-Al-Anbia Hospital, Mashhad

(Iran), consisting of ten full retinal images diagnosed with diabetic retinopathy and used for measuring vessel network tortuosity. Based on tortuosity, the images in this dataset are arranged by many experienced experts. Here, the correlation between the method introduced by the authors and the subjective results is 0.95. The third database comprised a private databank containing 120 full retinal images diagnosed with retinopathy of prematurity (ROP), which was also used to measure vessel network tortuosity. The authors evaluated the performance of their algorithm and obtained a correlation of 0.7 in this case.

Cavallari *et al.*¹⁴ proposed a semi-automated, computer-based method for automatic analysis of retinal images in hypertensive retinopathy. The authors defined the tortuosity index as a measure of blood vessel tortuosity. They considered 16 subjects with hypertensive retinopathy and funduscopy was carried out using a digital fundus camera. Using a software called Cioran, the authors calculated the tortuosity index following three steps:

1. vessel extraction;
2. vessel tracking; and
3. measurement of tortuosity index.

The vessel path is automatically extracted by the process of iterative runs of the subtract background task. On selecting the starting and end points of the vessel segment by the operator, Cioran automatically tracks the vessel. Lastly, for the measurement of tortuosity index, the Bezier and Spline interpolation method is used. Thus, the vessel path is described by a regular analytical function $y = f(x)$. The operator selected start and end points were set to $y = 0$. The computation of tortuosity index takes into consideration:

1. the area under the curve described by the segment of the vessel; and
2. the number of times directional changes occur along the vessel path.

The directional changes correspond to the points where the first derivative of the analytic function is equal to zero and the vessel path changes its slope.

Turior *et al.*¹⁵ have proposed curvature-based tortuosity metrics in the retinal blood vessels of premature infants. Tortuosity is evaluated by estimating the curvature of each point over some region and then adding the curvature at every pixels of the vessel. The curvature at each point is calculated by proper pairing of chain codes and related chain code rules. The chain code representation is based on certain geometric concepts that are related with the straightness or non-straightness of a digital curve. Figure 4 depicts a segment of a digital curve showing pair of chain codes for $k = 8$. The discrete curvature around the concerned point p_i is obtained by using the expression:

$$k(p_i, k) = \frac{1}{k} \sum_{j=1}^k \min \left\{ \min(f'_{i+j}, 8 - f'_{i+j}), \min(f'^{(+1)}_{i+j}, 8 - f'^{(+1)}_{i+j}), \min(f'^{(-1)}_{i+j}, 8 - f'^{(-1)}_{i+j}) \right\},$$

where

$$f'_{i+j} = |f_{i+j} - f_{i-j+1}|,$$

$$f'^{(+1)}_{i+j} = |f_{i+j+1} - f_{i-j+1}|,$$

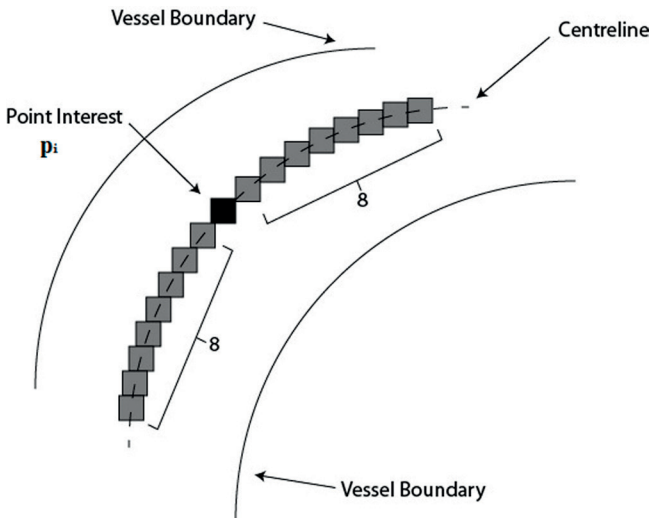
$$f_{i+j}^{(-1)} = |f_{i+j} - f_{i-j}| \tag{2}$$

where f_{i+j} and f_{i-j} are the chain code of the j^{th} leading and following point with respect to the point of interest p_i , respectively, is an integer given by $f = 0, 1, 2, \dots$, and k is the number of points used for calculating curvature. After calculating the curvature, the authors estimated the tortuosity of blood vessel as:

$$\tau = \left(\frac{n_{ic} - 1}{n_{ic}} \right) \frac{1}{L} \sum_{i=1}^n k(p_i, k) \tag{3}$$

n_{ic} and L are the number of inflection points and arc length, respectively, and n is the number of pixels in the vessel segment considered. The authors used the Naive Bayes neural classifier to classify non-tortuous, semi-tortuous, or extreme tortuous vessels on 45 retinal images. The retinal images were obtained from the Digital Imaging Research Centre of Kingston University (London, UK), Department of Ophthalmology of the Imperial College (London, UK) and Thammasat Hospital (Thailand). Following this, the authors achieved the best sensitivity and classification rate of 97.8% and 93.6% for non-tortuous, semi-tortuous, and extreme tortuous vessel segments, respectively.

El Abbadi and Al Saadi¹⁶ proposed a method for automatic human retinal vessel tortuosity measurement. The authors used a mask filter to trace the vessel along its course; tortuosity was then evaluated using the arc-to-chord ratio. A 3×3 mask (Fig. 5) is created and used to calculate vessel segment tortuosity. The center of the mask is placed over the first pixel of the blood vessel segment. The mask is then moved along the complete length of the vessel segment to determine its length.



-7	-2	-4
0	0	1
7	2	4

Fig. 5. A 3×3 mask used for evaluating tortuosity.

Fig. 4. A segment of a digital curve showing pair of chain codes for $k = 8$.

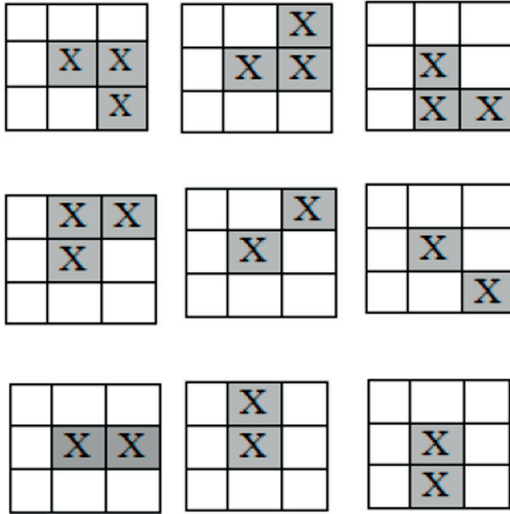


Fig. 6. Probable orientation of the blood vessel from the mask.

The movement of the mask from left to right also provides its orientation. There are nine possible orientations of the blood vessel segment pixels according to the filter. Figure 6 shows the orientation of the blood vessel segment using the 3×3 mask. In Figure 6, the blood vessel segment pixels are represented in gray, whereas white represents the background.

Then, using the Euclidean distance, the straight distance between the first and last points of the vessel is calculated as:

$$D_{\text{straight}} = \sqrt{(x_N - x_1)^2 + (y_N - y_1)^2} \quad (4)$$

where, (x_1, y_1) are the coordinates of the first point and (x_N, y_N) are the coordinates of the end point of the vessel segment, respectively.

The arc length L_{arc} when the mask reaches the last pixel in the blood vessel segment is obtained by adding the distance between consecutive points in the vessel. Mathematically:

$$L_{\text{arc}} = \sqrt{(x_{i+1} - x_i)^2 + (y_N - y_i)^2} \quad (5)$$

where (x_i, y_i) are the coordinates of the i^{th} pixel in the vessel segment consisting of N constituent points.

Finally, tortuosity is calculated using the formula:

$$\text{Tortuosity} = \frac{L_{\text{arc}}}{D_{\text{straight}}} \quad (6)$$

After a detailed survey of the available literature, we found that several authors have proposed different methods for evaluating tortuosity. However, there is ample room for contributions on evaluating tortuosity in hypertensive retinopathy images. Early detection of this disease is crucial to avoid its related risks. The current trend for tortuosity evaluation is based on manual examination of fundus photographs by human experts. Thus, there is a need to develop a method that could assist experts in determining tortuosity automatically, which is the purpose of the present work. This paper presents an image processing-based method for evaluating retinal blood vessel tortuosity automatically.

3. Methods

A block diagram of our proposed method is shown in Figure 7.



Fig. 7. Block diagram of the proposed model for tortuosity evaluation.

3.1. Input retinal images

A total of 55 retinal images are considered in the present work. Of these 55 images, 20 images were collected from the publicly available DRIVE database,¹⁷ 30 images were collected from the publicly available High-Resolution Fundus (HRF) database,¹⁸ and 5 images were collected from a local eye hospital, the Chandraprabha Eye Hospital (Jorhat, Assam, India). Figure 8a shows a retinal image, obtained from the DRIVE database, used as input in the proposed method.

3.2. Pre-processing

After acquiring the retinal image, the first stage is pre-processing the image. The main function of this step is to obtain uniform illumination in all retinal images. After the pre-processing stage, the images are more suitable for use in the later stages. Pre-processing consists of three main steps: green channel extraction, image complement and histogram equalization.

1. Green channel extraction: The input retinal images from the different databases and from the local hospital are all color images. The color images consist of three main color bands: red (R), green (G), and blue (B), known as RGB images. However, the green band is extracted from this RGB image as it provides a good contrast between the blood vessels and the background (Fig. 8b).
2. Image complement: The green band image is turned into a negative image

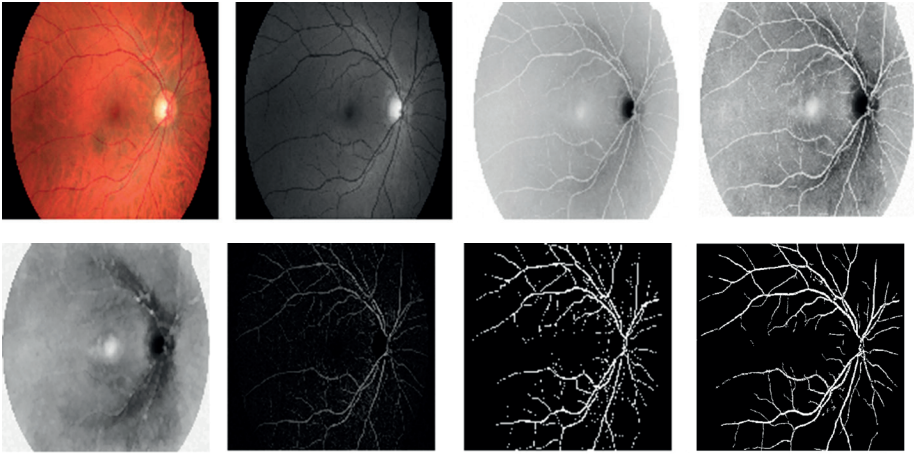


Fig. 8. Results of pre-processing and segmentation: (a) original image, (b) green channel image, (c) complement image, (d) CLAHE image, (e) opened image, (f) disc removed image, and (g) detected blood vessels (h) after removing small non-vessel regions.

in order to make the light areas become darker and vice versa for further processing (Fig. 8c).

3. Histogram equalization: An image enhancement technique known as Contrast Limited Adaptive Histogram Equalization (CLAHE) is used to enhance image contrast. The image is divided into a number of small, non-overlapping regions called tiles and the local contrast of all the regions is enhanced.¹⁹ The contrast enhanced image is shown in Figure 8d.

3.3. Segmentation

The next step after pre-processing is the segmentation of the histogram equalized retinal image. The main function of this step is to extract the blood vessels given that they are the focus of the proposed method. It consists of two main steps: morphological opening and image binarization.

1. Morphological opening: Erosion and dilation are the two basic morphological operations.²⁰ When pixels are added to the object boundaries, the object expands; this process is known as dilation. When pixels are removed from the object boundaries, it is known as erosion, which leads to shrinkage of objects. Here, a disc-shaped structuring element of radius 19 is used to remove objects, such as the optic disc, from the retinal image. For this, erosion is performed first, followed by dilation operation. Figure 8e depicts the result of the opening operation. A disc-removed image is then obtained by subtracting the opened image from the CLAHE image (Fig. 8f).
2. Image binarization: Image binarization is the process of creating a binary image with only two sets of pixel values: white as foreground and black as

background, or vice versa, as per the requirement. A binary image can be obtained by the thresholding process. Global thresholding and local thresholding are the two classes of thresholding.²¹ In this work, global thresholding by Otsu's method is used and applied on the disc-removed image to segment blood vessels. Figure 8g represents the binary image, consisting of blood vessels as the foreground white pixels. In addition to the blood vessels, a few small regions that are not part of the blood vessel pixels can be observed in this image. However, these small regions can be removed from the binary image by using morphological operations which open (push) the small isolated regions into the background (Fig. 8h). The effect of segmentation quality is therefore essential for achieving good segmentation results. There are many blood vessel segmentation techniques available in the previous works. We have used a simple threshold-based method that satisfies our requirements.

3.4. Tortuosity measurement by counting the occurrence of vessel pixels

To measure the tortuosity of a blood vessel, let us consider a binary image where blood vessels are represented by white pixels and the background by black pixels (Fig. 8h). From this binary image, some vessel segment regions are manually selected and cropped (Fig. 9a). This region is represented as a blood vessel segment image (Fig. 9b). This vessel segment image is then scanned from left to right, and the number of blood vessel pixels (white pixels) found in each scan is counted. This is repeated until scanning covers the entire vessel segment image. It is observed that, as vessel tortuosity increases, this process gives different results with increased number of vessel pixels.

To emphasize the effect of this observation, synthetically generated vessel segment images of size 100×500 were initially considered (Fig. 10). The vessel segments were classified into three types: normal, moderately tortuous, and severely tortuous. In our experiments, a normal vessel is considered to have fewer turns/twists compared to moderately tortuous and severely tortuous vessels. This observation is obtained from the literature and from the RET-TORT dataset.¹²

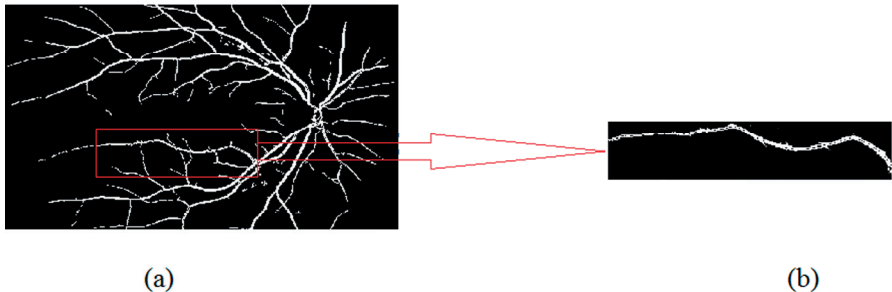


Fig. 9. (a) Blood vessel image. (b) Blood vessel segment image.

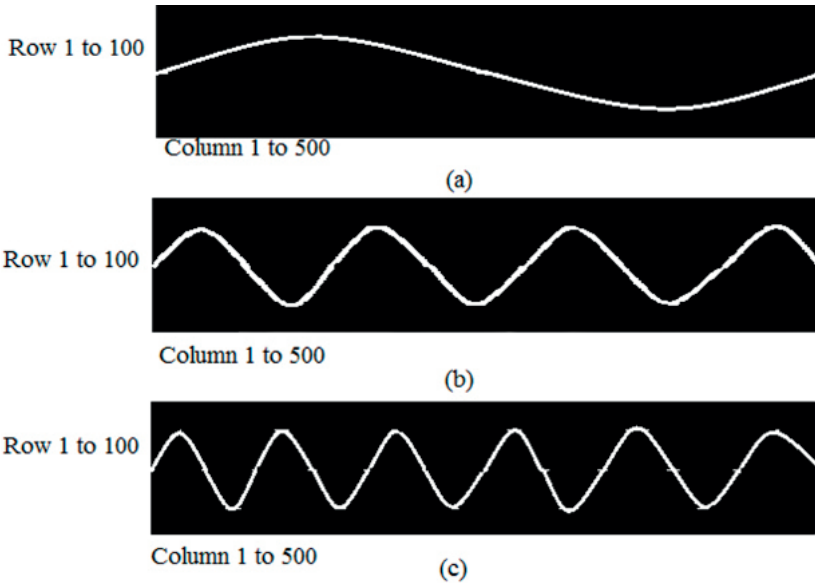


Fig. 10. Synthetically generated (a) normal, (b) moderately tortuous, and (c) severely tortuous vessel segment images.

The retinal vessel segment images in the RET-TORT database are arranged by a retinal specialist on the basis of increasing tortuosity by considering the number of turns/twists of the vessels. The vessels with fewer number of turns are given a low tortuosity ranking, whereas those with a greater number of turns are given a high tortuosity ranking. Thus, in our experiment we have also considered the number of turns/twists to classify the vessel segments as normal, moderately tortuous, or severely tortuous vessels.

For the synthetically generated vessels, the frequency of oscillations of the sine waves defines whether vessels are normal, moderately tortuous, or severely tortuous, given that the frequency of oscillations is related to the number of turns/twists. Sine waves with a lower oscillation frequency are considered to have fewer number of turns or be gently curved; they are classified as normal vessels. Similarly, sine waves with a higher oscillation frequency are considered to have a greater number of turns; they are classified as moderately tortuous vessels. Vessels with a greater oscillation frequency than moderately tortuous vessels are classified as severely tortuous. Figure 10a-c shows increasing oscillation frequencies for normal, moderately tortuous, and severely tortuous vessel segments. Thus, the frequency of oscillation is considered as a parameter for classifying these vessel segments as normal, moderately tortuous, or severely tortuous. In our method, this is referred to as tortuosity of synthetically generated vessels. It should be noted that in all types of synthetically generated vessels, the amplitude of the sinusoids is the same

while the oscillation frequency varies. Hence, we are considering that a synthetically generated normal vessel segment consists of a lower number of oscillations compared to moderately tortuous and severely tortuous vessel segments. The histograms showing the vessel pixel (white pixels) count for the corresponding synthetically generated blood vessels segments are shown in Figure 11a-c.

It can be observed from the graph in Figure 11a that the maximum occurrence of blood vessel pixels in a given row is five and that there are only two rows containing the maximum number of vessel pixels. The plot shows nearly a flat histogram, except for a few rows containing the maximum count. The histogram plot for a moderately tortuous vessel segment is shown in Figure 11b. In this case, the maximum occurrence of blood vessel pixels in a given row increases to 16 and the number of rows containing the maximum number of vessel pixels increases to 18. The plot consists of more than one flat region. Figure 11c depicts a severely tortuous vessel segment, where the maximum occurrence of blood vessel pixels further increases to 24 and the number of rows having the maximum number of vessel pixels is 20. In a similar fashion to the moderate case, the histogram consists of more than one flat region. The experiment is then repeated considering synthetically generated vessel segments of three different orientations: horizontal,

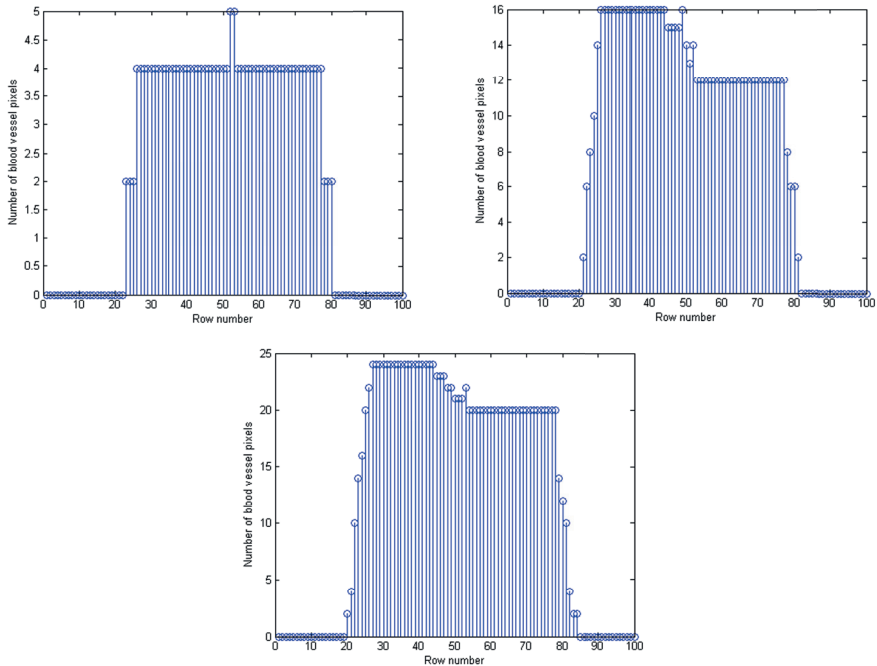


Fig. 11. Histogram of synthetically generated (a) normal, (b) moderately tortuous, and (c) severely tortuous vessel segments.

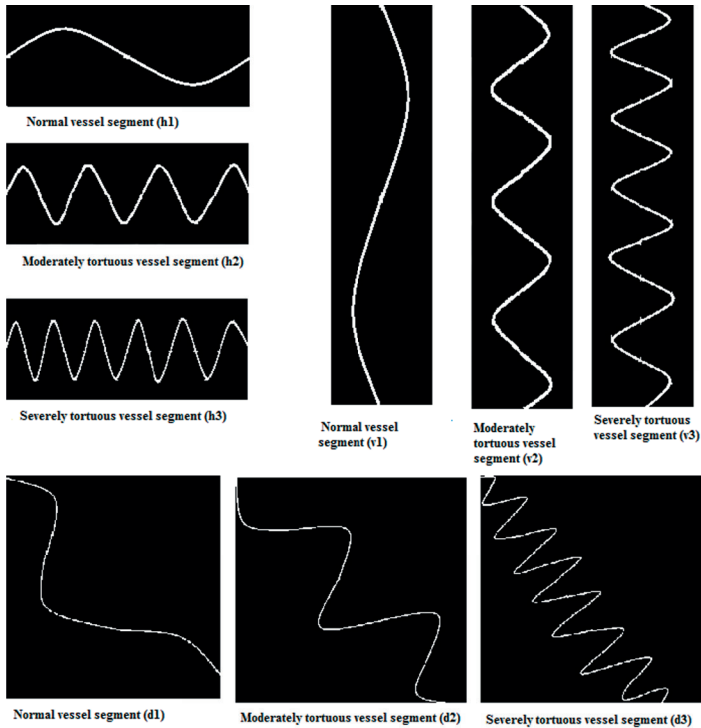


Fig. 12. Synthetically generated blood vessel segments in different orientations .

vertical, and diagonal, as depicted in Figure 12. The sizes considered for horizontal, vertical, and diagonal segments are 100×500 , 500×100 , and 500×500 respectively. It is observed that, irrespective of orientation, the vessel pixel count increases with increasing oscillation frequency. This means that increasing tortuosity is reflected in an increased vessel pixel (white pixels) count. From these observations, we found that tortuosity can be defined as a combination of two parameters:

1. maximum number of vessel pixel occurrence (M); and
2. number of rows (R) having vessel pixel occurrence M and very close to M.

To explore the relevance of parameter M and parameter R in defining tortuosity, the method is applied on an additional nine synthetically generated horizontal vessel segments of size 100×500 (Fig. 13). Here, three normal (normal 1, normal 2, and normal 3), three moderately tortuous (moderate 1, moderate 2, and moderate 3), and three severely tortuous (severe 1, severe 2, and severe 3) vessel segments are taken into consideration so as to include variations in each case. In each of these images, the amplitude is the same, whereas the frequency of oscillation varies. Normal 2 and normal 3 differ from normal 1 in the sense that their oscillation frequency is slightly different . The oscillation frequency of normal 2 is slightly

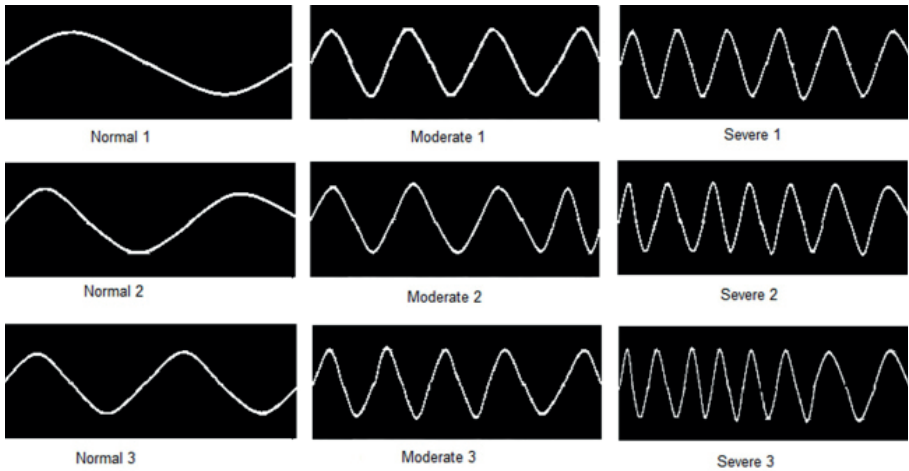


Fig. 13. Synthetically generated horizontal blood vessel segments of normal, moderate, and severe cases.

greater than normal 1, while normal 3 has an oscillation frequency slightly greater than normal 2 but less than moderate 1. Similarly, in the case of moderately tortuous and severely tortuous vessel segments, oscillation frequency increases as we move from the top image to the bottom image (Fig. 13). A small overlap may sometimes exist between normal and moderate as well as moderate to severe case classifications. For instance, normal 3 may overlap (look similar) with moderate 1, and moderate 3 may overlap with severe 1. This requires us to consider the different types of normal, moderate, and severe vessels in our method. Subsequently, nine synthetically generated vertical and diagonal vessel segments, respectively, were also considered. Thus, a total of 27 vessel segments were considered for tortuosity evaluation and thereafter used in the experiment. The mean for parameter M and parameter R is obtained using 27 vessel segments.

In Figure 13, the size of all images is considered to be same. Now, in order to make the method work for blood vessels of different size, amplitude and orientation, four considerations are made for each type of synthetically generated horizontal vessel segments (normal, moderate, and severe) (Fig. 14). These four considerations are:

1. size is considered to be 100×500 ;
2. size is 100×500 , but amplitude is increased;
3. size is now increased to 100×600 , but amplitude is the same as in (1); and
4. size is again increased to 200×700 , but amplitude is the same as in (1).

This gives a total of 12 considerations for horizontal blood vessel segments. Synthetically generated vessel segments with vertical and diagonal orientations were also considered. The mean values for parameter M and parameter R using the proposed method for tortuosity measurement after considering 36 (12 for

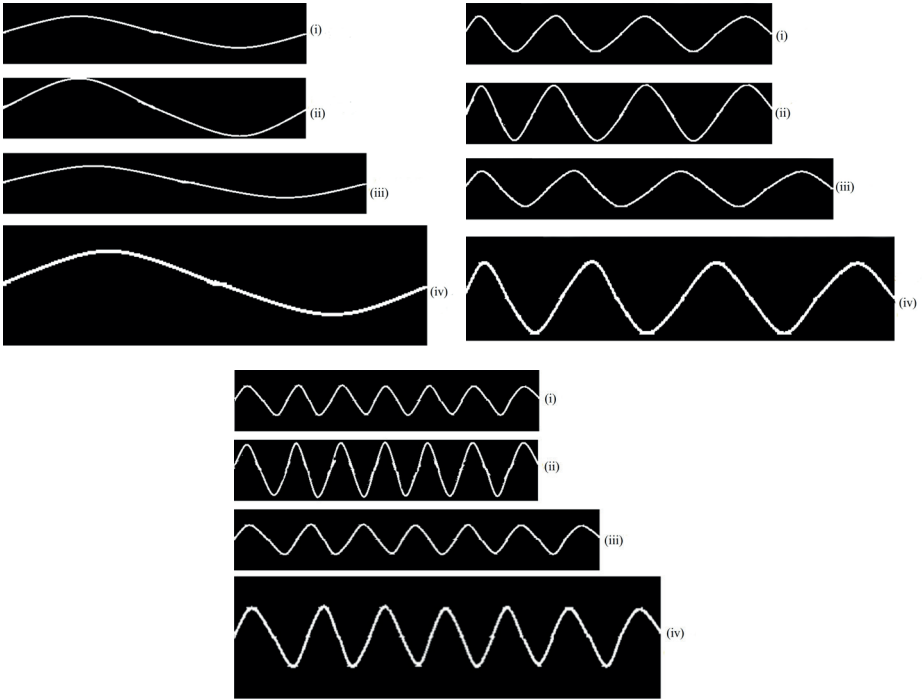


Fig. 14. Synthetically generated (a) normal, (b) moderately tortuous, and (c) severely tortuous horizontal vessel segments of varying amplitude and size.

horizontal, 12 for vertical, and 12 for diagonal vessel segments) synthetically generated vessel segments are noted down. The average values of M and R are calculated by considering the 27 and 36 numbers of vessel segments and are used for evaluating retinal vessel segment tortuosity. The results obtained from synthetically generated vessels thus constitute the baseline for evaluating the tortuosity of actual retinal blood vessels.

After applying the method on different synthetically generated vessel segments, the method was then applied to measure the tortuosity of actual retinal blood vessels. As different retinal images contain blood vessels of different amplitude, size, and orientation, the proposed method is applied to evaluate the tortuosity of retinal vessels. The method was first applied on 20 retinal images collected from the DRIVE database,¹⁷ 30 retinal images collected from the HRF database,¹⁸ and 5 retinal images collected from a local eye hospital. These databases contain a large number of retinal images, thus allowing us to test the system to its full potential.²² For each of these images, five horizontal, five vertical, and five diagonal blood vessel segments were considered. This implies that, from a single retinal image, 15 blood vessel (artery and vein) segments were considered. Therefore, the experiment was

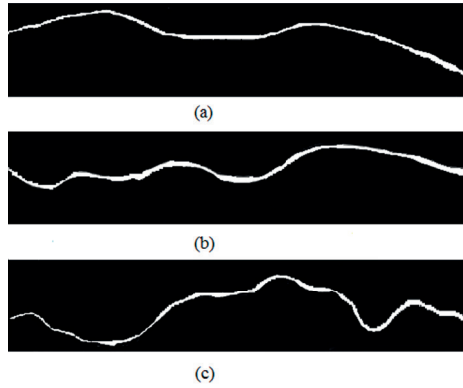


Fig. 15. Normal, (a) moderately tortuous (b), and severely tortuous (c) retinal blood vessel segments oriented horizontally.

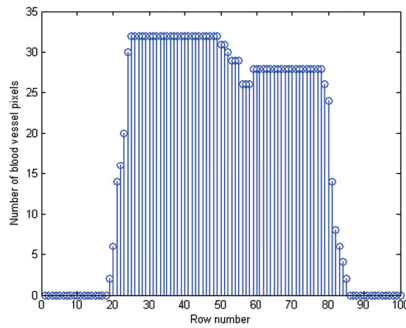
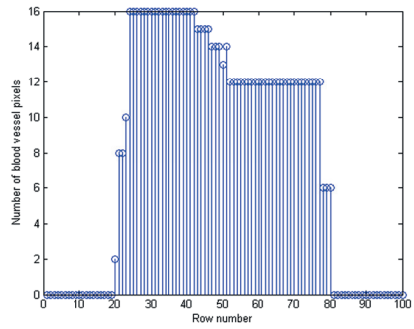
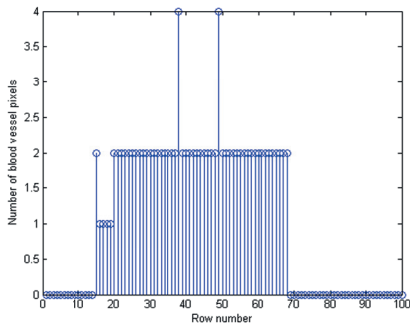


Fig. 16. Histogram of (a) normal, (b) moderately tortuous, and (c) severely tortuous retinal blood vessel segments.

performed on a total of 825 blood vessel segments to classify them as normal, moderately tortuous, or severely tortuous. Figure 15 illustrates a few horizontal retinal blood vessel image segments of a normal, moderately tortuous, and severely tortuous nature that were extracted from a retinal image. The corresponding histogram plot of blood vessel pixels is shown in Figure 16a-c. The results of tortuosity evaluation of retinal blood vessel segments using the proposed method is summarized in the Results section.

We would like to mention that we did not consider arteries and veins separately in the case of synthetically generated blood vessels, considering instead a general curve representing the blood vessel. We did, however, consider different types of synthetically generated vessel segments in relation to amplitude, size, and orientation. After conducting rigorous experiments on these synthetic vessels, the algorithm was applied to measure the tortuosity of actual retinal blood vessel segments containing both arteries and veins.

3.5. Evaluation

After applying the method on the retinal vessel segment images of the DRIVE¹⁷ and HRF¹⁸ database, the last stage of the proposed method is to evaluate the efficiency of our method in determining tortuosity. To do this, the retinal vessel segment images (30 arteries, 30 veins) from the RET-TORT database¹² are used. The image size for arteries ranges from 78×931 to 266×932 and the image size for veins ranges from 52×931 to 259×931 . All these images are provided with a clinical order number by a retinal specialist which represents the tortuosity level. It will be referred to as RET-TORT order in our method. By observing the vessel segments and their clinical order, these 30 vessel segment images are grouped into three categories:

1. RET-TORT order 1-11: Normal blood vessel (these vessel segments consist of fewer turns/twists);
2. RET-TORT order 12-27: Moderately tortuous blood vessel (number of turns/twists are greater than normal but fewer than severely tortuous vessel); and
3. RET-TORT order 28-30: Severely tortuous blood vessel (number of turns/twists are greater than moderately tortuous).

This grouping is done on the basis of visual examination of blood vessels from several images and based on the subjective opinion of different subjects. If the clinical ordering of the vessels and the results of the proposed method are similar, then it can be concluded that the proposed method has the capability of measuring the tortuosity of retinal blood vessels.

4. Results

The results for nine horizontal vessel segments (three normal, three moderately tortuous, and three severely tortuous), subsequently extended to nine vertical and

Table 1. Mean of M and R for 27 synthetically generated blood vessel segments

Blood vessel orientation	Type of blood vessel	Parameter M	Parameter R
Horizontal	Normal	7	12
	Moderate	17	26
	Severe	28	21
Vertical	Normal	7	9
	Moderate	17	21
	Severe	28	14
Diagonal	Normal	5	4
	Moderate	7	10
	Severe	8	5

nine diagonal vessel segments (three normal, three moderately tortuous, and three severely tortuous, respectively), as shown in Figure 13, are presented in Table 1. For all vessel orientations — horizontal, vertical, and diagonal— parameter M and parameter R for normal, moderately tortuous, and severely tortuous vessels is obtained by taking the mean of three types of normal, three types of moderately tortuous, and three types of severely tortuous vessels, respectively. It is clear from Table 1 that the maximum vessel pixel count (M) increases from normal to moderately tortuous, and from moderately tortuous to severely tortuous vessels. The number of rows (R) having the maximum count (M) also increased as compared to normal vessels.

To eliminate bias in the method, the procedure was executed on 36 synthetically generated vessel segments of different size and amplitude, as shown in Figure 14. The results are presented in Table 2. The results illustrate that, irrespective of orientation, size, and amplitude, the tortuosity of the blood vessel segments increases with increasing oscillation frequency (curviness) of the blood vessel segments.

On taking the average of M and R from Table 1 and Table 2, the following conclusions can be drawn:

1. for normal vessels, 'M' and 'R' ≤ 10
2. for moderately tortuous vessels, 'M' or 'R' fall in the range of 11-20; and
3. for severely tortuous vessels, 'M' or 'R' ≥ 21 .

Applying these ranges to actual retinal blood vessels, we found that out of 825 retinal blood vessel segments, there are a total of 605 normal, 217 moderately tortuous, and 3 severely tortuous blood vessel segments. The results for parameters M and R, used for evaluating the tortuosity of retinal blood vessel segments employing the proposed method, are presented in Table 3. Parameters M and R for normal,

Table 2. Mean of M and R for 36 synthetically generated blood vessel segments after considering the four cases

Blood vessel orientation	Type of blood vessel	Parameter M	Parameter R
Horizontal	Normal	5	15
	Moderate	16	14
	Severe	28	17
Vertical	Normal	8	15
	Moderate	12	24
	Severe	24	33
Diagonal	Normal	5	3
	Moderate	8	5
	Severe	9	5

Table 3. Tortuosity of retinal blood vessel segments using the proposed method

Blood vessel orientation	Type of blood vessel	Parameter M	Parameter R
Horizontal	Normal	8	5
	Moderate	13	6
	Severe	22	10
Vertical	Normal	8	5
	Moderate	13	5
	Severe	21	10
Diagonal	Normal	6	5
	Moderate	7	10
	Severe	8	12

moderately tortuous, and severely tortuous vessels oriented in horizontal, vertical and diagonal directions are obtained by finding the average for all normal, moderately tortuous, and severely tortuous vessels, respectively. These results were verified by conducting subjective evaluations, as discussed in the next section.

To check the validity of our method, the method was evaluated by comparing with the vessel segment images in the RET-TORT database.¹² The evaluation of the

Table 4. Comparison between RET-TORT order and proposed method

RET-TORT order	Visual examination	'M' of the proposed method	'R' of the proposed method	Remark of the proposed method
1	Normal	6	7	Normal
2	Normal	8	1	Normal
3	Normal	10	1	Normal
4	Normal	10	1	Normal
5	Normal	10	2	Normal
6	Normal	10	1	Normal
12	Moderate	12	3	Moderate
13	Moderate	14	3	Moderate
14	Moderate	20	4	Moderate
15	Moderate	16	4	Moderate
16	Moderate	14	8	Moderate
17	Moderate	18	3	Moderate
28	Severe	19	8	Moderate
29	Severe	18	7	Moderate
30	Severe	18	9	Moderate

proposed method closely follows the clinical ordering of vessels as provided by the RET-TORT database. A number of results showing a comparison between the ranking of RET-TORT vessel segment images using our proposed method and the clinical ordering by the retinal specialist in the RET-TORT database are presented in Table 4. However, it was found that, in some cases, the method was not able to classify severe cases correctly, classifying them instead as moderate. Nonetheless, normal cases were treated correctly. Table 4 shows that, although severe cases were classified as moderately tortuous by the proposed method, the values of parameter M and parameter R lie close to the upper limit of moderately tortuous blood vessels (M or R close to 20). This shows that there is a small overlap between normal to moderate and moderate to severe case classifications.

The experimental results show that the proposed method evaluates tortuosity efficiently and vessels are classified accordingly into normal, moderately tortuous and severely tortuous.

5. Subjective evaluation

To investigate the effectiveness of the proposed method, the tortuosity of different retinal vessels used in the method were also evaluated subjectively. Three post-graduate students and three research scholars working in the field of retinal image processing subjectively evaluated the tortuosity of blood vessel segments. Blood vessels from ten retinal images belonging to the HRF database were cropped out manually and displayed to the subjects as normal, moderately tortuous, and severely tortuous according to the number of twists and turns. The subjects were thus initially trained to identify normal and tortuous blood vessels and asked to provide an opinion score of 1 for normal, 2 for moderately tortuous, and 3 for severely tortuous blood vessels. The 825 blood vessel segment images were then arranged randomly to assess the ability of the subjects in identifying the blood vessels. The mean opinion score (MOS) was calculated for each image and a graph was plotted (Fig. 17). The subjective results state that out of those 825 blood vessel segments, 610 were normal, 210 were moderately tortuous, and 5 were severely tortuous blood vessel segments. This indicates that the method results correlate closely with the subjective evaluation.

6. Discussion

The method presented in this paper can be effectively used to evaluate retinal blood vessel tortuosity. The tortuosity evaluation using synthetically generated vessel segments shows promising results. The range of values for parameters M and R were obtained from these experiments and thus used as a baseline for measuring retinal blood vessel tortuosity. When the method is applied to actual retinal blood vessel segments obtained from retinal images of publicly available databases, the results obtained show that vessels are classified as normal, moderately tortuous, and severely tortuous. While many of the existing tortuosity evaluation methods have not been applied to retinal vessel segments, our method was tested on artery and vein retinal vessel segments. Furthermore, only a limited number of methods have classified the vessels, but the databases used in the work are not publicly available.^{11,15} In our method, most of the images were obtained from publicly available databases. The results of our method were also compared with the clinical ordering of images in the RET-TORT database. The experimental results and the clinical ordering of images provided by the retinal specialist in the RET-TORT database as well as the results of subjective evaluation closely match and hence, the proposed method can be efficiently used for evaluating the tortuosity of blood vessels. However, we have observed the following limitations in the proposed method:

1. There is an overlap in classification between normal and moderately

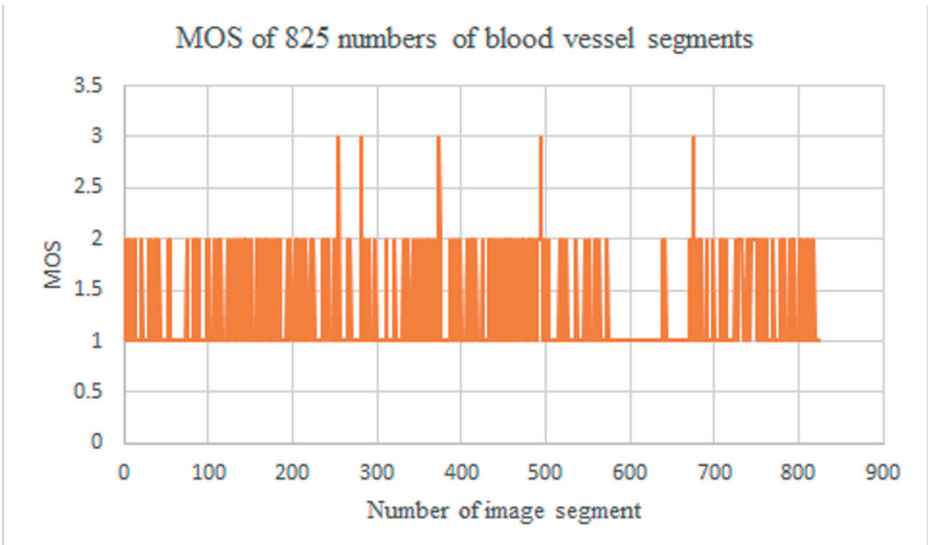


Fig. 17. MOS graph from the 6 subjects for 825 blood vessel segments.

tortuous blood vessels, and between moderately tortuous and severely tortuous blood vessels.

2. We have used a simple threshold-based image segmentation technique; nonetheless, the segmentation results were sufficient for performing our method.

We observed that, in a few images, some unwanted regions that were not part of the vessels remained after the segmentation step, which may have affected our results to some extent. Thus, improving segmentation quality is essential for obtaining better results.

7. Conclusion

The aim of this study is to measure the tortuosity of retinal blood vessels, which may help in detecting hypertensive retinopathy. We propose a simple but efficient image processing-based method to measure the tortuosity of retinal blood vessels. We found that in binary blood vessel images, the vessel pixel (white pixels) count increases with increasing vessel tortuosity. Two parameters were used to evaluate tortuosity. One is parameter M, which represents the maximum vessel pixels; the other is parameter R, which is described as the number of rows having M vessel pixels. The values of parameters M and R increase from normal to moderately tortuous, and from moderately tortuous to severely tortuous vessels. When the method was applied to the actual retinal blood vessel segments, the results obtained shows that

vessels are classified as normal, moderately tortuous, and severely tortuous. The method was also applied on tortuous vessel database (RET-TORT) images and the measured tortuosity level closely matches with the expert ranking. Similarly, there was a strong correlation between retinal vessel classification using the proposed method and retinal vessel classification performed by different subjects. Our future work will focus on testing the entire blood vessel instead of considering only segments and then classifying them as normal or tortuous. Given that very few tortuous images were considered in the work, we also plan to collect hypertensive retinopathy images in order to apply the method on them.

Acknowledgements

The authors would like to acknowledge Dr. Narayan Bardoloi, Medical Director of Chandraprabha Eye Hospital (Jorhat, Assam, India) for providing the necessary materials and giving his valuable suggestions and guidance for carrying out this research work.

References

1. Wang X, Cao H, Zhang J. Analysis of retinal images associated with hypertension and diabetes. In: Engineering in Medicine and Biology Society, 2005. IEEE-EMBS 2005. 27th Annual International Conference of the 2006 Jan 17 (pp. 6407-6410). doi:10.1109/IEMBS.2005.1615964.
2. Talu S. Characterization of retinal vessel networks in human retinal imagery using quantitative descriptors. *Human and Veterinary Medicine*. 2013;5(2):52-57.
3. Bhargava M, Wong TY. Current concepts in hypertensive retinopathy. *Retinal Physician*; 2013. Available from: <https://www.retinalphysician.com/issues/2013/nov-dec/current-concepts-in-hypertensive-retinopathy>
4. Wong TY, McIntosh R. Hypertensive retinopathy signs as risk indicators of cardiovascular morbidity and mortality. *Br Med Bull*. 2005 Sep 7;73-74 (1):57-70. doi:10.1093/bmb/ldh050.
5. Dougherty G, Varro J. A quantitative index for the measurement of the tortuosity of blood vessels. *Med Eng Phys*. 2000;22(8):567-574.
6. Oh KT. Ophthalmologic manifestations of hypertension, 2016. Available from: <https://emedicine.medscape.com/article/1201779-overview>.
7. Patasius M, Marozas V, Lukosevicius A, Jegelevicius D. Model based investigation of retinal vessel tortuosity as a function of blood pressure: preliminary results. In: Engineering in Medicine and Biology Society, 2007. EMBS 2007. 29th Annual International Conference of the IEEE 2007 Aug 22 (pp. 6459-6462). doi:10.1109/IEMBS.2007.4353838
8. Mondal RN, Martin MA, Rani M, et al. Prevalence and risk factors of hypertensive retinopathy in hypertensive patients. *J Hypertens*. 2017;6(2):1-5. doi:10.4172/2167-1095.1000241
9. Duncan BB, Wong TY, Tyroler HA, Davis CE, Fuchs FD. Hypertensive retinopathy and incident coronary heart disease in high risk men. *Br J Ophthalmol*. 2002;86(9):1002-1006.
10. Ong YT, Wong TY, Klein R, et al. Hypertensive retinopathy and risk of stroke. *Hypertension*. 2013 Oct;62(4):706-11. doi:10.1161/HYPERTENSIONAHA.113.01414.

11. Sharbaf MA, Pourreza HR, Banaee T. A novel curvature-based algorithm for automatic grading of retinal blood vessel tortuosity. *IEEE J Biomed Health Inform.* 2016;20(2):586-595. doi:10.1109/JBHI.2015.2396198.
12. BioImLab-Laboratory of Biomedical Imaging- Retinal Vessel Tortuosity Data Set. Available from: <http://bioimlab.dei.unipd.it/Retinal%20Vessel%20Tortuosity.htm>
13. Grisan E, Foracchia M, Ruggeri A. A novel method for the automatic grading of retinal vessel tortuosity. *IEEE Trans Med Imaging.* 2008;27(3):310-319. doi:10.1109/TMI.2007.904657.
14. Cavallari M, Stamile C, Umeton R, Calimeri F, Orzi F. Novel method for automated analysis of retinal images: results in subjects with hypertensive retinopathy and CADASIL. *Biomed Res Int.* 2015;2015:752957. doi: 10.1155/2015/752957.
15. Turior R, Onkaew D, Uyyanonvara B, Chutinantvarodom P, Orzi F. Quantification and classification of retinal vessel tortuosity. *ScienceAsia.* 2013;39(3):265-277. doi:10.2306/scienceasia1513-1874.2013.39.265
16. El Abbadi NK, Al Saadi EH. Automatic retinal vessel tortuosity measurement. *Journal of Computer Science.* 2013;9(11):1456-1460. doi: 10.3844/jcssp.
17. DRIVE database. Available from: <http://www.isi.uu.nl/Research/Databases/DRIVE>.
18. High-Resolution Fundus (HRF) Image Database. Available from: <https://www5.cs.fau.de/research/data/fundus-images>
19. Shome SK, Vadali SRK. Enhancement of diabetic retinopathy imagery using contrast limited adaptive histogram equalization. *International Journal of Computer Science and Information Technologies.* (2011;2(6):2694-2699.
20. Umbaugh S. *Computer vision and image processing.* New Jersey: Prentice Hall; 1998.
21. Singh TR, Roy S, Singh OI, Sinam T, Singh KM. A New adaptive thresholding technique in binarization. *International Journal of Computer Science Issues.* 2011;8(6):271-277.
22. Chetia S, Nirmala SR. Retinal blood vessel tortuosity measurement for analysis of hypertensive retinopathy. In: *Innovations in Electronics, Signal Processing and Communication (IESC), 2017 International Conference on 2017 Apr 6* (pp. 45-50). doi:10.1109/IESPC.2017.8071862



A socioeconomic evaluation of early-stage and moderate glaucoma patients

Miglė Lindžiūtė¹, Ingrida Janulevičienė²

¹Faculty of Medicine, Lithuanian University of Health Sciences, Kaunas, Lithuania;

²Department of Ophthalmology, Lithuanian University of Health Sciences, Kaunas, Lithuania

Abstract

Purpose: The aim of this study was to compare costs related to glaucoma treatment for early- and moderate-stage glaucoma patients.

Design: Descriptive observational study.

Methods: The study was conducted at the Eye Clinic in the Hospital of the Lithuanian University of Health Sciences Kauno Klinikos in Lithuania. An original questionnaire was administered to 80 open-angle glaucoma patients. Data regarding the age, gender, living area, occupation, income, concomitant diseases, frequency of outpatient visits, use of topical antiglaucoma and other medications, treatment and transportation costs were collected. The Hodapp classification was used to divide patients into two main groups of early- and moderate-stage glaucoma according to visual field loss. Results with $p < 0.05$ were interpreted as statically significant.

Results: There were 37 patients with early-stage glaucoma and 43 patients with moderate glaucoma. Moderate stage glaucoma patients were 73 (± 8) years old, while patients with early-stage glaucoma were 63 (± 11) years old, ($p < 0.001$). Early-stage glaucoma patients visited their ophthalmologist 2.5 (± 1.5) times per year, while patients with moderate glaucoma had 4.4 (± 2.7) outpatient visits per year ($p < 0.001$). Patients with early-stage glaucoma used 1.8 (± 0.9) medications, while patients with moderate glaucoma used 2.9 (± 0.9) medications ($p < 0.001$). Combined costs for treatment and transportation totaled an average of 4.7% of patient income. Patients that were in the early stages of glaucoma spent about 3.2% of their annual income for glaucoma care and transportation, while patients with

Correspondence: Miglė Lindžiūtė. P. Luksio street 8 – 25, LT-49355 Kaunas, Lithuania.
E-mail: migle.lindziute@gmail.com

moderate-stage glaucoma spent about 5.9% of their income ($p = 0.003$).

Conclusion: Moderate-stage glaucoma patients had significantly higher expenses related to glaucoma than early-stage glaucoma patients. Costs related to glaucoma comprised a significantly greater part of the income of patients who were retired than patients who were employed.

Keywords: cost evaluation, economic evaluation, glaucoma, glaucoma management, glaucoma treatment costs, socioeconomics

1. Introduction

Glaucoma is a neurodegenerative disorder in which degenerating retinal ganglion cells produce significant visual disability.¹ Despite the fact that the pathogenesis of glaucoma is not completely understood, it is widely accepted that elevated levels of intraocular pressure compress the optic nerve and cause progressive optic neuropathy associated with visual field loss.

Intraocular pressure is determined by the balance between secretion of aqueous humor by the ciliary body and its drainage through two independent pathways: the trabecular meshwork and the uveoscleral outflow pathway.² When aqueous humor outflow is disrupted, intraocular pressure increases. This disruption can occur when the drainage at the trabecular meshwork is blocked (in the case of open-angle glaucoma) or when there is a narrowing of the angle of drainage (in the case of angle-closure glaucoma). Since prolonged periods of elevated intraocular pressure lead to vision loss, glaucoma can result in complete blindness.

Glaucoma is the cause of approximately 12% of cases of blindness.³ About 10–11% of cases of blindness in Western Europe and USA are caused by glaucoma, and these numbers are increasing.⁴ It is estimated that 3% of the global population over 40 years of age currently has glaucoma, the majority of whom are undiagnosed.⁵ Projections estimate the prevalence of glaucoma worldwide will rise to 79.6 million by 2020 and counting as the population continues to age.⁶

Since the glaucomatous process is irreversible and glaucoma is often asymptomatic during the early stages, diagnosis and treatment are crucial before the process reaches advanced stages.^{7–9} Therefore, early intervention is essential to slow disease progression.² The main objective of treatment is to preserve the quality of life of the patient by slowing visual loss.

Reduction of intraocular pressure is the only proven method to treat glaucoma.¹⁰ The target intraocular pressure should be achieved with the minimum amount of medications and fewest possible adverse effects. There are several classes of medications that lower intraocular pressure, including: prostaglandin analogues, β -adrenergic blockers, α -adrenergic antagonists, carbonic anhydrase inhibitors, and cholinergic antagonists. In general, prostaglandin analogues are the first line of

medical therapy. This drug class reduces intraocular pressure by reducing outflow resistance, resulting in increased aqueous humor flow through the uveoscleral pathway.¹¹ However, as the disease progresses, patients usually require more than one medication to lower their intraocular pressure.¹²

Since glaucoma is not curable, patients affected with glaucoma require treatment for the rest of their lives. Lifelong treatment of glaucoma poses a financial challenge to the patient; this affects drug compliance, which plays a major role in treatment outcome.¹³ The fact that patients need more antiglaucoma medications as the disease progresses suggests that the direct costs of glaucoma treatment increase as disease severity worsens.^{14,15} Therefore, patients with moderate and advanced glaucoma have higher economic challenges than the healthy population or patients in the early stages of glaucoma.¹⁶

The prevalence of glaucoma in Lithuania has been rising in the past decade from a rate of 25.6/1000 in 2011 to 30.6/1000 in 2015.¹⁷ A compulsory health insurance model has been established in Lithuania by the Law on Health Insurance and other laws. This model is based on the principles of universality and provides the possibility of receiving individual healthcare services financed from the Compulsory Health Insurance Funds to insured individuals.¹⁸ Reimbursable medicines are prescribed to patients in an outpatient setting by primary care physicians or specialists. Most insured patients diagnosed with glaucoma are reimbursed at 80% of glaucoma medication costs. However, there is insufficient information about the direct costs of glaucoma treatment and care paid for by patients in Lithuania, as the socio-economic aspects of glaucoma in the country have never been investigated before.

Therefore, the objective of this study was to determine the relation between demographic characteristics, stage of glaucomatous process, and economic challenges of treatment and other costs related to glaucoma.

2. Methods

A descriptive observational study was conducted at the Eye Clinic of the Hospital of the Lithuanian University of Health Sciences Kauno Klinikos from June to August 2017. The goal of our study was to find out whether early detection and treatment of glaucoma could significantly reduce the economic burden of this disease.

In order to compare the economic challenges of treatment and other costs related to the stage of glaucoma, the calculated sample size providing 80% power to detect a standardized difference of 1.5 in treatment cost between early and moderate glaucoma groups was 35 in each group, assuming two-sided tests and a 5% significance level. An original questionnaire was administered to 80 patients with open-angle glaucoma. There were 37 patients (46.3%) with early-stage glaucoma and 43 patients (53.8%) with moderate glaucoma.

Inclusion criteria were:

1. patients older than 18 years of age;
2. diagnosed with open-angle glaucoma by a qualified glaucoma specialist at least two years before the questionnaire was administered;
3. actively treated with topical antiglaucoma medications; and
4. willing and able to give consent.

Exclusion criteria were:

1. patients with end-stage glaucoma;
2. patients who underwent surgical or laser glaucoma treatment;
3. advanced age-related macular degeneration, vitreous hemorrhage, diabetic retinopathy, or any progressive retinal or optic nerve disease other than glaucoma; and
4. refusal to give informed consent.

Informed consent was obtained from all participants before they participated in the study. The study was conducted in accordance with the Declaration of Helsinki and approved by our institutional Research Ethics Committee – Lithuanian University of Health Sciences Centre for Bioethics.

The questionnaire was composed of a set of 28 questions. Collected data included:

1. age and gender;
2. occupation and income;
3. frequency of outpatient visits;
4. living area, means, cost, and duration of transportation;
5. concomitant diseases;
6. use and costs of topical antiglaucoma medications; and
7. use of systemic medications.

Data about costs of replacing glasses, loss of wellbeing, rehabilitation, nursing, and other indirect costs such as lost earnings and productivity were not included. Costs related to glaucoma screening were not included in the evaluation of treatment costs since these services are fully compensated by the Compulsory Health Insurance Fund.

The patients were divided into two main groups of early-stage and moderate-stage glaucoma using the Hodapp–Parrish–Anderson classification,¹⁹ which is based on visual field assessment. Typically, the visual field is assessed by standard automated perimetry, in which patients respond to light dots presented at fixed locations in the field of vision by a perimeter that determines a sensitivity threshold for each location.²⁰

Glaucomatous loss was defined as:

- mean deviation (MD) < -6 dB;
- fewer than 18 points depressed below the 5% probability level and fewer than 10 points below the $p < 1\%$ level; and
- no point in the central 5° with a sensitivity of less than 15 dB.

Moderate glaucomatous loss was defined as:

- MD < -12 dB;
- fewer than 37 points depressed below the 5% probability level and fewer than 20 points below the $p < 1\%$ level;
- no absolute deficit (0 dB) in the central 5°; and
- only one hemifield with sensitivity of < 15 dB in the central 5°.

Patients with advanced glaucomatous loss were not included in this study.

Statistical analysis was performed using a software package SPSS v. 17.0 (IBM Corp., Armonk, NY, USA). Independent samples Student's *t*-tests were used to compare and determine the equality of means in two populations. The one-way analysis of variance (ANOVA) was used to determine whether there are any statistically significant differences between the means of three or more independent groups. The Mann-Whitney U test was used to compare the differences between two independent groups, while the dependent variable was ordinal. The Chi-square test of independence was used to analyze differences in two groups when the dependent variable was measured at a nominal level. Pearson correlation coefficient was used to measure the linear correlation between two variables. Cramer's V coefficient factor was used to measure the association between two nominal variables. Results with a significance level of $p < 0.05$ were interpreted as statistically significant.

3. Results

Eighty open-angle glaucoma patients participated in the study. Demographic characteristics, rates of comorbidity, and types of medications used to treat glaucoma are shown in Table 1. The average age of male subjects was 66.8 (± 10.6) years and the average age of female subjects was 69.2 (± 11.1) years, $p = 0.343$. There was no significant difference between the average age of males and females.

Patients were diagnosed with glaucoma for an average of 9.2 (± 7.3) years (minimum of 2 years; maximum of 30 years). Participants visited their ophthalmologist on average about 3.3 (± 1.7) times per year (minimum 1, maximum 7).

There was no significant correlation between the amount of outpatient visits per year and the age of patients ($r = 0.002$; $p = 0.985$) and distance needed to travel to the hospital ($r = 0.129$; $p = 0.254$). Employed patients had an average of 3.5 (± 2.3) visits per year, while retired patients had 3.6 (± 2.6) visits per year, showing that there was no significant relationship between employment status and number of outpatient visits per year, $p = 0.833$. However, from the 31 employed glaucoma patients, 21 (67.7%) had to take a day off to visit their ophthalmologist.

Patient income was distributed in the groups up to € 300 and from € 300 to 500, while only less than a fifth of patients had an income above € 500 (Fig. 1).

On average, patients lived 51 (± 66) km (minimum 1 km; maximum 260 km) away from the hospital. Most patients came to the hospital by private car or public trans-

Table 1. Demographic characteristics, concomitant diseases, and types of medications used to treat glaucoma of patients included in the study

	All patients
Age, mean \pm SD, years	68.3 \pm 10.9
Sex, N (%)	
Male	30 (37.5)
Female	50 (62.5)
Employment status, N (%)	
Employed	31 (38.8)
Retired	49 (61.2)
Rates of comorbidity, N (%)	
Cataracts	27 (33.8)
Arterial hypertension	46 (57.5)
Type 2 diabetes	10 (12.5)
Circulatory system conditions	5 (6.3)
Asthma	5 (6.3)
Type of medications used, N (%)	
β -adrenergic blockers	54 (67.5)
Carbonic anhydrase inhibitors	51 (63.8)
α -adrenergic antagonists	26 (32.5)
Prostaglandin analogs	58 (72.6)

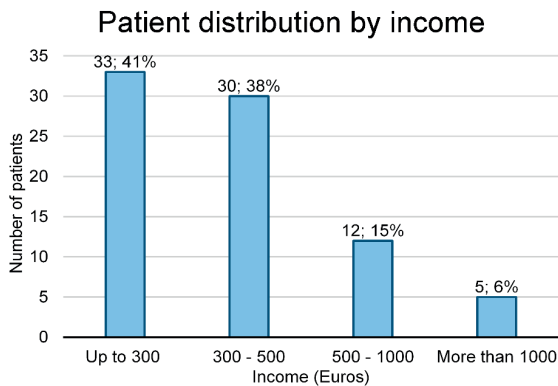


Fig. 1. Distribution of patients in different income groups. The income of most patients was up to € 300 and between € 300 and 500, while only less than a fifth of patients had an income above € 500.

Choice of transport and distance by mean of transport

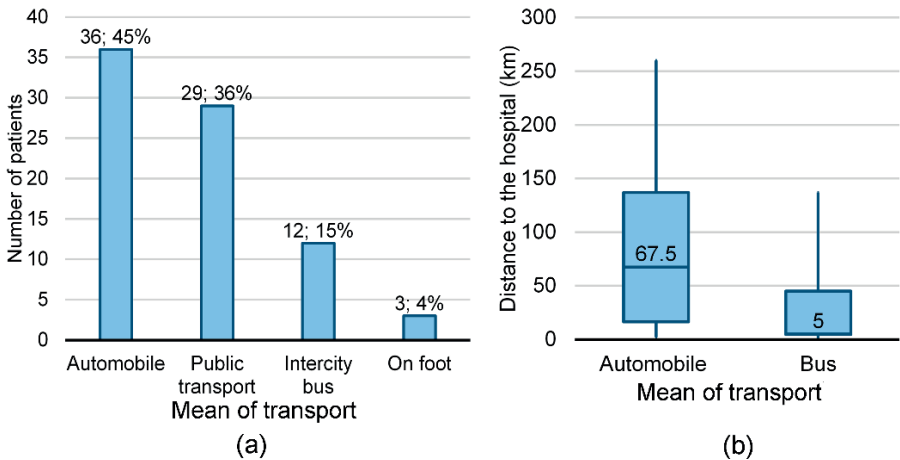


Fig. 2. Chosen means of transport and variation of distance by mean of transport. (a) Distribution of chosen transport means used to arrive to the hospital. (b) Box-plot showing the average distance needed to travel to the hospital by different means of transport.

portation, and some using an intercity bus or on foot (Fig. 2a). Patients who came by automobile lived statistically significantly further away than the ones that came to the hospital by bus, $p < 0.001$ (Fig. 2b). Twenty-four (30%) patients drove themselves to outpatient visits and 12 (15%) were taken to the hospital by a family member or friend. The average time it took for participants to get to the hospital was 1 hour, first quartile was up to 20 minutes, the median was 30 minutes, and the third quartile was 1.5 hours.

Sixty-one (76.3%) patients visited the ophthalmologist by themselves, while the other 19 (23.8%) patients came to the hospital with an accompanying person. Seventeen (89%) of them accompanied the patient because of their inability to travel or get to the hospital alone. Twelve (63%) of the 19 accompanying persons were employed and 6 (50%) of them had to take time off to take the patients to the hospital.

The average cost of travel for one visit to the ophthalmologist was € 10.84 (\pm 12.94) (minimum € 0, maximum € 48). Participants that came to the outpatient visits by bus had an average travel cost of € 4.69 (\pm 5.90), while patients who came to the hospital by car payed statistically significantly more, approximately € 18.72 (\pm 14.84) per visit, $p < 0.001$ (Fig. 3a). Patients who chose to travel to the hospital by bus lived an average of 27 (\pm 36) km to the hospital, while patients who lived further away from the hospital, approximately 83 (\pm 80) km, chose to take an automobile, $p < 0.001$. The result of correlation analyses shows that there was a statistically significant rela-

Transport cost by mean of transport and relation between travel distance and cost

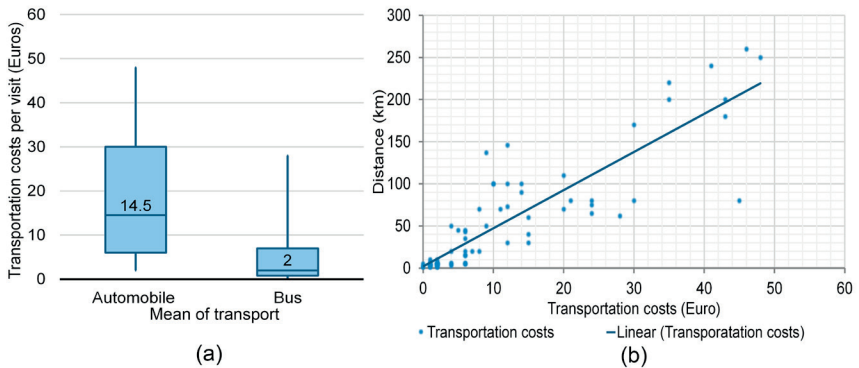


Fig. 3. Transport cost by means of transport and relation between travel distance and cost. (a) The variation of transport costs per one visit by chosen means of transport. (b) Correlation analyses shows that there was a statistically significant relationship between the distance the patient travels to the hospital and travel cost. The scattering of variables and linear regression is shown.

relationship between the distance traveled by patients to the hospital and travel costs, $r = 0.879$, $p < 0.001$ (Fig. 3b).

All the patients who participated in this study were divided into two groups using the Hodapp-Parrish-Anderson classification. There were 37 patients (46.3%) with early-stage glaucoma and 43 patients (53.8%) with moderate glaucoma. Comparison of demographic characteristics between patients with early- and moderate-stage glaucoma outlines that patients with moderate glaucoma were significantly older and more of them were retired than early-stage glaucoma patients. The distribution by sex was not significantly different in these groups, as shown in Table 2.

A summary of distribution of concomitant diseases and conditions in the early and moderate glaucoma groups is shown in Table 3. There were significantly more cases of cataracts in the moderate-stage glaucoma group. There was no significant difference of prevalence of diabetes, arterial hypertension, circulatory system conditions, and asthma between patients with early- and moderate-stage glaucoma.

Participants with early-stage glaucoma had been diagnosed in average for 6.6 (± 5.3) years, while patients with moderate glaucoma had the disease for a longer time period, approximately 11.2 (± 8.3) years, $p = 0.004$. Patients in the early stages of glaucoma visited their eye doctor about 2.5 (± 1.5) times per year, while patients with moderate glaucoma had statistically significantly more visits per year, approximately 4.4 (± 2.7) visits per year, $p < 0.001$. Types of medication used and frequency in use of specific types of antiglaucoma medications are detailed in Table 4.

Table 2. Demographic characteristics of patients with early-stage and moderate glaucoma

	Early-stage glaucoma group	Moderate-stage glaucoma group	χ^2	Cramer's V coefficient	p-value
Age, mean \pm SD, years	62.7 \pm 11.2	73.1 \pm 8.0			< 0.001
Sex, N (%)			0.75	r = 0.097	0.385
Male	12 (15.0)	18 (22.5)			
Female	25 (31.3)	25 (31.3)			
Employment status, N (%)			19.78	r = 0.497	< 0.001
Employed	24 (30.0)	7 (8.8)			
Retired	13 (16.3)	36 (45.0)			

Table 3. Concomitant diseases, conditions of patients that suffer from early and moderate stage glaucoma.

	Early-stage glaucoma group, N (%)	Moderate-stage glaucoma group, N (%)	Cramer's V coefficient	p-value
Cataracts	5 (13.5)	22 (51.2)	r = 0.397	< 0.001
Arterial hypertension	18 (48.6)	28 (65.1)	r = 0.166	0.175
Type 2 diabetes	4 (10.8)	6 (13.9)	r = 0.136	0.745
Circulatory system problems	3 (8.0)	2 (4.7)	r = 0.071	0.658
Asthma	1 (2.7)	4 (9.3)	r = 0.136	0.366

Table 4. Frequency in use of different type antiglaucoma medications in early-stage and advanced glaucoma management

	Early-stage glaucoma group, N (%)	Moderate-stage glaucoma group, N (%)	All patients, N (%)
β-adrenergic blockers	22 (59.5)	32 (74.4)	54 (67.5)
Timolol	22 (59.5)	30 (69.8)	52 (65.0)
Betaxolol	0 (0.0)	2 (4.7)	2 (2.5)
Carbonic anhydrase inhibitors	17 (45.9)	34 (79.1)	51 (63.8)
Brinzolamide	12 (32.4)	21 (48.8)	33 (41.3)
Dorzolamide	5 (13.5)	13 (30.2)	18 (22.5)
α-adrenergic antagonists			
Brimonidine	4 (10.8)	22 (51.2)	26 (32.5)
Prostaglandin analogs	23 (62.2)	35 (81.4)	58 (72.6)
Latanoprost	6 (16.2)	17 (39.5)	23 (28.8)
Bimatoprost	6 (16.2)	8 (18.6)	16 (20.0)
Travoprost	8 (21.6)	9 (20.9)	15 (18.8)
Tafluprost	3 (8.1)	1 (2.3)	4 (5.0)

The distribution of patients by the amount of medications used ranged from one to four topical antiglaucoma drugs (Fig. 4a). Patients with early-stage glaucoma used 1.8 (\pm 0.9) medications on average, while patients with moderate-stage glaucoma used significantly more drugs, 2.9 (\pm 0.9), $p < 0.001$. The results show a statistically significant difference in direct treatment costs depending on the amount of medications used, $p < 0.001$ (Fig. 4b).

The average yearly cost of antiglaucoma medications was € 249.75 (\pm 109.66) per patient (minimum € 36.75, maximum € 463.44). Patients with early-stage glaucoma used medications worth € 196.62 (\pm 105.12), while patients with moderate stage glaucoma had medication costs of € 295.47 (\pm 92.31) per year, $p < 0.001$ (Fig. 5). Patient costs for topical antiglaucoma medications were reimbursed at 80% by the Compulsory Health Insurance Fund of the Republic of Lithuania. The average direct cost for annual medication was € 107.09 (\pm 56.29) (minimum € 14.40, maximum € 264).

Variation in treatment cost by amount of medications used

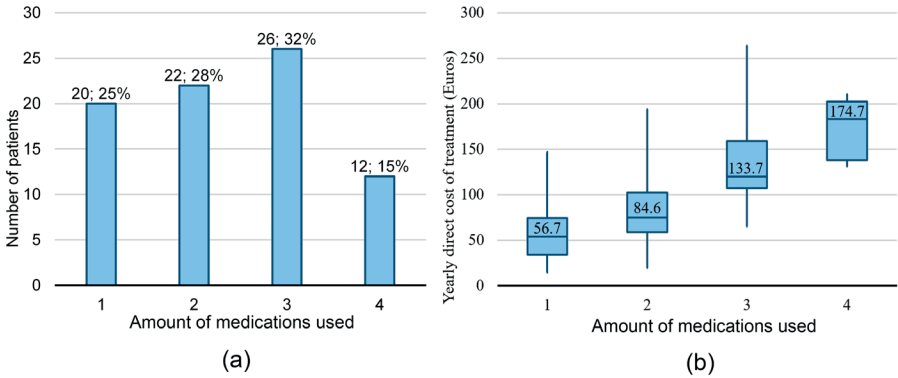


Fig. 4. Patient distribution by the amount of glaucoma medications used and variation of yearly treatment cost by amount of glaucoma medications used. (a) Patient distribution by the amount of glaucoma medications used. (b) Box-plot showing the variation of yearly cost of treatment by the amount of glaucoma medications used. Results show a significant increase of costs depending on the amount of medications used.

Cost of treatment in early and moderate stage glaucoma groups

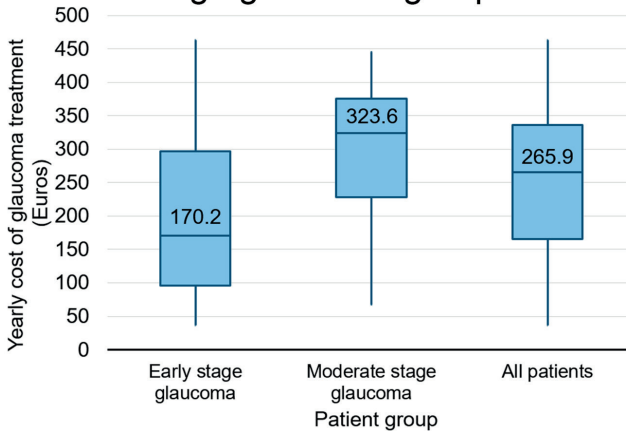


Fig. 5. Variation of yearly treatment cost in early and advanced glaucoma groups. Box-plot showing the variation of yearly cost of treatment in the early-stage and moderate glaucoma groups.

Combined direct patient treatment and travel costs were about € 143.29 (\pm 86.61) per year on average (minimum € 86.61; maximum € 528). Travel costs accounted for about 21% of combined patient costs. Combined costs for treatment and transportation made up about 4.7% of patient income. Patients that were in the early stages of glaucoma spent about 3.2% of their income on costs related to transport and treatment, while patients with moderate-stage glaucoma spent an average of 5.9% of their income, $p = 0.003$. Employed patients spent about 2.7% of their income for direct glaucoma costs, while retired participants spent a significantly higher amount, 5.9% of their earnings, $p = 0.001$.

4. Discussion

The number of people coming to hospital eye departments is likely to increase in the future as a result of an ageing population, increased optometric case findings, and raised public awareness.²¹ This study concludes that patients with moderate-stage glaucoma were significantly older than patients with early-stage glaucoma. This and data from other studies suggest that older age increases the risk of glaucoma progression.²²

Patients with moderate-stage glaucoma had a higher number of yearly ophthalmologist visits and had glaucoma for a significantly longer time. This shows that patients who suffer from glaucoma longer have a higher progression rate of the disease. Participants of this study who had a moderate glaucomatous process tended to need more medication to reach their target intraocular pressure, which amounts to higher treatment costs.

Many other studies that have researched the economic burden of glaucoma concluded that, as disease severity worsens, resource utilization and direct medical treatment costs increase. This increase in costs was observed in a study done in Europe, which concluded that direct treatment costs increased by € 86 by each incremental step (from € 455 in stage 1 to € 969 in stage 4).¹⁵ A study conducted in the USA showed a similar outcome, finding that treatment costs amounted to US\$ 623 in early-stage glaucoma, US\$ 1915 in advanced glaucoma, and US\$ 2511 in end-stage glaucoma.²³ Likewise, as seen in literature reviews, it appears that several other studies have come to the same result, namely, that increased disease severity is associated with increased costs.²⁴ This concludes that older patients with moderate and advanced glaucoma are facing a much higher economic burden than younger patients with early-stage glaucoma.

Glaucoma management strategies aimed at slowing or stopping disease progression, if effective, would be expected to significantly reduce the economic burden of this chronic disease over many years.¹⁵ Early disease recognition, proactive management, and prevention of progression beyond the early stages may reduce the overall national and personal economic burden, limit the reduction of

productivity from vision loss, and preserve quality of life.^{5,15,25} Home tonometers would transfer a considerable portion of IOP follow-up to patients themselves, similar to measuring blood sugar and blood pressure at home. The time of medical professionals would be freed to other patients who could benefit more from their care.²⁶

Findings about costs related to glaucoma treatment might vary in different countries and studies, but an objective way to observe the differences in glaucoma costs is comparing costs to patient income. In a study conducted in Sweden, the mean annual cost for glaucoma treatment and care was € 476.²⁷ Other studies undertaken in France and Sweden show that patients spent an average of € 390 and € 531, respectively.²⁸ According to data published by the Organization for Economic Co-operation and Development, the average yearly wage is € 41,835 (SEK 399,988) in Sweden and € 36,809 in France.²⁹ From this data, we can see that glaucoma patients in Sweden spend about 1.1–1.3% of their income on costs related to glaucoma, while patients in France spend about 1% of their income.

In our study, patients spent an average of € 143 annually for glaucoma medications and transport costs combined. The average net monthly earning in Lithuania in 2016 was € 602.30 (yearly income of € 7227.60).³⁰ Working patients spent about 2.7% of their income on glaucoma treatment and transportation. The average monthly state social insurance pension in 2015 was € 244.50 (yearly income of € 2934).³¹ Since more patients in the moderate-stage glaucoma group were retired and their income came from social insurance pensions, they spent a greater amount of their monthly pay, approximately 5.9%, for glaucoma care. It is evident that glaucoma poses a higher economic burden on this social group.

In our study, direct costs for medication comprised 79% of combined costs. In a study conducted in Europe, medication costs represent a minimum of 42% of total direct cost at any disease stage.¹⁵ Drug costs in Denmark accounted for 57% of total glaucoma care costs.³²

Groups of patients for which glaucoma pose a higher economic burden might prefer choosing cheaper alternative antiglaucoma medications with different substance concentrations or might display low treatment compliance due to sparing medication to lower treatment costs. The proportion of patients who deviate from their prescribed medication regimen ranged from 5–80%.³³ Low treatment compliance can cause an increase in intraocular pressure and speed up the rate of glaucoma progression. Treatment compliance is fundamental to reduce glaucoma progression; even a small (1 mmHg) reduction in intraocular pressure could reduce glaucoma progression significantly by approximately 10%.³⁴

Even though average travel costs per visit were about € 10.84 (\pm 12.94), they accounted for 21% of direct costs. There were similar results in a study published about travel costs for glaucoma patients in London hospitals; travel accounted for approximately one-fifth of total patient costs.²¹ It appears that patients who lived further away had higher transportation costs and would choose travel by automobile

more often. This problem may occur due to a lack of glaucoma specialists in their counties.

Our study had several limitations. Costs for office visits, glaucoma examinations, replacing glasses, rehabilitation, nursing, and other indirect costs were not included. Information about lost income during visits and lost productivity was not included, and additional costs incurred by accompanying persons were also not included. We assumed that patients were compliant with treatment and did not measure compliance directly by any objective methods.

5. Conclusion

Glaucoma is a neurodegenerative disorder in which elevated intraocular pressure causes irreversible damage to the retinal ganglion cells. Lifelong treatment is needed to slow disease progression, and as glaucomatous damage progresses, patients require more medications. Moderate-stage glaucoma patients were older, had glaucoma for longer, had more outpatient visits, and used more medications than early-stage glaucoma patients. Costs related to glaucoma comprised a considerable amount of patient income. However, some groups of patients were more affected than others. Our research shows that moderate-stage glaucoma patients had significantly higher expenses related to glaucoma than early-stage glaucoma patients. Likewise, costs related to glaucoma comprised a much higher portion of income for patients who were retired versus those who were employed. Given that retired patients had a lower income and higher glaucoma costs while also having moderate glaucoma more frequently due to disease duration made them a more socially vulnerable group. This shows that early detection and treatment of glaucoma can significantly reduce the economic burden of this disease.

References

1. Cohen LP, Pasquale LR. Clinical characteristics and current treatment of glaucoma. *Cold Spring Harb Perspect Med.* 2014;4(6):a017236. Available from: <http://www.ncbi.nlm.nih.gov/pmc/articles/PMC4031956/>
2. Weinreb R, Aung T, Medeiros F. The pathophysiology and treatment of glaucoma. *JAMA.* 2014;311(18):1901. doi:10.1001/jama.2014.3192
3. Foster A, Resnikoff S. The impact of Vision 2020 on global blindness. *Eye (Lond).* 2005;19(10):1133–1135. doi:10.1038/sj.eye.6701973
4. Bourne RRA, Jonas JB, Flaxman SR, et al. Prevalence and causes of vision loss in high-income countries and in Eastern and Central Europe: 1990–2010. *Br J Ophthalmol.* 2014;12;98(5):629 LP-638. Available from: <http://bjo.bmj.com/content/98/5/629.abstract>
5. Varma R, Lee PP, Goldberg I, Kotak S. an assessment of the health and economic burdens of glaucoma. *Am J Ophthalmol.* 2011;152(4):515–522. Available from: <http://www.ncbi.nlm.nih.gov/pmc/articles/PMC3206636/>

6. Quigley HA, Broman AT. The number of people with glaucoma worldwide in 2010 and 2020. *Br J Ophthalmol*. 2006;90(3):262–7. Available from: <http://www.ncbi.nlm.nih.gov/pmc/articles/PMC1856963/>
7. Leite MT, Sakata LM, Medeiros FA. Managing glaucoma in developing countries. *Arq Bras Oftalmol*. 2011;74(2):83–84. Available from: <http://www.ncbi.nlm.nih.gov/pmc/articles/PMC3787827/>
8. Bettin P, Di Matteo F. Glaucoma: present challenges and future trends. *Ophthalmic Res*. 2013;50(4):197–208. Available from: <http://www.karger.com/DOI/10.1159/000348736>
9. Buys YM, Gaspo R, Kwok K. Referral source, symptoms, and severity at diagnosis of ocular hypertension or open-angle glaucoma in various practices. *Can J Ophthalmol*. 2017;47(3):217–222. doi:10.1016/j.jcjo.2012.03.031
10. Boland MV, Ervin AM, Friedman DS, et al. Comparative effectiveness of treatments for open-angle glaucoma: a systematic review for the US Preventive Services Task Force. *Ann Intern Med*. 2013;158(4):271–279.
11. Stewart WC, Konstas AG, Nelson LA, Kruff B. Meta-analysis of 24-hour intraocular pressure studies evaluating the efficacy of glaucoma medicines. *Ophthalmology*. 2008;115(7):1117e1-1122e1
12. Waldock A, Snape J, Graham C. Effects of glaucoma medications on the cardiorespiratory and intraocular pressure status of newly diagnosed glaucoma patients. *Br J Ophthalmol*. 2000;84(7):710–713. Available from: <http://www.ncbi.nlm.nih.gov/pmc/articles/PMC1723530/>
13. Kumber SK, Mirje M, Moharir G, Bharatha A. Cost analysis of commonly used combination of drugs in primary open angle glaucoma. *J Clin Diagn Res*. 2015;9(5):FC05-FC08. Available from: <http://www.ncbi.nlm.nih.gov/pmc/articles/PMC4484082/>
14. Lorenz K, Wolfram C, Breitscheidel L, Schlaen M, Verboven Y, Pfeiffer N. Direct cost and predictive factors for treatment in patients with ocular hypertension or early, moderate and advanced primary open-angle glaucoma: the CoGIS study in Germany. *Graefes Arch Clin Exp Ophthalmol*. 2013;251(8):2019–2028. doi:10.1007/s00417-013-2354-z
15. Traverso CE, Walt JG, Kelly SP, et al. Direct costs of glaucoma and severity of the disease: a multinational long term study of resource utilisation in Europe. *Br J Ophthalmol*. 2005 89(10):1245–1249. Available from: <http://www.ncbi.nlm.nih.gov/pmc/articles/PMC1772870/>
16. Goldberg I. Stepping up glaucoma management: when and how? *Open Ophthalmol J*. 2009;3:67–69. Available from: <http://www.ncbi.nlm.nih.gov/pmc/articles/PMC2760861/>
17. Gaidelytė R, Garbuviėnė M, Madeikytė N. Lithuanian Ministry of Health Health Information Centre of Institute of Hygiene Health Statistics of Lithuania 2015; Available from: www.hi.lt
18. National Health Insurance Fund under The Ministry of Health. Healthcare in Lithuania. *Vlk.lt*. <http://www.vlk.lt/sites/en/healthcare-in-lithuania/>. Published 2019
19. Susanna R Jr, Vessani RM. Staging glaucoma patient: why and how?. *Open Ophthalmol J*. 2009;3:59–64. 2009. doi:10.2174/1874364100903020059
20. Elze T, Pasquale LR, Shen LQ, Chen TC, Wiggs JL, Bex PJ. Patterns of functional vision loss in glaucoma determined with archetypal analysis. *J R Soc Interface*. 2014;12(103):20141118–20141118. doi:10.1098/rsif.2014.1118
21. Sharma A, Jofre-Bonet M, Panca M, Lawrenson JG, Murdoch I. Hospital-based glaucoma clinics: what are the costs to patients. *Eye*. 2010;24(6):999–1005. doi:10.1038/eye.2009.284
22. Heijl A. Concept and importance of visual field measurements to detect glaucoma progression. *Glaucoma now*. 2010;(2):2–4.
23. Lee PP, Walt JG, Doyle JJ, et al. A multicenter, retrospective pilot study of resource use and costs associated with severity of disease in glaucoma. *Arch Ophthalmol*. 2006;124(1):12–19. doi:10.1001/archophth.124.1.12
24. Schmier JK, Halpern MT JM. The economic implications of glaucoma: A literature review. *Pharmacoeconomics*. 2007;(25):287–308.
25. Vaahoranta-Lehtonen H, Tuulonen A, Aronen P et al. Cost effectiveness and cost utility of organized screening programme for glaucoma. *Acta Ophthalmol Scand*. 2007;(85):508–518.
26. Tuulonen A. Challenges of glaucoma care – high volume, high quality, low cost. *Acta Ophthalmol*. 2013;91(1):3–5. doi:10.1111/aos.12088

27. Hagman J. Comparison of resource utilization in the treatment of open-angle glaucoma between two cities in Finland: is more better? *Acta Ophthalmol.* 2013;91(thesis3):1–47. doi:10.1111/aos.12141
28. Lindblom B, Nordmann J-P, Sellem E, et al. A multicentre, retrospective study of resource utilization and costs associated with glaucoma management in France and Sweden. *Acta Ophthalmol Scand.* 2005;84(1):74–83. doi:10.1111/j.1600-0420.2005.00560.x
29. OECD Statistics. *Stats.oecd.org*. 2017 [Internet]. Available from: <https://stats.oecd.org/>
30. Statistics Lithuania. *Labour Market Yearbook 2016*. Average net monthly earnings, 2006–2016. Vilnius, Lithuania; 2017. Available from: <https://osp.stat.gov.lt/services-portlet/pub-edition-file?id=27544>
31. Statistics Lithuania. *Social Protection in Lithuania 2015*. Average monthly state social insurance pension, 2010–2015. Lithuania, Vilnius; 2016. Available from: <https://osp.stat.gov.lt/statistikos-leidiniu-katalogas?publication=25060>
32. Olsen J, Berdeaux G, Skov J. Glaucoma costs in Denmark in treatment naive patients. *Acta Ophthalmol.* 2013;91(1):25–31. doi:10.1111/j.1755-3768.2011.02212.x
33. Olthoff C M, Schouten J S, van de Borne B W, Webers C A. Noncompliance with ocular hypotensive treatment in patients with glaucoma or ocular hypertension: an evidence-based review. *Ophthalmology* 2004;112(6): 953-961
34. Luca Rossetti OSP. Treatment strategies to help prevent Progression. *Glaucoma now.* 2010;(2):8–9.

Appendix

Questionnaire:

1. Gender:

- Male
 Female

2. Address: _____

3. Age: _____

4. Education:

- High school graduate
 Vocational school
 College
 University
 Other: _____

5. Occupation:

- Employed
 Unemployed
 Student
 Retired
 Other: _____

6. What is your monthly income?

7. How long have you been diagnosed with glaucoma?

8. How many times a year do you visit your glaucoma specialist for a follow-up?

9. Do you have any eye diseases other than glaucoma? (If yes, which ones?)

10. Do you have any other medical conditions?

- Hypertension
 Type 2 diabetes
 Asthma
 Other:

11. Have you undergone any glaucoma surgery?

- Yes
 No

12. Have you undergone any other type of eye surgery?

- Yes
 No

13. What antiglaucoma medications do you use?

Medication	Total cost	Cost after reimbursement

14. What systemic medications do you use?

Medication	Total cost	Cost after reimbursement

15. What percentage of your antiglaucoma medication costs are reimbursed by the Compulsory Health Insurance Funds? _____

16. Do you have to take a day off because of outpatient visits?

- Yes
 No
 I do not work

17. What mean of transport do you use to get to outpatient visits?

- On foot
- Public transport/bus
- Intercity bus
- Taxi
- Car

18. Do you need to come with an escort?

- Yes
- No (if no, proceed to Question 23)

19. What is your relationship with your escort?

- Husband/wife
- Family member
- Friend
- Other: _____

20. What is the occupation of your escort?

- Employed
- Unemployed
- Student
- Retired
- Other: _____

21. If the person that accompanies you is employed, does he/she miss work to escort you?

- Yes
- No

22. Why do you need an escort to get to outpatient visits?

- Drives to the hospital
- Moral support
- Disability
- Other: _____

23. Estimate the cost of one-way transportation per outpatient visit (according to your means of transport):

- Bus ticket price: _____
- Train ticket price: _____
- Taxi price: _____
- Gas price (by car): _____

24. How many kilometers do you need to travel to the hospital?

25. How long does it take for you to get to the hospital (hours and minutes)?

26. Do you have any additional costs (hiring a nanny/nurse for family members or other) when you go to outpatient visits?

Yes, what expenses: -----

No



Predicting infusion pressure during pars plana vitrectomy: a physically based model

Tommaso Rossi¹, Giorgio Querzoli², Giampiero Angelini³, Alessandro Rossi³, Carlo Malvasi³, Laura Landi¹, Serena Telani¹, Guido Ripandelli⁴

¹Scientific Institute for Research and Healthcare Polyclinical San Martino, Genoa, Italy; ²University of Cagliari, DICAAR, Cagliari, Italy; ³Optikon 2000 Inc., Rome, Italy;

⁴Scientific Institute for Research and Healthcare G.B. Bietti Foundation, Rome, Italy

Abstract

Purpose: Intraocular pressure (IOP) during pars plana vitrectomy (PPV) decreases as aspiration generates flow, a phenomenon known as head loss. Since direct measurement of the IOP during surgery is impractical, currently, available compensating systems infer IOP by measuring infusion flow rate and estimating corresponding pressure drop. The purpose of the present paper is to propose and validate a physically based algorithm of the infusion pressure drop as a function of flow.

Methods: Complete infusion lines (20G, 23G, 25G and 27G) were set up and primed. The infusion bottle was set at incremental heights and flow rate measured 10 times and recorded as mean \pm SD. Overall head loss (OHL) was defined, according to hydraulics laws, as the sum of frictional head loss (FHL; *i.e.*, pressure drop due to friction along tubing) and exit head loss (EHL). The latter is equal to the kinetic energy of the exiting flow through the trocar ($FKE = V^2/2g$). A 2nd degree polynomial equation (*i.e.*, $\Delta P = aQ^2 + bQ$, where ΔP is the pressure drop, or OHL, and Q is the volumetric flow) was derived for each gauge and compared to experimental data 2nd order polynomial best-fit curve.

Results: Ninety-seven percent of the pressure values for all gauges predicted using the derived equation fell within 2 SD of the mean difference yielding a Bland-Altman statistical significance when compared to 91% of best fit curve.

Conclusion: The derived equations accurately predicted the head loss for each given infusion line gauge and can help infer IOP during PPV.

Correspondence: Tommaso Rossi MD, Via Benedetto XV 5, 16132 Genoa, Italy.
E-mail: tommaso.rossi@usa.net

Keywords: head loss, intraocular pressure compensation, pars plana vitrectomy, volumetric flow rate

1. Introduction

Pars plana vitrectomy (PPV) addresses a variety of indications, including retinal detachment, diabetic retinopathy, macular surgery, and many others. Maintaining invariant intraocular pressure (IOP) and therefore volume during surgery, minimizes bleeding and prevents serious untoward events, as listed by Rossi *et al.*¹, including hemorrhagic choroidal detachment, optic nerve ischemia, and vitreous hemorrhage.

Infusion bottle height guarantees stable intraocular volume and equals ocular pressure under steady conditions (*i.e.*, when there is no flow). As the aspiration starts, balanced salt solution (BSS) (Alcon, Fort Worth, USA) flows through the infusion line and dissipates part of its energy, thus reducing pressure, a phenomenon called head loss. In order to maintain a stable IOP during aspiration, additional infusion pressure is needed to compensate the effect of head loss.² Conversely, when aspiration stops, flows also reduces to zero: pressure drop instantaneously vanishes and IOP suddenly increases.³

Several systems intended to compensate head loss have been developed and their efficiency has been tested by Falabella⁴ and Okamoto,⁵ although the underlying physics and algorithms used often remain unknown.

The purpose of the present paper is to characterize the pressure drop due to head loss of different infusion tubes ranging in diameter from 20G to 27G (Table 1) as a function of volumetric flow rate, in order to develop a physically based algorithm capable of calculating infusion pressure drop. This model applies to any given infusion system and allows the prediction of head loss based on the flow measurement and the deployment of reliable compensating systems. A thorough comprehension of head loss will also help design more efficient infusion lines.

Table 1. Gauge and corresponding inner diameter (in mm).

Gauge	Infusion cannula inner diameter
20G	0.69
23G	0.52
25G	0.40
27G	0.43*

*Note that “inner diameter” is considered the actual free surface available to fluid flow. The material we tested adopted the solution of an infusion cannula within the trocar for 20G, 23G, and 25G, while for the 27G infusion there was no cannula as the infusion tubing was directly connected to the trocar itself, which acted as an infusion cannula without further lumen reduction in order to increase flow. This is why the 27G inner lumen is actually wider than the 25G.

2. Materials and methods

2.1. Experimental setting

A sketch of the experimental setup is shown in Figure 1. The infusion system full of BSS, disposable tubing, cassette, 3-way stopcock, and four infusion cannulas of different gauges, 20G, 23G, 25G, and 27G (Table 1), were set up in the usual fashion and primed. All tests used the R-Evolution CR800 combined phaco-vitreotomy machine (Optikon 2000 Inc., Rome, Italy). In order to exclude possible vacuum within the infusion bottle, a plastic container open at the top was used and BSS continuously refilled to maintain the free surface height constant. The infusion ran by gravity and the cannula was taped to a plastic graduated beaker so that fluid discharge was horizontal at a given height and air-free.

2.2. Volumetric flow measures

The infusion bottle was set at incremental heights (measured from the discharge level) and the resulting volumetric flow recorded. During each experiment, the flow rate was measured by gathering fluid within the graduated container (Fig. 1, no.5) for 60 seconds after discarding the first 5 seconds of transient flow. The same procedure was repeated 10 times for each given height, z_1 , and gauge and flow recorded as mean \pm standard deviation (Fig. 2).

2.2. Physical-mathematical model and algorithm

The setting of the vitrectomy infusion system during surgery is represented in Figure 3.

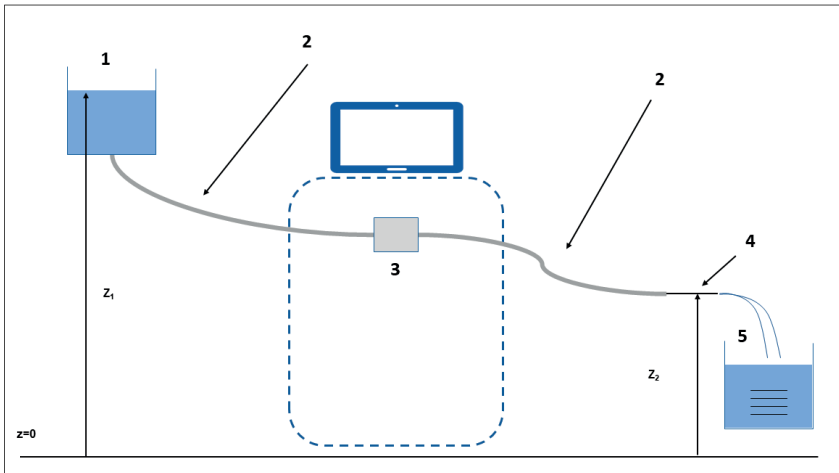


Fig. 1. Sketch of the setup used during the experiments: (1) Open bottle; (2) tubing; (3) vitrectomy machine and cassette; (4) cannula; (5) graduated beaker.

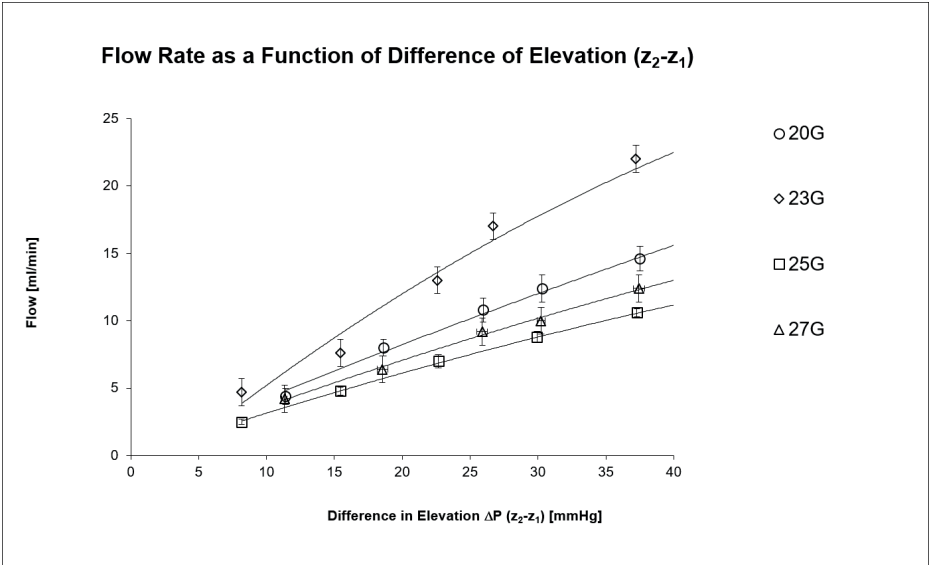


Fig. 2. Infusion line OHL as a function of flow.

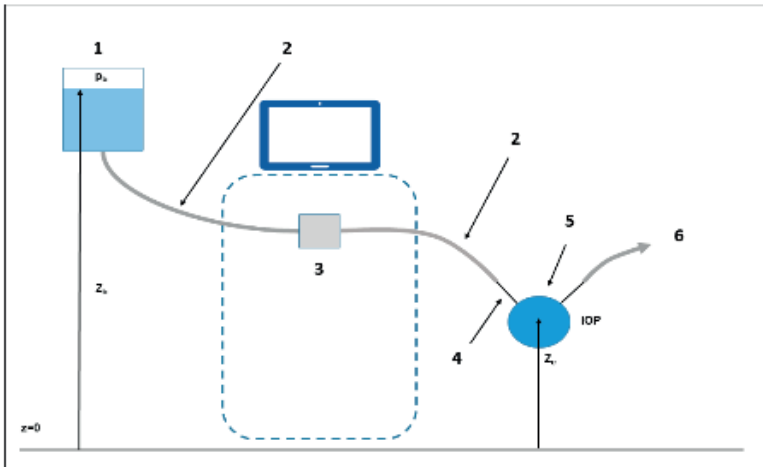


Fig. 3. Sketch of the system setup during surgery. (1) Irrigation bottle; (2) cannula; (3) vitrectomy machine with disposable cassette; (4) irrigation tubing; (5) eye; (6) aspiration.

In general, the mechanical energy per unit weight of the fluid (the so-called total head, H) is given by: $H = z + p/\gamma + v^2/(2g)$, where z is the elevation, p the relative pressure (*i.e.*, referred to the atmospheric pressure), γ the specific weight of the fluid, v the fluid velocity, and g the gravitational acceleration. The total head at the BSS bottle (Fig. 3, no. 1) is:

$$H_b = Z_b + p_b/\gamma \quad (1)$$

under the assumption that the average velocity in the bottle is negligible. p_b indicates the venting pressure if present (*i.e.*, when the pressure is equalized to ambient pressure through the opening of an electromagnetic valve $p_b = 0$; conversely, if the bottle is pressurized, p_b indicates the pressure within the bottle) and Z_b is the elevation of the free surface. Similarly, the total head in the eye is given by:

$$H_e = z_e + IOP'/\gamma \quad (2)$$

where z_e is the elevation of the eye and it is assumed that the average velocity of the fluid within the eye is negligible. When the fluid is at rest, the total head in the bottle and in the eye are the same ($H'_e = H_b$). Equating the heads and rearranging the terms yields:

$$IOP' = \gamma(Z_b - Z_e) + P_b \quad (3)$$

As the flow from the bottle to the eye starts, a portion OHL of the fluid energy is dissipated along the infusion system and the total head (mechanical energy) in the eye, $H''_e = z_e + IOP''/\gamma$ decreases correspondingly:

$$H''_e = H_b - OHL \quad (4)$$

Substituting the expression of H''_e and Equation (2) in Equation (4), IOP during infusion results in:

$$IOP'' = \gamma(Z_b - Z_e) + P_b - \gamma OHL = IOP' - \gamma OHL \quad (5)$$

Equation (4) states that the pressure drop given by the infusion flow, $PD = IOP' - IOP''$, is proportional to the OHL along the infusion: $PD = \gamma OHL$. OHL may be ideally divided into two contributions: the frictional dissipation of energy (per unit weight) along the infusion tubing (frictional head loss; FHL) and the dissipation of energy (per unit weight) at the cannula outlet (exit head loss; EHL):

$$OHL = FHL + EHL \quad (6)$$

We measured the FHL experimentally by means of the setup described in Figure 1 and computed the EHL analytically.

In order to measure the FHL during the experiments, the total head was measured both at the beginning (the bottle in Fig. 1, no.1; H_1) and at the end of the infusion line (the cannula in Fig. 1, no. 4; H_2). The difference ($H_1 - H_2$) yields the head loss due to frictional energy dissipation along the infusion tubing FHL.

The total head at the (open) bottle level corresponds to the free surface elevation ($H_1 = z_1$), since both relative pressure and velocity vanish at the open bottle surface, whereas the total head at the exit, H_2 , is the sum of elevation (z_2) and final kinetic energy (per unit weight), $FKE = v_2^2/2g$, since the outlet is in air and the relative pressure is null:

$$H_2 = z_2 + v_2^2/2g = z_2 + FKE \quad (7)$$

where v_2 indicates the fluid velocity at the outlet. Fluid velocity v_2 can be calculated as the volumetric flow rate (FR) divided by the area of the exit section (the infusion cannula) (A): $v_2 = FR/A$.

As mentioned above, FHL is the difference between the total heads at the ends of the tubing:

$$FHL = H_2 - H_1 = (z_2 - z_1) - FKE \quad (8)$$

i.e., the frictional dissipation along the tubing. The FHL can be obtained from the experiments simply by subtracting the FKE from the difference of elevation ($DE = z_1 - z_2$).

The second contribution to OHL, *i.e.*, EHL, can be evaluated by considering that, during surgery, the cannula is inserted into the posterior chamber of the eye (Fig. 3, no. 2), and once within the eye, the fluid moves erratically until it dissipates all the kinetic energy it had at its entrance through the infusion cannula (*i.e.*, the FKE). Therefore, EHL is exactly equal to FKE. In the present experiments, we calculated this additional head loss as:

$$EHL = FR^2/(2gA^2) \quad (9)$$

Combining Equation (6) with Equations (8) and (9), we obtain that OHL in surgical conditions is directly proportional to the difference in elevation ($DE = z_1 - z_2$) imposed during our experiments. $\Delta p = \gamma OHL$ is the pressure drop that must be compensated in order to maintain a constant IOP during surgical maneuvers irrespective of the infusion rate. Following the above argument, the pressure drop can be considered the sum of the contribution of the FHL, $\Delta p_{FHL} = \gamma FHL$ and EHL, $\Delta p_{EHL} = \gamma EHL$.

During our measurements, we imposed the DE and measured the FR for each given experiment and analytically computed the EHL from Equation (9). Then, we

derived the FHL as the difference between DE and FKE (Equation (8)).

The resulting values are reported in the left panes of Figures 4-7 for 20G, 23G, 25G, and 27G infusion tubing, respectively. In the same plots, the values of EHL obtained on the basis of Equation (9) are reported.

Obtained FHL values are fairly aligned along a straight line, demonstrating a linear dependency of the head loss on the flow rate, as expected in laminar flows.⁶ This result is consistent with the fact that the Reynolds number, $Re = UD/\nu$ (U indicates the velocity of the flow, D the inner diameter of the infusion conduit, and ν the kinematic viscosity of the fluid) in the infusion line did not exceed $Re = 400$ during our tests, well below the value of transition to turbulence in pipe flows.⁷ FHL for the different configurations has been approximated as a function of the flow rate by a linear best fit of experimental data points (see Equation (5) in Appendix), as reported in Figures 4a-7a. These two equations (parabolic Equation (9) and linear best fit), calculated for each given gauge, can be algebraically added to yield a third function (referred to as the 'derived' equation or function from here on) that can be used to predict the OHL along the infusion line for any given flow rate (see Appendix).

Finally, the values of OHL predicted by the above-mentioned function were compared to experimental data to verify whether they matched (Fig. 8).

Both observed and calculated OHL values have been plotted in Figure 9a-9d for 20G, 23G, 25G, and 27G, respectively. Intuitively, the lesser the distance between observed and calculated data points, the better the predictive capability of the algorithm.

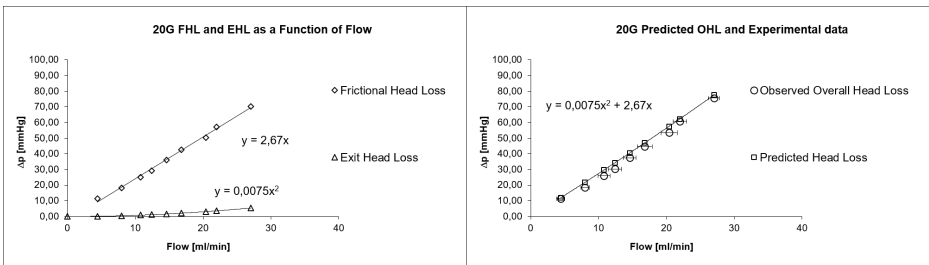


Fig. 4. 20G infusion. (Left) EHL and FHL as functions of observed volumetric flow. Both curves and derived equations (EHL, parabolic and FHL, linear) are reported in each graph. (Right) Measured OHL compared to predictions by the derived equation (reported in the plot). Experimental data points (observed OHL) and calculated values (predicted head loss) overlap significantly.

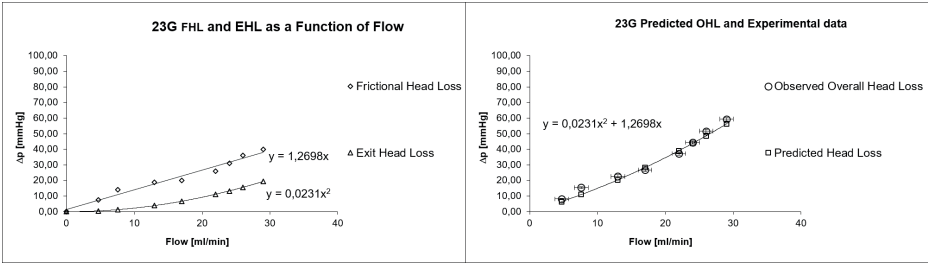


Fig. 5. 23G infusion. (Left) EHL and FHL as functions of observed volumetric flow. Both curves and derived equations (EHL, parabolic and FHL, linear) are reported in each graph. (Right) Measured OHL compared to predictions by the derived equation (reported in the plot). Experimental data points (observed OHL) and calculated values (predicted head loss) overlap significantly.

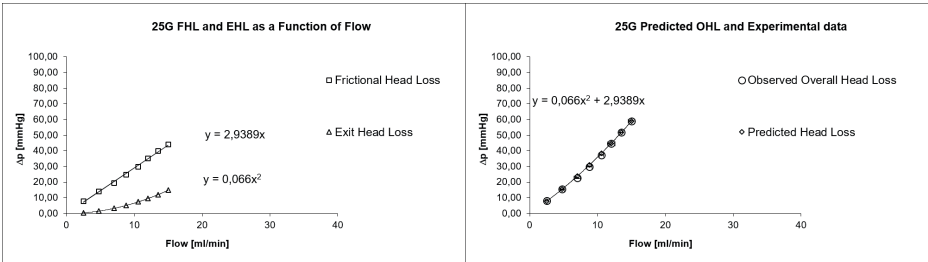


Fig. 6. 25G infusion. (Left) EHL and FHL as functions of observed volumetric flow. Both curves and derived equations (EHL, parabolic and FHL, linear) are reported in each graph. (Right) Measured OHL compared to predictions by the derived equation (reported in the plot). Experimental data points (observed OHL) and calculated values (predicted head loss) overlap significantly.

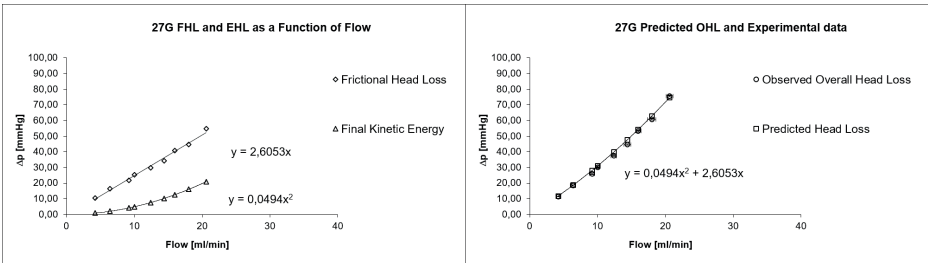


Fig. 7. 27G infusion. (Left) EHL and FHL as functions of observed volumetric flow. Both curves and derived equations (EHL, parabolic and FHL, linear) are reported in each graph. (Right) Measured OHL compared to predictions by the derived equation (reported in the plot). Experimental data points (observed OHL) and calculated values (predicted head loss) overlap significantly.

2.3. Interpolation of experimental data points with best fit polynomial equation

In order to test whether a simple best fitting algorithm of experimental flow rate data per se could yield satisfying OHL prediction, we used the Excel 2013 (Microsoft, USA) best fitting curve to yield a 2nd order polynomial equation (hereafter referred to as the interpolated equation).

We then calculated OHL values by the interpolating curve and plotted them in Figure 8 for comparison with experimental (observed) data and OHL values predicted by the derived function.

2.4. Statistical analysis

The t-test was used for repeated measures of flow rate. Statistical significance was set at a p-value less than 0.05.

The Bland-Altman statistic evaluated the agreement between observed and OHL values predicted with the derived and interpolated functions. According to Bland and Altman recommendations,^{8,9} the agreement was considered statistically significant if at least 95% of the data points fell within ± 2 SD of the mean difference between observed and predicted OHL.

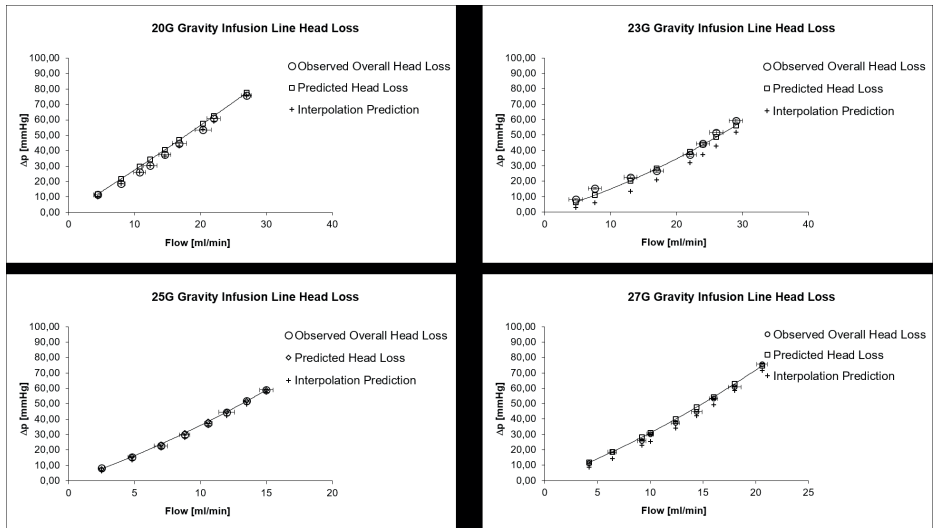


Fig. 8. Comparison of infusion line head loss: (Top left) 20G; (Top right) 23G; (Bottom left) 25G; (Bottom right) 27G. Each graph reports the comparison between experimental data points (observed), derived equation, and interpolated data prediction and curves. For each tested caliper, the derived equation yields predicted values closer to experimental ones (observed).

3. Results

Figure 2 reports volumetric FR as a function of the DE for all tested gauges. FR decreased in the following order: 23G > 20G > 27G > 25G; the difference between all calipers reached statistical significance for any given pressure delta over 15 mmHg ($p < 0.01$).

The EHL parabolic function and FHL linear equation fitting experimentally derived points are reported in the left panes of Figures 4-7, while the comparison between experimental points (observed) and the derived function (see Appendix) for all tested gauges are shown in the right panes of Figures 4-7. The graphs report the comparison between experimental data points (observed), derived equation, and interpolated data prediction and curves. For each tested caliper, the derived equation yields predicted values closer to experimental ones (observed). Figure 8 includes the 2nd order polynomial best fit in the comparison.

The Bland-Altman plot of observed OHL vs those predicted with both equations is shown in Figure 9. The derived function (Fig. 10a) shows a highly statistically significant agreement with experimental data: 97.1% of all data points falling within 2 SD of the mean difference. The best fit (interpolation) function (Fig. 10b) showed a higher SD and data scattering with only 91.1% of predicted values falling within ± 2 SD of the mean difference, a predictive value considered non-significant.

The difference between OHL data calculated with the derived and interpolated functions proved also highly statistically significant ($p < 0.01$).

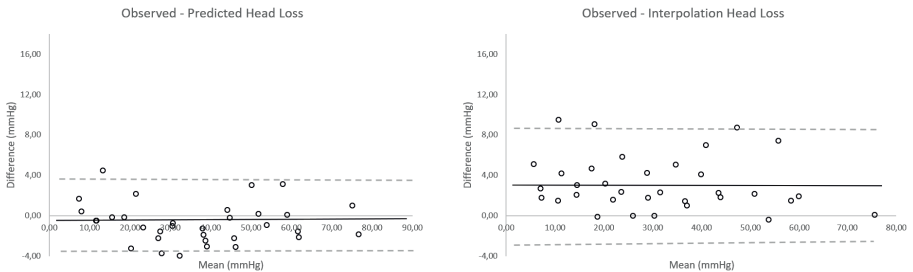


Fig. 9. Bland-Altman plot for (*left*) predicted and (*right*) interpolated values. Predicted values are less dispersed and much closer to the x-axis (97% within 2 SD) than those obtained with the interpolated function (91% within 2 SD). Solid line is the mean of difference and dotted line ± 2 SD.

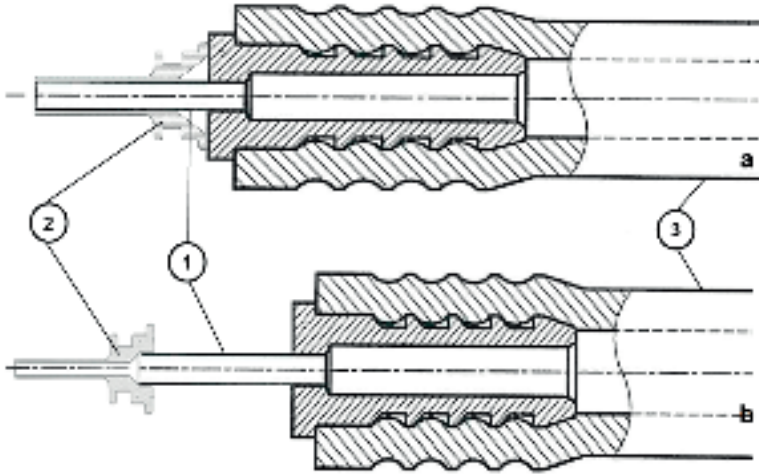


Fig. 10. Schematics of the trocar/cannula systems used during the experiments. (a) 20G, 23G, and 25G. (b) 27G. (1) infusion tubing metal connector; (2) trocar; (3) silicone tubing.

4. Discussion

Maintaining a stable IOP throughout surgery is extremely important, as pressure changes may result in severe intra- and postoperative complications, as described by Minami *et al.*¹⁰ Previous studies by Kim *et al.*¹¹ and Moorhead *et al.*¹² on PPV recorded an IOP range of 0-120 mmHg, with oscillations exceeding 40 mmHg, values which may induce acute ischemic damage also in healthy eyes.¹³

The introduction of small gauge instruments with highly efficient pumps allows high outflow rates and reduced surgical time, but inherently raises the issue of head loss and the risk of hypotony, as clearly shown in the work of Abulon *et al.*¹⁴ In fact, small gauge surgery imposes a narrow distal infusion opening that limits inflow, increasing the risk of significant pressure drop, especially at high vacuum.

The purpose of our study is to characterize the flow of 20G through 27G infusion lines in order to measure head loss and define a consistent prediction algorithm as a prerequisite for its efficient compensation.

Experimental data (Fig. 2) emphasize the objective clinical significance of head loss and the need for γ OHL compensation, showing head losses corresponding up to 40 mmHg at flow easily generated during surgery. The relative role of tubing and trocar/cannula in OHL is clarified in the left panes of Figures 4-7: the tubing frictional component is predominant (steeper curve), but the trocar/cannula gains significance as flow increases and caliper diminishes, reaching a fraction as high as approximately one-third of the FHL (left panels in Figs. 5-7). It should be noted that

FKE includes the energy dissipation along the tubing, predicted by the Hagen-Poiseuille law and the additional head loss due to the sudden variations, such as tips or connections between different conduit tracts.

Construction details explain the apparently odd result of the 27G and 23G yielding a lower EHL compared to the 25G and 20G, respectively. Unlike their counterparts, the 27G and 23G infusion tubing are in fact directly connected to the trocar, whereas the 25G and 20G have a metal cannula tip sliding into the trocar, thus reducing its inner lumen (see Fig. 10 and Table 1). Additionally, the FHL is slightly lower for the 27G infusion compared to the 25G. This demonstrates that a significant fraction of frictional dissipation (FHL) occurs at the narrowest section: the trocar/cannula system. The meaningful role that the trocar/cannula system plays both in EHL and FHL suggests that its design is crucial in minimizing the pressure drop generated by an infusion line. Interestingly, since head loss depends on the 4th power of the lumen diameter based on Hagen-Poiseuille law for fluid flow, even a small increase of the exit lumen and/or inner diameter of the cannula inner lumen may significantly decrease the related head losses.

We derived head loss function (OHL) by adding its known physical components: EHL and FHL. The former has a known equation (see Methods section and Appendix), while the latter is obtained from experimental data (Figs. 4-7). The developed algorithms are both justified from a purely hydraulic standpoint and experimentally validated, since predicted OHL values closely matched experimental data (right panels in Figs. 4-7 and Fig. 8; 20G-27G) and proved significantly more accurate than direct interpolation (Figs. 8 and 9). It is important to note that the coefficients of the equation proposed here strictly refer to tested infusion lines and cannot be applied to infusion tubing belonging to other manufacturers. Nonetheless, their form holds in general and the same simple method can be used to derive the appropriate coefficients for any given infusion line of any brand.

We relied on gravity infusion to ensure invariant pressure given by piezometric head and yield accurate measures. Although most vitrectomy machines use a forced infusion system, the concept of head loss applies to pressure drop caused by flow, regardless of how pressure is imposed on the infusion bottle.

An accurate OHL compensating system would undoubtedly represent a step forward although insufficient per se in guaranteeing a stable pressure throughout surgery. A 'feed forward' mechanism, in fact, may correct deterministic, systematic biases due to the onset and interruption of aspiration, but are useless by definition in counteracting random pressure changes as well as transient states. Feedback controls, on the contrary, can compensate unpredictable changes but take time, and require fine-tuning to avoid dangerous overcorrection and/or system divergence.

Falabella *et al.*⁴ and Sugiura *et al.*¹⁵ investigated one such device and concluded that it reestablished preset IOP after an average delay of 2.8 seconds; a lengthy time and potentially dangerous, due to the system design that reacts ex-post to pressure drop.

Falabella *et al.*⁴ also reported an overshooting pressure wave after head loss compensation, but did not investigate the opposite phenomenon. When high flow aspiration steady state is reached, the system increases infusion pressure to balance head loss; if aspiration stops abruptly, eye pressure will suddenly equal the infusion line pressure at potentially dangerously high levels.¹⁰ In such a case, flow would stop almost instantaneously and no compensating system could effectively attenuate this pressure rise.

In summary, we derived functions capable of describing with very high precision OHL based on flow in a steady regime. Although unable to capture the transient effects due to the velocity of variation of the FR, the equations based analytically on hydraulics laws demonstrated a statistically significant prediction capability of the steady component of the pressure variations. The same method can be used for any given infusion system and will help develop algorithms capable of improving intraoperative pressure control. It is worth noting that, in principle, the present study could be extended to investigate the transient pressure changes due to the flow variation velocity. However, these effects are presumably too fast to be reliably compensated in real time during surgery.

Acknowledgements

Giampiero Angelini, Alessandro Rossi, and Carlo Malvasi are employees of Optikon 2000 Inc. (Rome, Italy). None of the other authors has any financial interest in the subject matter and no financial support is involved in the study. The authors wish to thank the Fondazione Roma (Rome, Italy) for its support.

References

1. Rossi T, Querzoli G, Angelini G, Rossi A, Malvasi C, Iossa M, Ripandelli G. Ocular perfusion pressure during pars plana vitrectomy: a pilot study. *Invest Ophthalmol Vis Sci.* 2012;55:8497-8505.
2. Rossi T, Querzoli G, Gelso A, Angelini G, Rossi A, Corazza P, Landi L, Telani S, Ripandelli G. Ocular perfusion pressure control during pars plana vitrectomy: testing a novel device. *Graefes Arch Clin Exp Ophthalmol.* 2017 Sep 8. doi: 10.1007/s00417-017-3799-2
3. Abulon DJ, Buboltz DC. Performance Comparison of High-Speed Dual-Pneumatic Vitrectomy Cutters during Simulated Vitrectomy with Balanced Salt Solution. *Transl Vis Sci Technol.* 2015;29:4-6.
4. Falabella P, Stefanini FR, Lue JC, et al. Intraocular pressure changes during vitrectomy using Constellation vision system's intraocular pressure control feature. *Retina.* 2016;36:1275-1280.
5. Okamoto F, Sugiura Y, Okamoto Y, Hasegawa Y, Hiraoka T, Oshika T. Measurement of ophthalmodynamometric pressure with the vented-gas forced-infusion system during pars plana vitrectomy. *Invest Ophthalmol Vis Sci.* 2010;51:4195-4199
6. Suter, SP, Skalak, R. The History of Poiseuille's Law. *Annu Rev Fluid Mech.* 1993;25:1-20. <https://doi.org/10.1146/annurev.fl.25.010193.000245>

7. Poiseuille, J. L. M. Recherches experimentales sur le mouvement des liquides dans les tubes de tres petits diametres; II. Influence de la longueur sur la quantite de liquide qui traverse les tubes de tres petits diametres; III. Influence du diametre sur la quantite de liquide qui traverse les tubes de tres petits diametres. C. R. Acad. Sci.1840; 11:1041-1048
8. Bland JM, Altman DG. Statistical methods for assessing agreement between two methods of clinical measurement. *Lancet*. 1986;2:307-310.
9. Bland JM, Altman DG. Comparing methods of measurement: why plotting difference against standard method is misleading. *Lancet*. 1995;346:1085-1087.
10. Minami M1, Oku H, Okuno T, Fukuhara M, Ikeda T. High infusion pressure in conjunction with vitreous surgery alters the morphology and function of the retina of rabbits. *Acta Ophthalmol Scand*. 2007;85:633-639.
11. Kim YJ, Park SH, Choi KS. Fluctuation of infusion pressure during microincision vitrectomy using the constellation vision system. *Retina*. 2015;5:2529-2536.
12. Moorhead LC, Gardner TW, Lambert HM, O'Malley RE, Willis AW, Meharg LS, Moorhead WD. Dynamic intraocular pressure measurements during vitrectomy. *Arch Ophthalmol*. 2005;123:1514-1523.
13. Michelson G, Groh MJ, Langhans M. Perfusion of the juxtapapillary retina and optic nerve head in acute ocular hypertension. *Ger J Ophthalmol*. 1996;5:315-321
14. Abulon DJ, Buboltz DC. Performance Comparison of High-Speed Dual-Pneumatic Vitrectomy Cutters during Simulated Vitrectomy with Balanced Salt Solution. *Transl Vis Sci Technol*. 2015;29:4-6.
15. Sugiura Y, Okamoto F, Okamoto Y, Hiraoka T, Oshika T. Intraocular pressure fluctuation during microincision vitrectomy with constellation vision system. *Am J Ophthalmol*. 2013;156:941-947.

Appendix

1. Derived function

Figure 2a reports experimental Δp_{FHL} and Δp_{EHL} data in mmHg as functions of FR measured in ml/min for the 20G infusion line. The EHL in mmHg was evaluated as a function of FR in ml/min using Equation (3) that assumes the form:

$$\Delta p_{FHL} = a \times FR^2 \quad (4)$$

where the coefficient $a = 0.0075 \text{ mmHg}/(\text{ml}^2/\text{min}^2)$.

The FHL computed by Equation (2) is then approximated by a linear best fit as a function of the FR with the equation:

$$\Delta p_{FHL} = b \times FR \quad (5)$$

where $b = 2.6700 \text{ mmHg}/(\text{ml}/\text{min})$.

Since $OHL = FKE + FKL$, the pressure drop, which equals γOHL , can be predicted as the sum of Δp_{EHL} and Δp_{FHL} equations as follows (derived from the OHL equation):

$$\Delta p = \gamma OHL = a \times FR^2 + b \times FR \quad (6)$$

The left panel in Figure 2 reports Δp obtained from the measured OHL and the predicted head loss as a function of FR, calculated with the above equation for the 20G infusion line. The overlap between experimental and prediction data is excellent.

2. Interpolation function

For comparison, a 2nd-degree polynomial interpolant was obtained by a best fit procedure from OHL data points, *viz*:

$$\Delta p = \gamma OHL = c \times FR^2 + d \times FR \quad (7)$$

where $c = 0.0242 \text{ mmHg}/(\text{ml}^2/\text{min}^2)$ and $d = 2.1463 \text{ mmHg}/(\text{ml}/\text{min})$; the pressure drop is measured in mmHg and FR in ml/min, as usual. The values for the pressure drop obtained from the interpolating Equation (7), from the derived Equation (6), and the experimental data are plotted in the left panel of Figure 6.

The same procedure was repeated for the 23G, 25G, and 27G infusion circuits. Corresponding coefficients a and b of the derived Equation (6) and c and d of the interpolant Equation (7) are listed in Table 1 and related data is plotted in Figures 5-8.



Peripapillary non-flow area measurement for progressive localized glaucomatous perfusion damage: a case series

Gábor Holló

Department of Ophthalmology, Semmelweis University, Budapest, Hungary

Abstract

Purpose: To investigate the applicability of peripapillary non-flow area (PNFA) measurement in the radial peripapillary capillaries (RPC) layer for the measurement of progressive localized glaucomatous perfusion damage.

Methods: A research software version of the Angiovue /RTVue-XR OCT (Optovue, Fremont, CA, USA) was used to measure localized PNFA progression by clicking on a predefined peripapillary non-perfusion area on prospectively acquired images. Capillary vessel density (VD) in the corresponding peripapillary sector was also measured. High-quality peripapillary Angiovue OCT VD images of an open-angle glaucoma population prospectively imaged for 2 to 2.5 years (5 or 6 visits at 6-month intervals) were investigated. Eyes with both localized PNFA at baseline and statistically significant peripapillary VD progression in the hemifield of the PNFA were selected for the analysis.

Results: Four eyes of four patients were eligible. In three eyes, the Octopus visual field cluster mean defect in the cluster spatially corresponding to the area of the PNFA progressed significantly ($P < 0.01$) at a rate of 1.5 to 3.4 dB/year. In two eyes, neither PNFA nor sector VD showed significant correlation with the follow-up time. In one eye, significant negative correlation for sector VD ($r = -0.841$, $P = 0.036$) and almost significant positive correlation for PNFA ($r = 0.803$, $P = 0.055$) was found, while in another eye significant positive correlation for PFNA ($r = 0.875$, $P = 0.022$) but no correlation for sector VD was found.

Conclusion: Our results suggest that PNFA measurement in the RPC layer is a

Correspondence: Gábor Holló, MD, PhD, DSc, 1085 Budapest, Mária u 39, Hungary.
E-mail: hollo.gabor@med.semmelweis-univ.hu

potentially useful tool for the measurement of progression of localized glaucomatous capillary perfusion damage in open-angle glaucoma eyes with localized peripapillary non-perfusion.

Keywords: Angiovue optical coherence tomography angiography, glaucoma progression, peripapillary capillary vessel density, peripapillary non-flow area measurement, retinal nerve fiber layer thickness

Introduction

Primary open-angle glaucoma is one of the most common, irreversible, and potentially blinding painless progressive optic neuropathies, in which the retinal ganglion cells and their axons are progressively lost.¹ Treatment of open-angle glaucoma is mainly intraocular pressure reduction, which slows down progression in most of the cases, but cannot fully stop disease progression. The manifest glaucomatous structural damage is characterized by optic nerve head cupping (loss of the neuroretinal rim of the optic nerve head), reduced peripapillary retinal nerve fiber layer thickness (RNFLT), and reduced inner macular retina thickness, while the functional deterioration is best characterized and quantitatively measured with threshold perimetry of the central 30° portion of the visual field.² Since vision-related quality of life of a glaucoma patient is determined both by the severity of damage at the time of diagnosis and the speed of progression (rate of progression expressed as worsening of a parameter per year), long-term glaucoma management requires regularly repeated functional and structural testing of the eye under treatment.

Vascular dysregulation and unstable perfusion of the optic nerve head and the peripapillary retina have been considered as important risk factors for the development and progression of primary open-angle glaucoma.^{3,4} Therefore, in the last decades, several ocular perfusion measurement methods have been established and investigated for glaucoma.⁵ However, due to their limitations, their use remains minimal in clinical glaucoma care. Optical coherence tomography (OCT) angiography is a non-invasive technology that has been recently developed to measure capillary perfusion in various layers of the retina, in the macula, the optic nerve head, and the peripapillary area, respectively.⁶⁻¹⁰ The most important difference between the information provided by earlier blood flow measurement methods and OCT angiography is that the latter provides segmented measurement data for various retinal layers and areas separately, while the former methods provide results for the whole eye, whole optic nerve head, retina, or large retinal areas, respectively. The segmented and localized information offered by OCT angiography on the peripapillary perfusion and its stability or progressive reduction can be coupled with the spatially corresponding structural and functional test results.

Early and significant reduction of peripapillary vessel density (VD) in the RNFLT

(radial peripapillary capillaries layer, RPC layer) has been established in open-angle glaucoma.⁶⁻¹⁰ Measurement of glaucomatous progression of the peripapillary capillary perfusion damage, however, remains a challenge in clinical practice.¹¹⁻¹⁸ The software in some OCT angiography instruments automatically presents and calculates 360°, superior and inferior hemifield VD progression for change analysis.^{12,13,19} However, in a similar fashion to progressive glaucomatous RNFLT reduction, capillary perfusion damage may progress in small isolated areas with little effect on 360° and hemifield average values provided by the software. In order to better focus on local VD changes, the Angiovue/RTVue-XR OCT (Optovue Inc., Fremont, CA, USA) offers peripapillary sectors and sector VD values for the RPC layer.¹⁹ The peripapillary sectors follow the distribution of the sectors established by Garway-Heath and colleagues for spatial correspondence with the visual field test points and glaucomatous visual field deterioration pattern (the Garway-Heath map).²⁰ However, in localized progressive capillary perfusion damage, the sector VD values may still not be entirely satisfactory, since the damage area may not respect the sector borders, and the between-visit fluctuation of the preserved perfusion within the sector may blunt the effect of localized progression.

Non-flow area measurement is an established method in macular OCT angiography scans to quantify non-perfusion in macular disease.^{19,21} In the retinal layer of interest, the investigator selects a dark (non-perfused) area by clicking on the appropriate point on the screen, and the software automatically delineates those pixels that form a non-perfused area continuous with the site of the click-point. The area of the total delineated surface is automatically given in mm².

In the current case series, we investigated whether peripapillary non-flow area (PNFA) measurement in the RPC layer can be used to measure the progression of localized peripapillary capillary perfusion damage in open-angle glaucoma. We used a research version of the Optovue 2017.1 software that allows measuring PNFA in the RPC layer. PNFA was measured in high-quality peripapillary OCT angiography images that had been obtained earlier from open-angle glaucoma eyes in a prospective study.¹²

2. Methods

The research protocol was approved by the Institutional Review Board for Human Research of Semmelweis University, Budapest. Written informed consent was obtained from all participants before enrolment. All applicable institutional and governmental regulations concerning the ethical use of human volunteers were followed. All participants were white Europeans participating in a long-term imaging study in the Glaucoma Center of Semmelweis University in Budapest. OCT angiography and RNFLT imaging were conducted prospectively between March 2015 and September 2017. The detailed methodical description is provided in our original publication.¹²

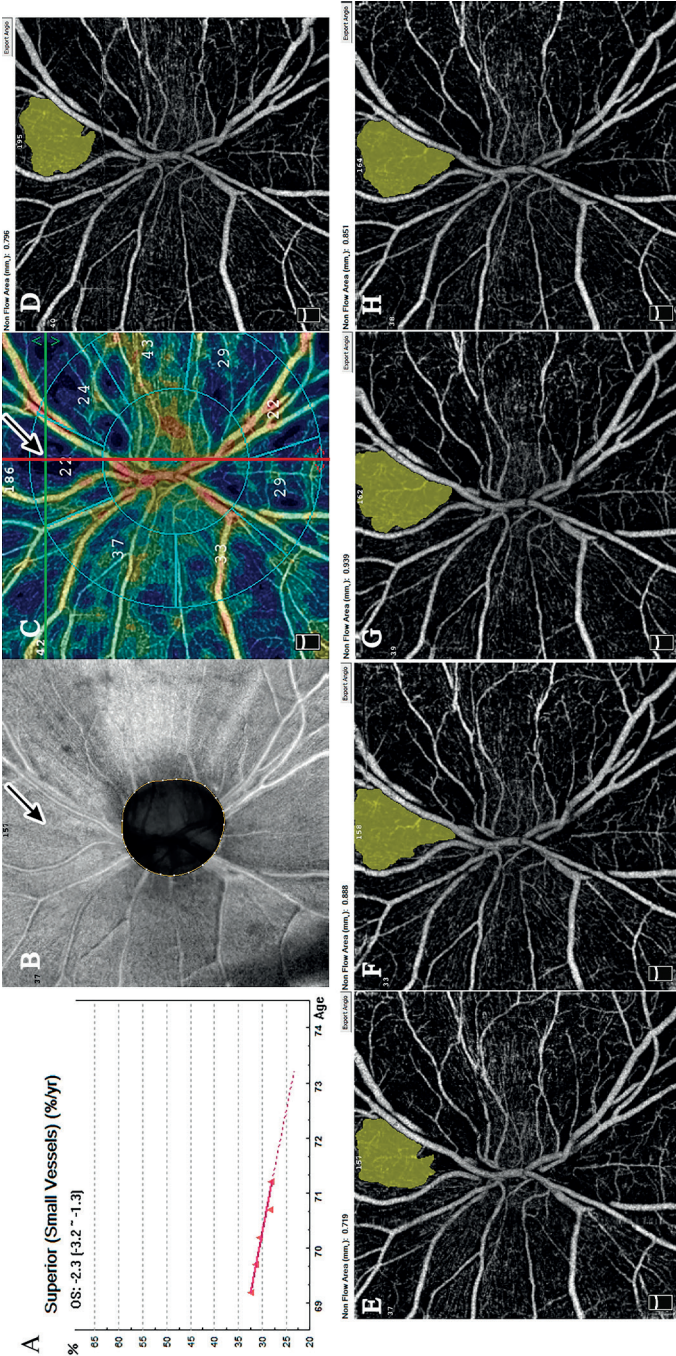


Fig. 1. Determination and measurement of PNFA progression for Case 1, left eye. (A) Statistically significant capillary vessel density progression indicated by the OCT instrument's software in the superior hemifield. (B) En face image of the RNFL. The arrow shows the location of the PNFA adjacent to a severe superotemporal retinal nerve fiber bundle damage. (C) The color-coded perfusion map shows both the location of the PNFA (superior sector, arrow) and the use of the intersection tool (cross of the green and red lines) for the determination of the position of clicking-point. (D) Baseline perfusion image with the software-determined PNFA. (E-H) The software determined PNFA on the follow-up images during the 2-year follow-up.

In brief, five or six prospective study visits at 6-month intervals were made (2 to 2.5-year follow-up). A reliable Octopus normal G2 perimetry test was conducted on all study eyes in all visits.^{12,22,23} To be included in the analysis, the participants had to have clear optical media, no eye disease other than glaucoma, and no eye surgery during the study period. For peripapillary VD measurements, we used the Angiovue/RTVue-XR OCT and the Optovue 2015.100.0.33 software version (Optovue Inc., Fremont, CA, USA) via undilated pupil. Only images with optimal image quality, no motion artifacts, vitreous floaters, or other artifacts were used for research purposes. The 4.5 mm x 4.5 mm scan size was used. All image acquisitions were made by the same investigator (GH). In the current investigation, the previously acquired VD images were reanalyzed using a research software version of software 2017.1 with the Phase 7 update.¹³ This software version provides selective information on capillary vessel density (expressed in percentage of the measured area) in the RPC layer for the superior and inferior hemifields, and for each of eight peripapillary sectors, respectively. The research software version also offers PNFA measurement in the RPC layer, irrespective to the VD sector borders. The software automatically offers linear regression analysis for superior and inferior peripapillary VD, separately, based on the Garway-Heath map.²⁰ No exact P-value is given; significant progression is defined as $P < 0.05$.

For the current analysis, eligible eyes had to have open-angle glaucoma and both localized PNFA in the baseline image and a statistically significant peripapillary VD progression for the hemifield containing the PNFA. One eye per patient was investigated; therefore, when one eye of a patient qualified for the analysis, the other eye was not considered eligible. One PNFA location per eye was investigated. The exact location of the clicking-point for PNFA measurement was determined in the baseline image using anatomical landmarks and the cross-line tool of the VD image (Fig. 1C). This image was saved and used for the exact repetition of the clicking-point on all corresponding VD images. PNFA was determined three times in each VD image. The measured value was accepted and used for analysis when all three PNFAs reflected the same area and provided exactly the same area value. Baseline Octopus visual field cluster mean defect (MD) and the software-provided cluster MD progression (in dB/year)^{22,23} for the corresponding OCT angiography follow-up period were recorded for the cluster that spatially corresponded to the PNFA location. In Octopus perimetry, a visual field cluster comprises all test points that project to the same peripapillary retinal nerve fiber bundle, based on the Garway-Heath map.^{20,22,23} In Octopus perimetry, abnormal sensitivity values are indicated with positive numbers.

2.1. Statistics

Pearson correlation with the follow-up time was used to determine progression. A significant VD progression was defined with a negative slope, and a significant PNFA progression with a positive slope at $P < 0.05$ level. The ROPstat 2.0 program package was used.

Results

Of the 24 prospectively imaged open-angle glaucoma cases, 4 eyes of 4 patients qualified for analysis (Table 1). Case 1 was an advanced primary open-angle glaucoma eye of a 73-year-old male patient with 51 μm baseline mean RNFLT and 18.5 dB baseline Octopus visual field MD. No significant RNFLT progression was measured during the follow-up, probably due to the low values, which had decreased below the measurement threshold (floor effect). PNFA was defined in the superior sector adjacent to an advanced superotemporal RNFL bundle defect (Fig. 1B and C). Neither PNFA nor sector VD progressed in a statistically significant manner (Table 1). In the spatially corresponding visual field cluster, the cluster MD progressed significantly at 2.9 dB/year rate ($P < 0.01$).

Case 2 was a primary open-angle glaucoma eye of a 65-year-old male patient with early visual field deterioration (baseline visual field MD 4.1 dB), high myopia (spherical equivalent: 8.0 diopter), and 71 μm baseline average RNFLT. PNFA was found in the inferotemporal sector. No sector VD progression and no PNFA progression were found (Table 1). No significant average RNFLT progression was measured, and the spatially corresponding visual field cluster progression was not statistically significant.

Case 3 was an early primary open-angle glaucoma eye of a 71-year-old female patient with multiple vascular white matter lesions in the brain. The baseline RNFLT was 81 μm and the baseline visual field MD 0.3 dB. The RNFLT progression rate was 3.77 $\mu\text{m}/\text{year}$ ($P = 0.004$) and the visual field cluster MD progression rate 1.5 dB/year ($P < 0.01$) in the cluster spatially corresponding to the inferonasal peripapillary sector, where sector VD progressed significantly ($r = -0.841$, $P = 0.036$) and PNFA progressed in an almost significant manner ($r = 0.803$, $P = 0.055$, Table 1).

Case 4 was an advanced juvenile open-angle glaucoma eye of a 48-year-old female patient with 59 μm baseline RNFLT and 18.7 dB baseline visual field MD. No RNFLT progression was found during the follow-up, probably due to floor effect. In the superotemporal sector, significant PNFA progression ($r = 0.875$, $P = 0.022$) was found without sector VD progression (Table 1). The visual field cluster MD progression in the spatially corresponding cluster was 3.4 dB/year.

4. Discussion

In the current case series, prospectively acquired peripapillary OCT angiography images of four open-angle glaucoma eyes with PNFA and significant hemifield VD progression were investigated using a research software version that offers both PNFA measurement and peripapillary sector VD measurement in the same images. Our goal was to investigate whether PNFA measurement in the RPC layer can add clinically useful information regarding localized progression of glaucomatous

Table 1. Demographics and progression data of the patients

Patient	Baseline average RNFLT (μm)	Baseline Octopus VF MD (dB)	Baseline sector [‡] RNFLT (μm)	Baseline Octopus VF cluster [±] MD (dB)	Average RNFLT progression ($\mu\text{m}/\text{year}$, P-value*)	Octopus VF cluster [±] progression (dB/year, P-value*)
Case 1 73-yr old male, left eye, superior sector	51	18.5	50	14.1	0.26 P = 0.410	2.9 P < 0.01
Case 2 65-yr old male, left eye, inferotemporal sector	71	4.1	53	10.8	0.04 P = 0.820	1.1 P > 0.05
Case 3 71-yr old female, left eye, inferonasal sector	83	0.3	91	0.0	-3.77 P = 0.004	1.5 P < 0.01
Case 4 48-yr old female, left eye, superotemporal sector	59	18.7	60	17.7	-0.44 P = 0.31	3.4 P < 0.01

*: Pearson correlation; ‡: sector in which the peripapillary non-flow area is located; ±: visual field cluster that spatially corresponds to the sector in which the peripapillary non-flow area is located; RNFLT: retinal nerve fiber layer thickness; VF: visual field; MD: mean defect; VD: vessel density

	Visit 1	Visit 2	Visit 3	Visit 4	Visit 5	Visit 6	r-value*
Sector VD (%)	22	22	22	21	17		-0.802 P = 0.102
Non-flow area (mm ²)	0.796	0.719	0.888	0.939	0.851		0.615 P = 0.270
Sector VD (%)	29	33	26	28	29		-0.310 P = 0.612
Non-flow area (mm ²)	0.215	0.248	0.468	0.434	0.427		0.816 P = 0.092
Sector VD (%)	36	37	35	32	33	23	-0.841 P = 0.036
Non-flow area (mm ²)	0.101	0.282	0.548	0.595	0.404	0.647	0.803 P = 0.055
Sector VD (%)	24	29	25	26	27	22	-0.330 P = 0.523
Non-flow area (mm ²)	0.384	0.519	0.524	0.512	0.669	0.620	0.875 P = 0.022

perfusion damage to the information provided by the corresponding sector VD in eyes with PNFA. The background to our investigation is that localized progression of capillary perfusion damage in such eyes can theoretically be caused both by a more-or-less diffuse reduction in a peripapillary VD sector and by an isolated increase of a non-perfusion area. In the latter case, sector VD may not detect progression since PNFA may not respect the sector borders, and the between-visit variability of the preserved perfusion in the sector may mask the effect of PNFA change.

In two of the four cases, neither sector VD nor PNFA correlated with the follow-up duration. This suggests that, in these cases, no OCT angiography progression was present in the investigated areas. In another case, high correlations (progression) were found for the spatially corresponding sector VD and PNFA, although for the latter parameter the relationship was not quite statistically significant. In the last case, a high and significant correlation was found for PNFA, but no correlation was found for the corresponding sector VD. These results show that PNFA and sector VD provide similar but not identical information, and their clinical usefulness can be different in different cases. In this small case series, we did not find any clear relationship between sector VD and PNFA progression, and visual field cluster MD progression in the spatially corresponding visual field cluster.

It is important to note that in the current work our goal was to evaluate one technical aspect of peripapillary OCT angiography for the evaluation of open-angle glaucoma progression. Thus, we present the between-parameter differences for the detection of progression within an eye, and do not interpret the between-patient differences or the differences between the systemic health conditions of the patients. Since only four eyes qualified for the current analysis, such interpretation would not be scientifically or medically established. There was a considerable difference in the age of the patients, ranging from 48 and 73 years at baseline. However, in progressive late-stage glaucoma, age plays no role in the development of glaucomatous progression in a 2.5-year follow-up period.^{12,13} One may speculate that Patient 3, with both primary open-angle glaucoma and white matter lesions in the brain, progressed rapidly due to a combination of both diseases. This, however, has no influence on the technical aspects of perfusion measurement investigated by us in the current case series. In real-life glaucoma care, elderly glaucoma patients frequently suffer from systemic vascular and cerebrovascular diseases. Therefore, Case 3 represents one type of open-angle glaucoma patient commonly seen in clinical practice.

Our case series has limitations. Even though we had 24 open-angle glaucoma patients prospectively followed for 2.5 years in the original study, in the current case series the analyzed sample size was small due to the small number of eyes with both PNFA and significant hemifield VD progression, as well as high-image quality. We could not extend the length of the analyzed period beyond 2.5 years (6 visits) since we replaced the imaging software with a different, higher resolution version. Currently, PNFA measurement has not been validated by the OCT manufacturer.

Thus, further research is necessary before this parameter can be considered for clinical application. Extension of a PNFA toward the image periphery can be limited by the image frame. This can decrease the probability of measuring true progression.

In conclusion, our results suggest that PNFA measurement in the RPC layer may provide additional information to sector VD measurement. Therefore, it may become a potentially useful new tool for the measurement of progression of localized glaucomatous peripapillary capillary non-perfusion. Evaluation of PNFA for glaucoma progression requires prospective high-quality imaging and long follow-up. Therefore, ongoing prospective clinical investigations conducted on large open-angle glaucoma populations may provide the possibility of a more detailed and sufficiently powered future investigation on the usefulness of PNFA in glaucoma progression analysis.

Acknowledgements

This research received no specific grant from any funding agency in the public, commercial or not-for-profit sectors. Gábor Holló is an unpaid consultant of Optovue, Inc. (Fremont, CA, USA) and Carl Zeiss Meditec, Inc. (Jena, Germany).

References

1. Wang W, He M, Li Z, et al. Epidemiological variations and trends in health burden of glaucoma worldwide. *Acta Ophthalmol.* 2019;97:e349-e355. doi:10.1111/aos.14044
2. European Glaucoma Society. Terminology and guidelines for glaucoma 4th Edition. Publiccom, Savona 2014.
3. Pinto AL, Willekens K, Van Keer K, et al. Ocular blood flow in glaucoma - the Leuven Eye Study. *Acta Ophthalmol.* 2016;94:592-598. doi:10.1111/aos.12962
4. Flammer J, Orgül S, Costa VP, et al. The impact of ocular blood flow in glaucoma. *Prog Retin Eye Res.* 2002;21:359-93
5. Grudzinska E, Modrzejewska M. Modern diagnostic techniques for the assessment of ocular blood flow in myopia: current state of knowledge. *J Ophthalmology.* 2018;4694789. doi:10.1155/2018/4694789
6. Yarmohammadi A, Zangwill LM, Diniz-Filho A, et al. Optical coherence tomography angiography vessel density in healthy, glaucoma suspect, and glaucoma eyes. *Invest Ophthalmol Vis Sci.* 2016;57:OCT451-459. doi:10.1016/j.ophtha.2017.01.004
7. Liu L, Jia Y, Takusagawa HL, et al. Optical coherence tomography angiography of the peripapillary retina in glaucoma. *JAMA Ophthalmol.* 2015;133:1045-1052 doi:10.1001/jamaophthalmol.2015.2225
8. Yarmohammadi A, Zangwill LM, Diniz-Filho A, et al. Relationship between optical coherence tomography vessel density and severity of visual field loss in glaucoma. *Ophthalmology.* 2016;123:2498-2508. doi:10.1016/j.ophtha.2016.08.041
9. Holló G. Relationship between optical coherence tomography sector peripapillary angioflow-density and Octopus visual field cluster mean defect values. *PLoS One.* 2017;12:e0171541. doi:10.1371/journal.pone.0171541

10. Geyman LS, Garg RA, Suwan Y, et al. Peripapillary perfused capillary density in primary open-angle glaucoma across disease stage: an optical coherence tomography angiography study. *Br J Ophthalmol*. 2017;101:1261-1268. doi:10.1136/bjophthalmol-2016-309642
11. Shoji T, Zangwill LM, Akagi T, et al. Progressive macula vessel density loss in primary open-angle glaucoma: A longitudinal study. *Am J Ophthalmol*. 2017;182:107-117. doi: 10.1016/j.ajo.2017.07.011
12. Holló G. Comparison of peripapillary OCT angiography vessel density and retinal nerve fiber layer thickness measurements for their ability to detect progression in glaucoma. *J Glaucoma*. 2018;27:302-305. doi:10.1097/IJG.0000000000000868
13. Holló G. Influence of removing the large retinal vessels-related effect on peripapillary vessel density progression analysis in glaucoma. *J Glaucoma*. 2018;27:e137-e139. doi:10.1097/IJG.0000000000000990
14. Holló G. Progressive decrease of peripapillary angioflow vessel density during structural and visual field progression in early primary open-angle glaucoma. *J Glaucoma*. 2017;26:661-664. doi:10.1097/IJG.0000000000000695
15. Holló G. Valsalva maneuver and peripapillary OCT angiography vessel density. *J Glaucoma*. 2018;27:e133-e136. doi:10.1097/IJG.0000000000000983
16. Holló G. Influence of large intraocular pressure reduction on peripapillary OCT vessel density in ocular hypertensive and glaucoma eyes. *J Glaucoma*. 2017;26:e7-e10. doi:10.1097/IJG.0000000000000527
17. Holló G. Influence of posterior subcapsular cataract on structural OCT and OCT angiography vessel density measurements in the peripapillary retina. *J Glaucoma*. 2019; 28:e61-e63. doi:10.1097/IJG.0000000000001147
18. Holló G. Peripapillary capillary vessel density progression in advanced glaucoma: a case report. *BMC Ophthalmol* 2019;19:2 <https://doi.org/10.1186/s12886-018-1021-x>
19. Optovue Inc. RTVue XR Avanti System. User Manual International Software Version 2017.1. Release date: 11/2017.
20. Garway-Heath DF, Poinosawmy D, Fitzke FW, Hitchings RA. Mapping the visual field to the optic disc in normal tension glaucoma eyes. *Ophthalmology* 2000;107:1809-1815.
21. Atta Allah HR, Mohamed AAM, Ali MA. Macular vessels density in diabetic retinopathy: quantitative assessment using optical coherence tomography angiography. *Int Ophthalmol*. 2018;Sep 7. doi:10.1007/s10792-018-1013-0. [Epub ahead of print]
22. Holló G. Comparison of structure-function relationship between corresponding retinal nerve fibre layer thickness and Octopus visual field cluster defect values determined by normal and tendency-oriented strategies. *Br J Ophthalmol* 2017;101:150-154. doi:10.1136/bjophthalmol-2015-307759
23. Racette L, Fischer M, Bebie H, et al. Visual field digest: A guide to perimetry and the Octopus perimeter. 7th edition, Hag-Streit AG, Kőniz, 2017:165-187.



Increasing protected data accessibility for age-related cataract research using a semi-automated honest broker

Samaikya Valluripally, Murugesan Raju, Prasad Calyam, Mauro Lemus, Soumya Purohit, Abu Mosa, Trupti Joshi

University of Missouri-Columbia, Columbia, MO, USA

Abstract

Ophthalmology researchers are becoming increasingly reliant on protected data sets to find new trends and enhance patient care. However, there is an inherent lack of trust in the current healthcare community ecosystem between the data custodians (*i.e.*, health care organizations and hospitals) and data consumers (*i.e.*, researchers and clinicians). This typically results in a manual governance approach that causes slow data accessibility for researchers due to concerns such as ensuring auditability for any authorization of data consumers, and assurance to ensure compliance with health data security standards. In this paper, we address this issue of long-drawn data accessibility by proposing a semi-automated “honest broker” framework that can be implemented in an online health application. The framework establishes trust between the data consumers and the custodians by:

1. improving the efficiency in compliance checking for data consumer requests using a risk assessment technique;
2. incorporating auditability for consumers to access protected data by including a custodian-in-the-loop only when essential; and
3. increasing the speed of large-volume data actions (such as view, copy, modify, and delete) using a popular common data model.

Correspondence: Prasad Calyam, 201 Naka Hall, University of Missouri-Columbia, Columbia, MO 65211, USA.

E-mail: calyamp@missouri.edu

Via an ophthalmology case study involving an age-related cataract research use case in a community cloud testbed, we demonstrate how our solution approach can be implemented in practice to improve timely data access and secure computation of protected data for ultimately achieving data-driven eye health insights.

Keywords: common data model, honest broker, precision medicine, protected data access, semi-automated compliance

1. Introduction

Health care big data being collected today for patients typically comprises heterogeneous data sets collected as: electronic health records (EHR) of patient history, wearable and other sensor data, genetics, environmental factors, medical imaging, clinical diagnosis of signs/symptoms/outcomes, and laboratory results.¹ With the increased push to promote data-driven methods in healthcare, there are massive data collection and archival efforts underway. In fact, biomedical big data has become one of the critical thrust areas for the US National Institutes of Health² due to the potential of multi-source data sharing and analysis for discovering rare patterns. Particularly, EHRs have transformed the availability of patient data as well as disease information to researchers and physicians. The American Medical Informatics Association (AMIA)³ Genomics and Translational Bioinformatics Working Group has identified knowledge discovery and data mining as important components of clinical research informatics and next-generation clinical decision support.

Building upon these advances, researchers and clinicians in ophthalmology and other fields of medicine can enhance existing knowledge relating to studies of disease management (diagnosis, prevention, early prediction, personalized treatment)⁴ for quality health care.¹ They can potentially analyze/visualize any accessible (protected) data sets to pursue medical breakthroughs in the areas of personalized medicine,⁵ and big data knowledge discovery.⁶ Thus, they can investigate novel data-driven methods in, *e.g.*, identifying latent associations of patient data sets to determine risk factors for diseases and test hypotheses with relevant heuristics as part of ongoing clinical research studies.⁷

However, there is an inherent lack of trust in the current health care community ecosystem between the data custodians (*i.e.*, health care organizations and hospitals) and data consumers (*i.e.*, researchers and clinicians). This typically results in an approach that causes slow data accessibility for consumers due to concerns such as ensuring auditability for any authorization of data access, and information assurance to ensure access compliance with health data security standards. The governance to authorize data access requests from researchers and clinicians includes several data custodian tasks. The tasks include:

1. ensuring privacy preservation of data owners (*i.e.*, patients) by checking for compliance of health regulations such as the Health Insurance Portability and

Accountability Act (HIPAA),⁸ and

- ensuring data consumers have the appropriate Institutional Review Board (IRB) protocol approvals when accessing the data.

These essential tasks introduce additional steps that cause delays in timely handling of the user data query requests. Figure 1 illustrates the current "manual honest broker" governance that is used by data custodians to manage data consumers' access of multiple data sources with heterogeneous data sets that are multi-domain, sensitive, and guarded by multiple access regulations. Consequently, any data consumer user request involving various data sets access and their corresponding secure computation resource requirements are subject to governance tasks and community cloud infrastructure configuration. These actions often take several months before approval is granted for data consumption.

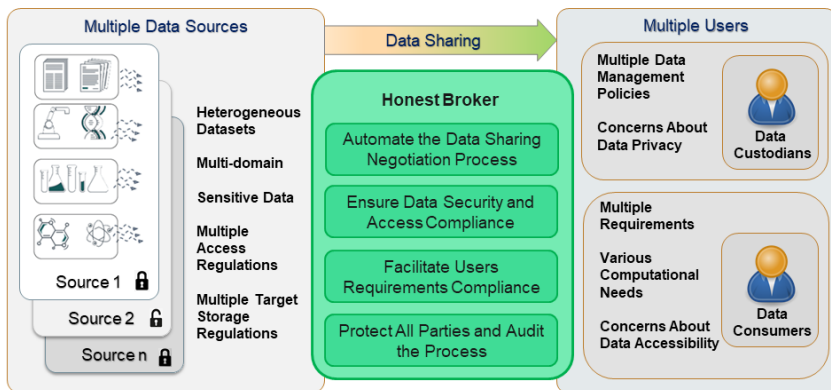


Fig. 1. Illustration of an honest broker facilitation for health big data sharing.

In this paper, we address this issue of long-drawn data accessibility by proposing a semi-automated "honest broker" framework that can be implemented in an online health application. Figure 1 shows the various features that our honest broker solution must ideally support. It should help in the automation of the data sharing negotiation process, as well as ensure data access compliance to protect all parties involved (*i.e.*, data owners, data custodians, and data consumers). The design of our honest broker framework aims to foster trust establishment between the data consumers and the custodians in several ways. Firstly, it improves the efficiency in compliance checking for data consumer requests using a risk assessment technique that uses a natural language processing scheme to automate portions of the compliance checking (based on the NIST SP 800 guidelines)⁹ given a data consumer's filled-out request form, and a data custodian's access policy document. Secondly, it incorporates auditability for consumers to access protected data by including a custodian-in-the-loop only when essential. Logging, notification, and manual approval confirmation

are performed for data actions (such as view, copy, modify, and delete) depending upon the assessed risk and the sensitive nature of the data being accessed. Lastly, it increases the speed of large-volume data actions using a popular common data model (CDM)¹⁰ on a global data catalogue (a.k.a., centralized data repository) that is hosted in a community cloud infrastructure with high-performance computing, high-throughput storage, and virtual desktop access resources.¹¹ We implement our semi-automated honest broker solution in the form of an online health application for an ophthalmology case study involving an age-related cataract research use case involving the assessment of risk factors (*e.g.*, race, age, and diagnosis) that can possibly cause the cataract diseases.¹² We also demonstrate our implementation benefits for the ophthalmology case study in a real-world community cloud testbed to improve timely data access and secure computation of protected data for ultimately achieving data-driven eye health insights.

The remainder paper organization is as follows: Section 2 lists the related work and discusses the novelty of our contributions. Section 3 presents a background regarding our ophthalmology case study and challenges experienced when accessing protected data sets. Section 4 details our solution approach for the semi-automated honest broker framework development. Section 5 describes our solution implementation and benefits demonstration in a real-world community cloud testbed for protected health data management. Section 6 concludes the paper.

2. Related work

2.1 Brokering solutions for health applications

To expedite the processing of data requests, existing works^{13,14} adapt the functionalities of a brokering approach that includes either retrieving the data faster or checking the access compliance based on data custodian policies to identify the risk of sharing the data. Prior work¹⁵ proposed an integrative clinical and genomic data framework called SPARKS, featuring a user interface that requires low levels of training on how to query/access the diverse data. However, these works^{13–15} fail to address the latency caused by the manual governance approach to process the related data requester queries. In order to address such data access issues in a diverse data environment, our approach employs a semi-automated honest brokering approach (automation is performed when possible based on risk factors) to the process of compliance checking that ultimately enhances data access speed and its secure computation in a community cloud infrastructure.

2.2 Data model approaches for integrating diverse data

Due to the diverse nature of the data sources handled in existing works,^{13,14} the data retrieval process for each user request can cause overheads for the users, such as knowing the query language for data retrieval, getting to know the internal structure

of data sources, or dealing with the burden of combining multiple data sources. To resolve such challenges, a data repository known as the common data model (CDM)¹⁰ is employed, which includes standardized data elements, reduced data discrepancies, combined handling of multiple data sources within standard views, and facilities for reproducibility and consistency of data retrievals.¹⁶ The fundamental part of using a CDM¹⁰ is that it supports data collections for different purposes and from multiple sources. For instance, providers, clinical research, patient care, and financial information can be combined within a common structure. The OMOP-CDM¹⁰ has been widely adopted to structure clinical research data,¹⁷ and multiple open-source tools have been published to bring disparate data sources into the CDM.¹⁸ Given the advantages of using a CDM, we use the OMOP-CDM version 5 in our work to improve query performance of data retrievals from the original data sources and establish a CDM-based common data repository.

2.3 Risk assessment approaches

Health data access and availability of information from different data sources are essential factors to take a clinical decision for the data consumers (*i.e.*, researchers and clinicians) involved in a health care ecosystem. Ensuring trust between the data consumers and the data custodians to facilitate data accessibility is one of the key components for many data-oriented transactions involved in health care applications. To establish mutual trust or auditability in cloud-based software deployments, the risk of each data transaction and its impact needs to be analyzed.¹⁹ As part of establishing trust between the users using our honest broker solution approach, we employ a two-step process which includes the NIST-based risk assessment approach.^{19,20} We also adapt a semi-automated compliance checking building upon the work in²⁰ in order to bring a custodian-in-the-loop only when necessary.

2.4 Compliance-checking solutions

Industry efforts in existing works^{21–23} deploy various computation capabilities along with HIPAA compliance to support the development of health care applications. Similarly, to efficiently utilize cloud-based services, consumers have to continuously monitor and manage the Service Level Agreements (SLA) and also ensure compliance among the services requested by the users. Moreover, a NIST-based compliance mechanism in our prior work²⁰ elaborates how to align and check compliance for different computing service policies for a given user request with security and performance requirements for a bioinformatics use case. Our proposed honest broker solution features semi-automated HIPAA⁸ compliance checking²⁰ based on Natural Language Processing (NLP) methods to establish the trust and auditability of data transactions in health care big data applications.

3. Background of age-related cataracts case study

3.1 EHR database

Recent advancements in health care community using big data provide unique opportunities to investigate risk factors for the development of age-related cataract diseases. As part of a cataract research study,¹² we utilize the data in a computation-friendly EHR database such as the Cerner HealthFacts® database. This EHR database captures and stores de-identified, longitudinal EHRs, including information on demographics, type of encounter, diagnosis, medications, procedures, laboratory tests, hospital information, and billing details with more than 60 million patient records. In our work, we particularly utilize a cataract data set research study as a use case for our proposed honest brokering solution development.

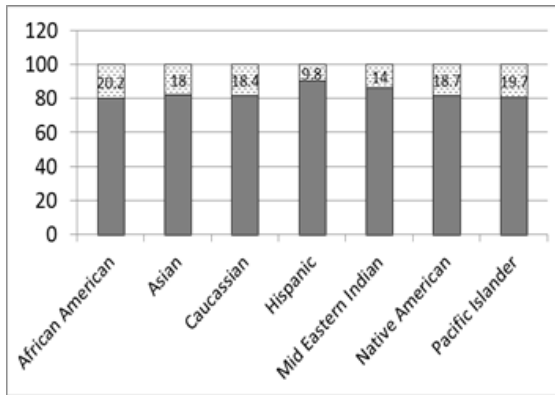


Fig. 2. Demographics of the ophthalmological data in the Cerner HealthFacts® database.

This EHR database provides us with a unique opportunity to study more variables (patient demographic, gender, weight, diagnosis, etc.) to analyze the risk factors, as shown in Figure 2 of age-related cataract diseases.¹² As part of accessing the data for this risk factor analysis,¹² the data consumers (*i.e.*, clinicians and researchers) need to run large-scale queries similar to a query shown in Figure 3. In our experiments, it took approximately 24 minutes to run a basic program using about 1% of the data available in the HealthFacts database. For more complex programs using more of the data, it took 3 or 4 days to run the query, as shown in Figure 3. Such performance outputs are extremely slow for data consumers who would have to wait long periods to test bold data-driven hypotheses and derive analytical insights for the future illness treatment or drug discovery.

3.2 Governance process challenges in the current model

In addition to the above discussed practical problems, new bottlenecks in utilizing large health-related databases can arise due to the manual governance employed in

```

PROC SQL;
CREATE TABLE PREJOINED AS
SELECT IDSK.PATIENT_ID, IDSK.PATIENT_SK, IDSK.RACE, IDSK.GENDER, HF_F_ENCOUNTER.ADMITTED_DT_TM, HF_F_ENCOUNTER.ENCOUNT
FROM IDSK AS L INNER JOIN HFFACTV3.HF_F_ENCOUNTER AS R
ON L.PATIENT_ID=R.PATIENT_ID
WHERE HF_F_ENCOUNTER.PATIENT_ID IN (SELECT PATIENT_ID FROM EYEVIS.EYE_ID);
QUIT;

PROC SORT DATA=PREJOINED NODUPKEY;
BY PATIENT_ID PATIENT_SK ADMITTED_DT_TM ENCOUNTER_ID WEIGHT HOSPITAL_ID;
RUN;

PROC SQL;
CREATE TABLE JOINED AS
SELECT PREJOINED.PATIENT_ID, PREJOINED.PATIENT_SK, PREJOINED.RACE, PREJOINED.GENDER, PREJOINED.ADMITTED_DT_TM, PREJOI
FROM PREJOINED AS L INNER JOIN D_DIM_V3.HF_D_UNIT AS R
ON L.WEIGHT_UNIT_ID=R.UNIT_ID;
QUIT;
    
```

Fig. 3. Query execution of an ophthalmology health big data application case study involving HealthFacts and the Statistical Analysis System (SAS) analytical tool.

the current HealthFacts, as shown in Figure 4. The challenges caused by the manual governance approach can be grouped under issues pertaining to: approval for extracting data, latency in extracting data, and storing the data for analysis. To elaborate, the data request process in the current HealthFacts system includes the following steps. Firstly, a data consumer sends his/her data request to the HealthFacts database custodian involving various data types such as: aggregated, de-identified, identified, and limited. Secondly, each of the user requests are reviewed by a data custodian-appointed governance committee to check for HIPAA compliance along with the policies employed across different data sources. The time taken for obtaining consent from each of the parties involved in the data access transaction typically takes several days or even months due to the manual processes. This results in queued data requests, query building to use for data visualization, latency in accessing the data (slow query response), and delayed patient care decisions, which we term as a case of *Loss of opportunity*.

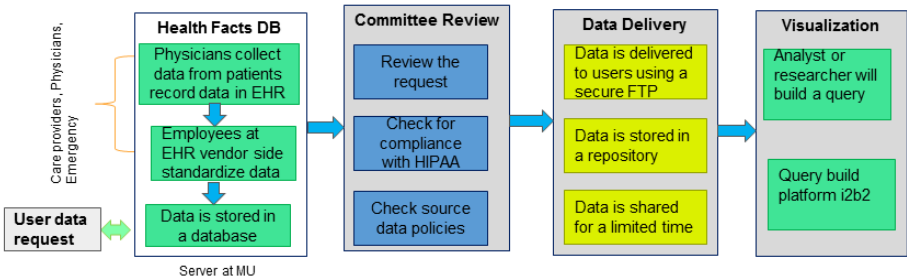


Fig. 4. Data sharing pipeline subject to a governance process for compliance assurance and auditability of protected health big data applications.

The usability is affected for data consumers due to the latency in accessibility of the data specifically to run large-scale queries for analytical purposes. The end users, who are typically not experts in high-performance computing, require automation for handling queries that involve performing a data lookup at the high scale. Moreover,

lack of auditability mechanisms for data transactions in a health care ecosystem and other related trust issues among the data consumers and custodians leads to the fear of *Loss of value* for data sets being requested. Furthermore, slow disk mechanisms used for data lookup, inadequate memory provisioning, and low-scale processing back-ends can all cause additional latency in data accessibility. To scan billions of health records from the HealthFacts database using a query look up, relevant user interfaces and appropriate community cloud system configurations need to be designed to obtain reasonable response times for retrieval of relevant records.

4. Semi-automated honest broker framework

In order to address the challenges shown in Figure 4 relevant to the case study, we propose a semi-automated brokering solution that features a pipeline to speed up the data request, access, and sharing process to help research and day-to-day clinical applications. We mainly categorize our proposed solution approach into three modules:

1. User interface (UI) module - for the user requests;
2. Honest broker module - for the brokering service to process the requests involving the governance committee; and
3. CDM - to integrate the disparity among the multiple sources of data for speedy query/analysis, as shown in Figure 5.

Thus, through our approach, multiple and disparate data sources can be integrated and the queried data can be shared without compromising the access policy compliance of the sources. Our approach also expedites data accessibility by improving performance while handling users requirements, and making the data sharing process trustworthy.

4.1 UI design

The UI module features a web-based interface that allows users to request/review data relevant to the age-related cataract research study. To develop the UI, we used an open-source platform known as HumHub,²⁴ which is an open-source social network development kit based on the Yii2 Framework. HumHub uses the Model-view controller (MVC) architecture that allows adding new features or allows changing existing core features by means of custom modules. We implemented our UI equipped with both front-end technologies (*e.g.*, HTML, CSS, Javascript) and back-end technologies (*e.g.*, PHP, PostgreSQL, Python). The UI allows data consumers (*i.e.*, researchers and clinicians) to create a new data request by filling out a questionnaire that helps the administrators in governance committee reviews, and initiates the processing of user requests to make a (approve/deny) decision. The decisions are

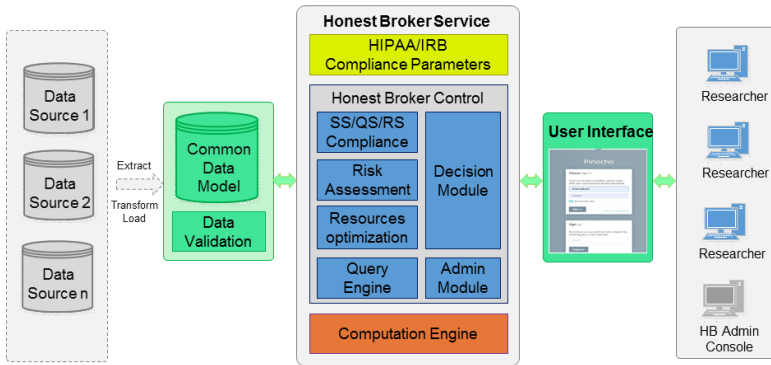


Fig. 5. Layout of the functional modules of the honest broker that include the: UI for the data custodians and data consumers, the honest broker service for semi-automated assurance and auditability of the protected health data access, and the CDM for supporting high-volume data actions.

made based on the compliance and risk values obtained for each of the user requests considering tradeoffs in the *Loss of opportunity* and *Loss of value* criteria. The interactions between the server and the web applications that are part of the data request and authorization review process in the UI are communicated via JSON formatted messages. We assume two different types of data consumers, *i.e.*, local-user (Intra-domain) and external-user (Inter-domain), who can submit their requests. These users can have access privileges with, *e.g.*, default access for Intra-domain user, and limited access for Inter-domain user. An example of the user data request form and the admin request review form to access diverse data types (*e.g.*, aggregated, de-identified, limited, identified) are included in Figure 6.

4.2 Honest brokering design

The honest brokering module serves as a monitoring system that acts upon the tasks of a governance committee, such as HIPAA and data source policy compliance, risk assessment of each data request, and subsequent decision making on each of the user requests. The honest broker module in Figure 5 illustrates the compliance check functionality, risk assessment¹⁹ relevant to a user request, and user access privileges; decision module that pertains to the approval/denial of the user requests. The *compliance* functionality, allows the admin users to classify the requests into several bags of words that are categorized as performance and security requirements (Fig. 7). The performance and security requirements obtained, as well as the policies of the requested data sources are checked for HIPAA compliance adapted from the work in Dickinson *et al.*,²⁰ whose compliance levels are classified as low, medium, and high.¹⁹

Pinocho Internal User Create New Request

New Request:

Request Title:

Request Description:

Which dataset are you trying to access?:

How will you use the data?:

How will you store the data?:

How long does the data need to be accessible?:

How soon does the data need to be accessible?:

What type of data would you like to receive?:

Pinocho Admin User

Description	Medical data with faster access
User Access Type	Internal
Requested Dataset	Care site place of service counts
How They Will Use the Data	Data within the cloud
How They Will Store the Data	Data within the cloud
Data Type	Aggregated
IRB Compliant?	No
HIPAA Compliant?	No
How Long They Will Access the Data	1 Week
How Soon They Want Access to the Data	1 Week
Risk Level	Low

Reason for Denying Request

(a) UI for the data consumer.

(b) UI for the governance committee.

Fig. 6. Honest broker UI screenshots from the HumHub-based implementation of the user data request forms, and the logging/notification/approval-seeking for assurance and auditability.

```
analysis a08.5 imaging data, stage pertain material modeling biological specimen analysis generate large amount raw processed data set image files. require different set data standardized analysis within week.  
[ 'analysis', 'a08', 'imaging', 'data', 'stage', 'pertain', 'material', 'modeling', 'biological', 'specimen', 'generate', 'large', 'amount', 'raw', 'processed', 'set', 'image', 'files', 'require', 'different', 'standardized', 'within', 'week' ]  
data is performance  
analysis is performance  
standardized is security
```

Fig. 7. Conversion of a user request into performance/security requirements using an NLP tool.

The honest broker module handles various parameters related to the requested data, and analyzes the risk associated with each user request, as shown in Figure 8. A risk assessment evaluates the risk score associated with each of the user requests, including data type requested, user type, and data source. Due to the independent event nature of these user request entities, a maximum function is used to determine the overall likelihood (f1). For accurate risk assessment, we model the compliance score (level) of the user request as input into the risk assessment module to compute the overall risk score (f2), which is an average function of (f1 and compliance score). The overall risk score is categorized on a uniform scale of 1-10 such as: low (1-3), medium (4-6), and high (7-10). To take an effective decision based on all the computed parameters, such as compliance and risk associated with the user requests, a decision process is integrated. This enables the admin to give a decision to approve/deny that considers tradeoffs in *Loss of opportunity* and *Loss of value* criteria. For ex-

ample, consider an Intra-domain user (local user) requesting aggregated data whose data source risk input is minimum. The risk assessment in this case determines the overall risk score as low. Consequently, data access is allowed by logging the data transaction and additionally notifying the admin about the data transaction. With such a risk-analysis based decision, a long-drawn manual governance committee review is avoided. However, if an Inter-domain user (external user) requests, e.g., identified data involving a large number of days range, then the risk assessment directs the admin to initiate a manual governance committee review.

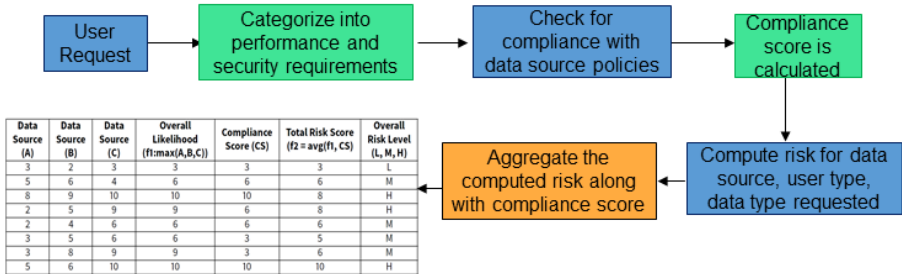


Fig. 8. Steps to calculate the compliance score during risk assessment for a given user request.

4.3 Data query using the CDM

The CDM¹⁰ helps in the creation of a global catalogue that can provide a standardized repository of the data. This standardized data is accessible to the honest broker system for sharing data analytics pipelines to Intra/Inter-domain users. As part of the CDM module, we adapt the MOP-CDM v5.0 to provide a common view of the data and control the access pertaining to different types of data and resources allocated to fulfill a particular request.¹⁰ Our CDM module improves performance by exposing a standard way to access any data request. This module combines the data from multiple data sources into a single standard model via Extraction, Transformation, and Load (ETL)¹⁸ functions, as shown in Figure 9. Data is recorded on a day-to-day basis as part of the regular healthcare operations in the EHR at the data source sites. An ETL process from EHR in a CDM implementation can be automated by scheduling incremental refresh of data on a nightly, biweekly, monthly, or even quarterly basis. Data can also be refreshed in real-time using HL7 messages. In the case that a specific data attribute is queried across a given time and day range by user(s), the corresponding data can be retrieved if necessary metadata has been added by the data sources involved. Note that the metadata information can be processed as new attributes in the data model as part of the CDM implementation. To validate our solution approach, we considered data sources containing age-related cataract patients data in the DE-SynPUF format stored in text files.

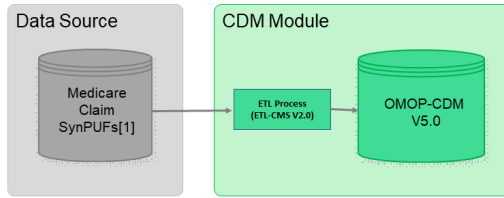


Fig. 9. Illustration of CDM module handling multiple data sources through an ETL process to convert to the standard OMOP-CDM v5.0 format and to load into central data repository.

An offline ETL process extracts the data from the text files, transforms the data into the OMOP-CDM v5.0 data model¹⁰ format, and loads the standardized data into the CDM repository built on a PostgreSQL v9.5 database. With data available in the CDM repository, the honest broker is able to process approved/authorized user requests by running predefined queries to handle the user-requested data sets.

The sample data sets as shown in Table 1, are utilized for the data retrieval process where the user requests are processed by the honest broker, as shown in Figure 10. Once the user request is processed and an approval decision is made automatically (with notification to the admin), or manually by the admin or the governance committee, the related predefined queries are executed against the CDM repository, where the time taken for data retrieval is logged. The data flow process shown in Figure 10 includes a set of text files from data sources comprising patient data in the DE-SynPUF format. The data is extracted from those files, transformed into the OMOP-CDM V5.0 format,¹⁰ and loaded into the central data repository. When user data requests are processed through data retrieval from the central repository, the result-sets are presented to the users for analysis/visualization.

If a request is semi-automatically approved by the honest broker, then the total processing time for that request is just limited to the time taken to execute the query (on the order of a few seconds). Our approach is thus based on the fact that the decision about approving or denying a request is automated based on the data access factors of the request and the additional information provided by the user for risk assessment. If further authorization is needed for data access, then a custodian-in-the-

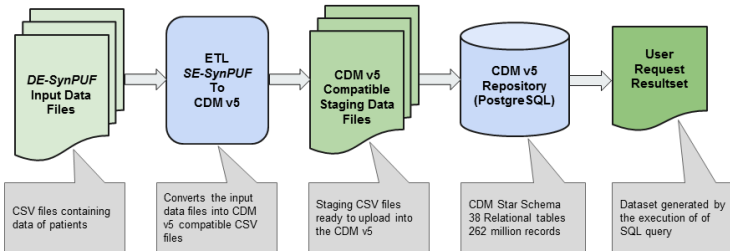


Fig. 10. Illustration of the data flow process handled by the honest broker from multi-domain sources to the target CDM-supporting computing location.

loop intervention is introduced (on the order of a few days or months). Regardless, the semi-automated honest broker along with the CDM simplifies user data access requests, and shortens the time for checks (e.g., HIPAA fields) and data transformation (e.g., de-identification) that are currently performed entirely manually. Thus, the semi-automated honest broker aids the admin as well as the governance committee to formally approve data access from multiple data sources with varied compliance requirements. Correspondingly, it also helps in streamlined and automated handling of data queries based on the fields, as well as their associated metadata in the CDM.

5. Implementation and evaluation results

5.1 Testbed setup

To evaluate our proposed honest broker solution, we implemented our solution approach using a community cloud testbed on the NSF GENI cloud infrastructure,²⁵ as shown in Figure 11. In this community cloud testbed setup, we included a host dedicated for the honest broker service on a HumHub instance²⁴ and customized our UI functionality. An ExoGeni host allows Layer 3 access to the CDM module. Virtual machines are deployed for the two hosts dedicated to the original data-source repositories (located locally and externally), and the two hosts to serve as the users (Intra-domain and Inter-domain). All of these components are connected via a network switch that emulates the functionalities of each of these entities across multiple network domains.

Each of the components in the testbed setup as shown in Figure 11 are equipped with different networking speeds based on the user type (Inter-domain, Intra-domain). An Intra-domain user requests the data access via a LAN (Local Area Network) switch to the data repository, whereas an Inter-domain data access occurs over the Internet. To process these requests, the honest broker administrator (HB-ADMIN) who is a local user, will have the option to review the request based on the responses from the honest broker component used in the testbed setup. The decisions are sent to the HB-ADMIN from the honest broker module via a high-speed network to avoid the latency in the request process. If the request is approved, then the requested data is fetched from the ETL-CDM component used in the community cloud-testbed setup shown in Figure 11. Evaluation results for the functionalities of each

5.2 Risk assessment results

As part of the honest broker service, we performed compliance checking along with risk assessment based on the scheme detailed in Section 4. As the main three entities of a user request (i.e., data source risk, data type requested, and user type) are given as the input parameters as shown in Figure 8, we term these entities as A,B,C with eight combinations of user request scenarios. As defined in Section 4, we utilize a scale of 1-10 for the related risk assessment calculations. As function f_1 is modeled as

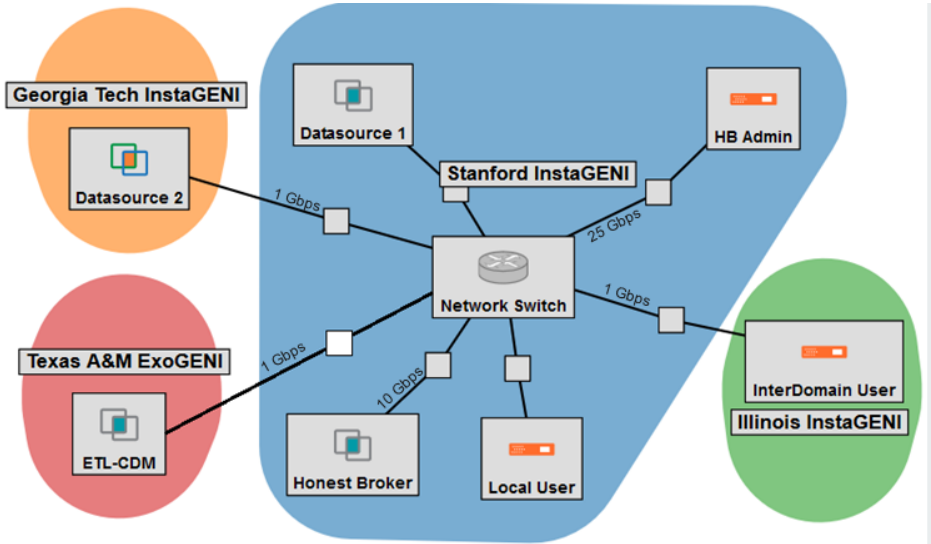


Fig. 11. Community cloud testbed topology including the honest broker node, the ETL-CDM Exo-Geni node, the data sources, an Inter-domain user external to the data custodian organization, and an admin user corresponding to the data custodian organization.

a maximum function, it is irrelevant which entity among A,B,C is high, as each of these A,B,C parameters are independent of each other in an online health application. Thus, the combination of user request scenarios are reduced to eight and used to compute f_1 , as shown in Table 1. Furthermore, as shown in Figure 8, once the compliance module identifies that the given user requests are compliant with HIPAA privacy rules, a compliance score is assigned. The values of the compliance score are assigned as low (L), medium (M), and high (H) scale based on the user request being processed.^{9,19,20}

This compliance H/M/L score is sent as an input to compute the risk score, which is the average of the three entities. The compliance score for each user request is then output as shown in Table 1. To elucidate, consider the scenario when a local user re-

Table 1. Risk assessment for exemplar user requests handled in the online health application.

Data source (A)	Data source (B)	Data source (C)	Overall likelihood ($f_1: \max(A,B,C)$)	Compliance score (CS)	Total risk score ($f_2 = \text{avg}(f_1, \text{CS})$)	Overall risk level (L, M, H)
3	2	3	3	3	3	L
5	6	4	6	6	6	M
8	9	10	10	10	8	H
2	5	9	9	6	8	H
2	4	6	6	6	6	M
3	5	6	6	3	5	M
3	8	9	9	3	6	M
5	6	10	10	10	10	H

quests (compliance level: Low) for an aggregated data (Low) and data requested is "Return the count of condition type (diagnosis)" which is compliant with HIPAA policies (as the data does not have any PHI data); the corresponding overall risk score level is Low. In this case, the admin approves the user request and shares the data based on *Loss of opportunity* (data availability) priority considerations. Similarly, for the other seven user request scenarios, we enlisted the risk scores as shown in Table 1, with corresponding data access authorizations involving logging, notification, or formal (manual) approval from admin or governance committee.

5.3 CDM-enabled query results

After the (approve/deny) decision process has been completed, the response for the requested data access is shown on the UI dashboard of the data consumer. If the request is approved, the data consumer is granted access to the data via a data delivery mechanism that can include links to, *e.g.*, archived repositories or shared folders, which have an expiration period. Each of these data delivery mechanisms is linked to the data retrieval from the CDM implementation, and logged on the data custodian system side for auditability.

Table 2. CDM-enabled data query times in the community cloud testbed implementation of the semi-automated honest broker solution for high-volume patient data requests.

Requested data set	Query time
Counts of drug types	4.1 sec
Counts of persons with any number of exposures to a certain drug	328 ms
Distribution of age across all observation period records	709 ms
How long does a condition last	783 ms
Number of patients by gender, stratified by year of birth	846 ms
Number of people continuously observed throughout a year	178 ms
Number of people who have at least one observation period that is longer than 365 days	183 ms
Patient count per care site place of service	321 ms

We validated the functionality of our proposed CDM module by uploading a cataract data sample that includes health claim-related information. The query time shown in Table 2 is the parameter we use to evaluate the implementation of our CDM module in the honest broker implementation. Based on the query time shown in Table 2, we can observe that most of the resultant data set is retrieved in a time period of less than a second, whereas, the user request related to drug type took approximately four seconds. Thus, from the results shown in Table 2, we show that the complexity of the queries is impacted when performing joins and retrieving the required data sets from the relational schema. Based on these results, we

plan to further evaluate the effectiveness of our honest broker implementation in the future by considering additional usability-related metrics relevant to the user requests for the age-related cataract study, including: query time, data request time, and latency/delay for handling a data request. We also plan to compare the results for different community cloud infrastructure configurations and data source policy variants to investigate CDM-based designs that improve the user experience.

6. Conclusion

Health care data comprises heterogeneous data sets collected from multiple sources, such as patient information, health claims, billing info, and user demographic data. To pursue new trends and medical breakthroughs, researchers and clinicians are inclined to analyze or visualize any protected data sets. In this paper, we addressed the issue of long delays in data accessibility using a semi-automated honest broker solution within an online health application implementation. Our solution approach is targeted for an ophthalmology case study involving an age-related cataract research study that is supported via an actual community cloud testbed. Our honest broker solution facilitates the data request process in the case study based on the following steps. Firstly, a user can send a data request via the user interface module we developed. Secondly, these user requests are checked for compliance with HIPPA and data source policies as part of a compliance module that uses NLP. Thirdly, the risk associated with each user request is analyzed based on the risk assessment calculation that follows NIST SP 800 guidelines. Finally, once an approve/deny decision is taken based on the tradeoffs of *Loss of opportunity* and *Loss of value* criteria, the response to the user request is sent back to the user. If the decision associated to the user request results in an approval, then the requested data is retrieved using a CDM that transforms the disparity in any multi-source data as a common representation (terminologies, vocabularies, and coding schemes). In the other cases, our honest broker solution approach handles data accessibility with a limited custodian-in-the-loop intervention using logging, notification, or formal approval from admin or governance committee.

Our future work is to extend the CDM implementation with additional features related to an automated ETL process to bring multiple data sources into the standard model on a regular basis. In addition, we also plan to compare the effectiveness of our current semi-automated honest broker solution to the current manual governance considering other exemplar case studies. Using such detailed analyses, we seek to establish a fully automated honest broker solution with minimal dependency on the totally manual governance processes in current practice through advanced features that include user interfaces for non-experts to easily query within online health applications, and parallel computation services for scalable data processing in a variety of analysis contexts of health big data sets.

Acknowledgements

This work was supported in part by the National Science Foundation (NSF) under award number OAC-1827177. Any opinions, findings, and conclusions or recommendations expressed in this publication are those of the author(s) and do not necessarily reflect the views of the NSF.

The authors would like to thank the following students at the University of Missouri, who contributed to this work: Matthew Chisholm, Matthew Gambino, Zachary Hess, Felipe Costa, and Joshua Westbrook.

References

1. Andreu-Perez J, Poon Y, Merrifield R, Wong S, Yang G. Big Data for Health. *IEEE Journal of Biomedical and Health Informatics*, 2015;19(4): 1193–1208.
2. What is Big Data?, <https://datascience.nih.gov/bd2k/about/what>, [Last accessed 05/28/2019].
3. Genomics and translational bioinformatics trending advancements and their working groups, <https://www.amia.org/programs/workinggroups/genomics-and-translational-bioinformatics>, [Last accessed : 05/28/2019].
4. Aronson S J, Heidi L R. Building the foundation for genomics in precision medicine. *Nature* 526.7573, 2015;336. doi: 10.1038/nature15816.
5. Suh K, Sarojini S, Youssif M, Nalley K, Milinovicj N, Elloumi F, et al. Tissue Banking, Bioinformatics, and Electronic Medical Records: The Front-End Requirements for Personalized Medicine. *Journal of Oncology*, 2016;
6. Fayyad U, Piatetsky-Shapiro G, Smyth P, Pecora A, Schechter E, Goy A. Knowledge Discovery and Data Mining: Towards a Unifying Framework. Association for the Advancement of Artificial Intelligence, 1996;
7. Bergner M. Quality of Life, Health Status, and Clinical Research. *Advances in Health Status Assessment*, 1989;27(3):
8. An Introductory Resource Guide for Implementing the Health Insurance Portability and Accountability Act (HIPAA) Security Rule. NIST Special Publication 800-66 Revision 1, 2013; Available from: <https://nvlpubs.nist.gov/nistpubs/Legacy/SP/nistspecialpublication800-66r1.pdf>.
9. Security and Privacy Controls for Federal Information Systems and Organizations. NIST SP800-30 Technical Report. NIST Special Publications, 2013;
10. OMOP Common Data Model (CDM) V5.0. Observational Health Data Sciences and Informatics (OHDSI), 2019; Available from: <https://www.ohdsi.org/data-standardization/>.
11. Valluripally S, Murugesan R, Calyam P, Chisholm M, Sivarathri S, Mosa A, et al. Community Cloud Architecture to Improve Use Accessibility with Security Compliance in Health Big Data Applications. ICDCN '19 Proceedings of the 20th International Conference on Distributed Computing and Networking. ACM, 2019; 377–380.
12. Raju M, Chisholm M, Mosa AS, Shyu C, Fraunfelder FW. Investigating Risk Factors for Cataract Using the Cerner Health Facts® Database. *Journal of Eye and Cataract Surgery*, 2017; doi: 10.21767/2471-8300.100019.
13. Dhir R, Patel A, Winters S, Bisceglia M, Swanson D, Aamodt R, et al. A multidisciplinary approach to honest broker services for tissue banks and clinical data. *Cancer*, 2008;7, 1705–1715. Available from: <https://doi.org/10.1002/cncr.23768>. doi: 10.1002/cncr.23768.
14. Boyd A, Hunscher D, Kramer A, Hosner C, Saxman P, Athey B, et al. The Honest Broker Method of Integrating Interdisciplinary Research Data. AMIA Annu Symp Proceedings, 2005;

15. Orechia J, Pathak A, Shi Y, Nawani A, BelozeroV A, Fontes C, et al. OncDRS: An integrative clinical and genomic data platform for enabling translational research and precision medicine. *Applied & Translational Genomics*, 2015;6, 18–25. doi: 10.1016/j.atg.2015.08.005.
16. Zhao Y, Yan B, Rocca WA, Wang Y, Shen F, Sauver J, et al. Annotating Cohort Data Elements with OHDSI Common Data Model to Promote Research Reproducibility. *IEEE International Conference on Bioinformatics and Biomedicine (BIBM)*, 2018;1109(10): 1310–1314.
17. Sia Y, Wenga C. An OMOP CDM-Based Relational Database of Clinical Research Eligibility Criteria. *PMC Stud Health Technol Inform*, 2017;245(1): 950–954.
18. Lambert GCA, Kumar P. Transforming the 2.33M-patient Medicare synthetic public use files to the OMOP CDMv5: ETL-CMS software and processed data available and feature-complete. 2016; Available from: http://www.ohdsi.org/web/wiki/doku.php?id=resources:ohdsi_symposium_2016_posters.
19. Ronald R. Guide for Conducting Risk Assessments. 2012; Available from: <https://nvlpubs.nist.gov/nistpubs/Legacy/SP/nistspecialpublication800-30r1.pdf>.
20. Dickinson M, Debroy S, Calyam P, Valluripally S, Zhang Y, Antequera R B, et al. Multi-cloud Performance and Security Driven Federated Workflow Management. *IEEE Transactions in Cloud Computing*, 2018; Available from: <https://ieeexplore.ieee.org/document/8392768>.
21. Oh S, Cha J, Ji M, Kang H, Kim S, Heo E, et al. Architecture Design of Healthcare Software-as-a-Service Platform for Cloud-Based Clinical Decision Support Service. *IEEE Healthcare Informatics Research*, 2018;
22. Getting your data ready for precision medicine - <https://www.ibm.com/blogs/insights-on-business/healthcare/getting-data-ready-precision-medicine>.
23. Community cloud architecture for salesforce health care applications - <https://www.salesforce.com/products/community-cloud/faq>.
24. HumHub: Open-source Social Network Development Kit. Available from: <https://humhub.org/en>.
25. Berman M, Chase J, Landweber L, Nakao A, Ott M, Raychaudhuri D, et al. GENI: A Federated Testbed for Innovative Network Experiments. *Elsevier Computer Network*, 2014;61(14): 5–23. Available from: <https://ieeexplore.ieee.org/document/8392768>.




Journal for Modeling in Ophthalmology

Focus and Scope

While the rapid advance of imaging technologies in ophthalmology is making available a continually increasing number of data, the interpretation of such data is still very challenging and this hinders the advance in the understanding of ocular diseases and their treatment. Interdisciplinary approaches encompassing ophthalmology, physiology, mathematics and engineering have shown great capabilities in data analysis and interpretation for advancing basic and applied clinical sciences.

The Journal for Modeling in Ophthalmology (JMO) was created in 2014 with the aim of providing a forum for interdisciplinary approaches integrating mathematical and computational modeling techniques to address open problems in ophthalmology. JMO welcomes articles that use modeling techniques to investigate questions related to the anatomy, physiology and function of the eye in health and disease.



www.modeling-ophthalmology.com

Published by Kugler Publications

www.kuglerpublications.com

